MAGNETORESISTANCE IN SEMICONDUCTOR-METAL HYBRIDS FOR POWER APPLICATIONS

A Dissertation

presented to the Faculty of the Graduate School

at the University of Missouri-Columbia

In Partial Fulfillment

of the Requirements for the Degree

Doctor of Philosophy

---

by

CLAY NUNNALLY

Committee

Dr. T. Greg Engel, Chairman

Dr. John W. Farmer

Dr. Naz Islam

Dr. John M. Gahl

MAY 2008

The undersigned, appointed by the dean of the Graduate School, have examined the dissertation entitled

MAGNETORESISTANCE IN SEMICONDUCTOR-METAL HYBRIDS

FOR POWER APPLICATIONS

presented by Clay Nunnally, a candidate for the degree of doctor of philosophy and hereby certify that, in their opinion, it is worthy of acceptance.

Dr. T. Greg Engel (Committee Chair), James C. Dowell Associate Professor of Electrical and Computer Engineering

Dr. John W. Farmer (Outside Member), MURR Senior Research Scientist and Adjunct Associate Professor

Dr. Naz Islam, LaPierre Associate Professor of Electrical and Computer Engineering

Dr. John M. Gahl, Professor of Electrical and Computer Engineering, MURR Senior Research Scientist

ACKNOWLEDGEMENTS

I would like to thank Dr. Greg Engel for his guidance and assistance during the course of this research. Additionally, I would like to thank Dr. John Farmer, Dr. John Gahl, and Dr. Naz Islam for their advice and willingness to serve on my Ph.D advisory committee. I would like to thank Dr. Stuart Solin and his group at Washington University for their correspondence and information regarding EMR. Finally, I would like to thank Shawn Huenefeldt, Brian Samuels and Rick Wells for their assistance during the course of this research.

Table of Contents

Table of Figures

Figure Page

List of Tables

Table Page

List of Nomenclature

2DES	Two-dimensional electron structure	
B	Transverse magnetic field or magnetic flux density	T
CMR	Colossal magnetoresistance	
E_g	Semiconductor gap energy	eV
EMR	Extraordinary magnetoresistance	
ESHP	Externally- shunted Hall plate	
FEM	Finite element methods	
GMR	Giant magnetoresistance	
HgCdTe	Mercury Cadmium Telluride	
m*	Semiconductor electron effective mass	kg/kg
MBE	Molecular beam epitaxy	
m_e	Mass of an electron	kg
MOS	Metal-oxide semiconductor	
MR	Magnetoresistance	-
n	Bulk Semiconductor majority carrier density	m^{-3}
n_m	Free electron density in metallic shunt	m^{-3}
PFN	Pulse forming network	
PSPICE	Personal computer simulation program with circuit emphasis	
R_{2p}	Two-point (terminal) device resistance	Ω
R_{4p}	Four-point (terminal) device resistance	Ω
SCD	Shunted Corbino disk	
SCP	Shunted Corbino plate	
t_c	Mean free collision time	s
vdP	Van der Pauw	
μ	Semiconductor Hall mobility	$m^2/V\ s$
μ_m	Metallic shunt Hall mobility	$m^2/V\ s$
σ	Semiconductor conductivity	$S\ m^{-1}$
σ_m	Metallic shunt conductivity	$S\ m^{-1}$

Abstract

Extraordinary magnetoresistance (EMR) in semiconductor-metal hybrids has been studied exclusively for sensor applications. However, some properties of EMR-based devices are potentially advantageous for power applications. A PSPICE finite-element model has been developed to aid in the analysis and design of semiconductor-metal hybrid devices for power applications. This paper presents the model theory, implementation, and results when applied to an externally-shunted van der Pauw (vdP) plate. The conventional 4-terminal (4-point) vdP probe configuration for sensors is compared to 2-terminal (2-point) probe positioning which is necessary for power devices. The effects of material properties on resistance and magnetoresistance (MR) for an externally-shunted vdP plate in both probe configurations are presented.

Two prototype metal-semiconductor hybrid topologies for power applications have been derived from EMR sensor technology and are examined here for the first time, the shunted Corbino plate (SCP) and the externally-shunted Hall plate (ESHP). The PSPICE FEM model was used to analyze MR behavior as a function of geometric ratios characteristic of each new topology and semiconductor material properties. Sets of models for each topology generated using ElecNET were used to evaluate these devices' pulsed-current and breakdown limitations.

The PSPICE model has the benefit of being versatile, simple, and computationally stable. Understanding the 2-point resistance behavior of existing EMR sensors is a

primary step in characterizing EMR-based power devices since it, and not the conventional 4-point resistance, is of merit for power applications.

The largest room-temperature MR ($\Delta R/R_o$) calculated for each prototype topology was approximately 2000% at 1 T. Current concentration caused by the inclusion of a shunt was found to limit the pulsed current capacity in each device studied. For a common scale (13.6 mm x 3.4 mm x 1 mm), pulsed-current capacity was found to vary within each device topology according to a characteristic geometric ratio. The best candidate, in terms of MR, from the SCP family showed a 1-ms pulsed current capacity of 323 A. In contrast, the pulsed current capacity of the best ESHP device was found to be 82 A. The best device geometries in terms of MR showed the lowest breakdown voltage among each set, both ~ 200 V. The data set presented here is useful for purely characterization purposes. But also, these findings and the unavoidable trade-off between magnetic sensitivity and breakdown voltage indicate that potential advantages are offset by intrinsic limitations in the use of the EMR effect for power applications.

1. Introduction

In 2000, Solin et al. reported a large change in resistance of Au-InSb hybrid structures when subjected to a transverse magnetic field [1]. The magnitude of this magnetoresistance (MR) significantly surpassed the traditional MR caused by Lorentz-force deflection of current. To distinguish, this effect was called Extraordinary Magnetoresistance (EMR). Magnetic field sensors based on EMR have exhibited room-temperature resistance increases ($\Delta R/R_o$) up to 75000% for a transverse magnetic field of 4 T [2]. EMR sensors consist of a highly conductive inhomogeneity or shunt embedded in a narrow-gap semiconductor matrix. At zero magnetic field, current flows preferentially through the shunt since it is highly conductive and the current density vector is parallel to the electric field ($J \parallel E$). In this case the shunt acts as a short circuit and the resistance of the hybrid structure is lower than that of a homogenous structure of the same size. At large magnetic field, the current is deflected by the Lorentz force which is then at an acute angle to the electric field. By virtue of the large mobility of the narrow-gap semiconductor matrix, this angle, the Hall angle, approaches 90° i.e. $J \perp E$. Since the local electric field is perpendicular to the shunt-semiconductor interface, the current becomes tangent and is deflected around the shunt. For sufficient magnetic fields the current then travels only in the semiconductor matrix; in this case the shunt acts as an open circuit. This transition of the shunt from short circuit to open circuit results in an enhanced geometric MR or EMR [3].

The EMR effect has important implications for magnetic field sensing applications that include position/speed sensing and high-density magnetic data storage. In particular, prospective EMR read-head sensors would exhibit higher sensitivity and significantly faster response times than conventional multi-layer metallic (spin-valve) read heads [4]. Since EMR read heads are non-magnetic, they would not be subject to limitations of magnetization dynamics at the superparamagnetic density limit of ~ 100 Gb/in^2, such as the spin-valve read heads [5]. Scaling properties of EMR read-head sensors indicate the possibility of ultra-high areal density magnetic recording on the order of 1 Tb/in^2 [6].

To date the EMR effect has been characterized only in the purview of sensor applications. However, a magnetically-actuated switch or current commutator based on the extraordinary magnetoresistance (EMR) effect offers potential advantages over traditional solid-state switches because its composition and switching mechanism are fundamentally different. Possible advantages include larger current densities and current rise times due to the absence of a PN junction. Since EMR devices employ strictly majority carrier semiconductors, minority-carrier effect such as thermal runaway do not occur. Transition times are not limited by the conductivity modulation of a drift region and there is no reverse current associated with stored charge during turn-off as in bipolar devices. The basic trade-off in power devices between switching speed and on-state conduction losses is not intrinsic to an EMR-based switch. On state conduction losses have the potential to be very low since the current flows preferentially through a highly conductive, metallic shunt at zero magnetic field.

The recent development of EMR-based sensors presents an opportunity to study the effect for a different end product. The characterization of devices based on the EMR effect in terms of power-device performance is the first step in assessing the feasibility and utility of such devices in this new role.

A PSPICE finite-element model (FEM) has been developed to aid in the analysis and design of semiconductor-metal hybrid devices for power applications. This paper presents the model theory, implementation, and results when applied to an externally-shunted van der Pauw (vdP) plate. The conventional 4-terminal (4-point) vdP probe positioning is compared to 2-terminal (2-point) probe positioning which is necessary for power devices. The effect of material properties on device resistance and MR in both 4-point and 2-point configurations is contrasted.

Two prototype metal-semiconductor hybrid topologies for power applications, the shunted Corbino plate (SCP) and the externally-shunted Hall plate (ESHP), have been derived from EMR sensor technology and are presented here for the first time. The PSPICE FEM was used to analyze MR behavior as a function of geometric ratios characteristic of each new topology. Additionally, MR behavior was analyzed as a function of semiconductor material properties. Sets of models for each topology generated using ElecNET were used to evaluate these devices' pulsed-current and breakdown limitations as a function of a geometric ratio.

The PSPICE model has the benefit of being versatile, simple, and computationally stable. The 2-point resistance characterization of an existing EMR device is a primary step in characterizing this effect for power applications. The two-point MR calculated

here for the externally-shunted vdP plate is significantly lower than the conventional 4-point MR. The distinction between and numerical evaluation of the two ways of measuring resistance in an EMR device is important because extremely large 4-point MR has been reported in the literature [2, 7, 8]. However, the 4-point magnetoresistance is not useful in the scope of typical power applications.

The MR characterization of the prototype devices as a function of topology, geometric ratio, and semiconductor material properties forms the fundamental evaluation of EMR devices for power applications. The pulsed current and breakdown voltage limitation mechanisms are identified. These limitations are evaluated for typical material properties and scale. The largest MR ($\Delta R/R_o$) calculated for each prototype topology with typical high-mobility semiconductor material properties was approximately 2000% at 1 T. Current concentration caused by the inclusion of a shunt limits the pulsed current capacity in each device studied. Pulsed-current capacity was found to vary with device topology and geometric ratio. The best candidate (in terms of MR) from the SCP family showed a 1-ms pulsed current capacity of 323 A. In contrast, the pulsed current capacity of the top ESHP device was found to be 82 A. The best device geometries in terms of MR unfortunately showed the lowest breakdown voltage among each set, both ~ 200 V. The data set presented here is useful for purely characterization purposes. But also, these findings and the unavoidable trade-off between magnetic sensitivity and breakdown voltage indicate that potential advantages are offset by fundamental limitations in the use of the EMR effect for power applications.

This paper begins with a review of geometric MR, a Hall-effect opening switch and EMR. Chapter 3 presents the theory, assumptions, and basic equations of the PSPICE FEM model along with a description of its implementation. This chapter will also include a description a conformal mapping procedure commonly used to aid in EMR device modeling and design. In Chapter 4, the results of the model as applied to an externally shunted van der Pauw (vdP) plate will be presented. These results on the externally shunted vdP plate demonstrate the effect of probe position on MR and the effects of material properties on device resistance and MR in both 4-point and 2-point configurations. Chapter 5 presents prototype MR hybrid devices which have been identified as candidates for power applications. The two new topologies examined here have been derived from previous sensor designs. Device minimum and maximum resistance, MR, and dR/dB are calculated using the PSPICE FEM model. Pulsed current capacity and breakdown voltage are calculated numerically using two sets of ElecNET FEM models. A summary, conclusions, comments on feasibility, and suggested future experiments are then discussed in Chapter 6.

2. Review of Geometric Magnetoresistance and EMR

The magnetoresistance of a material consists of a physical component and a geometric component. The physical component involves the magnetic field dependence of material properties such as mobility or carrier density. The geometric component is due to a change in the current distribution in the device when subjected to a magnetic field. Geometric MR is influenced by electrode configuration, material composition, and the shape of the device [9].

The physical MR dominates in two types of magnetic materials considered traditional candidates investigated for the development of sensors with improved room temperature MR. The first type is metallic multi-layer structures which exhibit giant MR (GMR) and the second is manganese-based perovskite oxides which exhibit colossal MR (CMR). In contrast, narrow-gap semiconductor/metal hybrid structures have recently been developed to exploit the geometric component of MR in order to exhibit much larger room-temperature MR than physical-MR-based sensor materials [2] . The effect of enhanced geometric MR by virtue of a metallic shunt in high-mobility semiconductors is called EMR.

This class of MR device has been characterized almost exclusively for sensor applications, most notably for the development of read-head sensors for ultrahigh-density magnetic recording applications [6, 8, 10]. This chapter will review the concept of geometric MR, a previous pulsed power application of the Hall-effect, and EMR in semiconductor-metal composites. Its purpose is to lay a framework of prior work

relevant to the characterization of metal-semiconductor hybrids for power applications that is found in the rest of the paper.

2.1 Geometric Magnetoresistance

Charge carriers moving in a semiconductor under the influence of an external electric field *E* and an orthogonal magnetic induction *B* are subject to the Lorentz force given by

$$\vec{F} = q(\vec{v} \times B). \tag{2.1}$$

This force results in the direction of the current density vector *J* no longer coincide with the direction of the external electric field. This angle between *J* and *E* is called the Hall angle. Which is given by

$$\tan(\theta) = \mu_H B. \tag{2.2}$$

where θ is the Hall angle, μ_H is the Hall mobility and B is the transverse magnetic field magnitude. The Hall mobility is an effective mobility of charge carriers under the influence of a transverse magnetic field component. The Hall mobility is an important material property in MR devices because it determines the relative sensitivity to transverse magnetic fields. Its variation with temperature and dopant density is similar to that of the drift mobility [11]. In contrast to the drift mobility of charge carriers, the Hall mobility carries with it the sign of the charge on the carrier to which it pertains. For this paper the term mobility is used in reference to Hall mobility unless otherwise specified. For moderate to heavily doped majority carrier semiconductors, the Hall mobility is nearly identical to the majority carrier (electron or hole) electric-field drift mobility [9].

The simplest device that demonstrates the effect of geometry on the MR and hall voltage generation is a hall plate. Consider the simple hall plates in Fig. 2-1. A voltage (V_x) is applied between the two current electrodes of each plate and a magnetic field is applied perpendicular to the current density vector *J.*

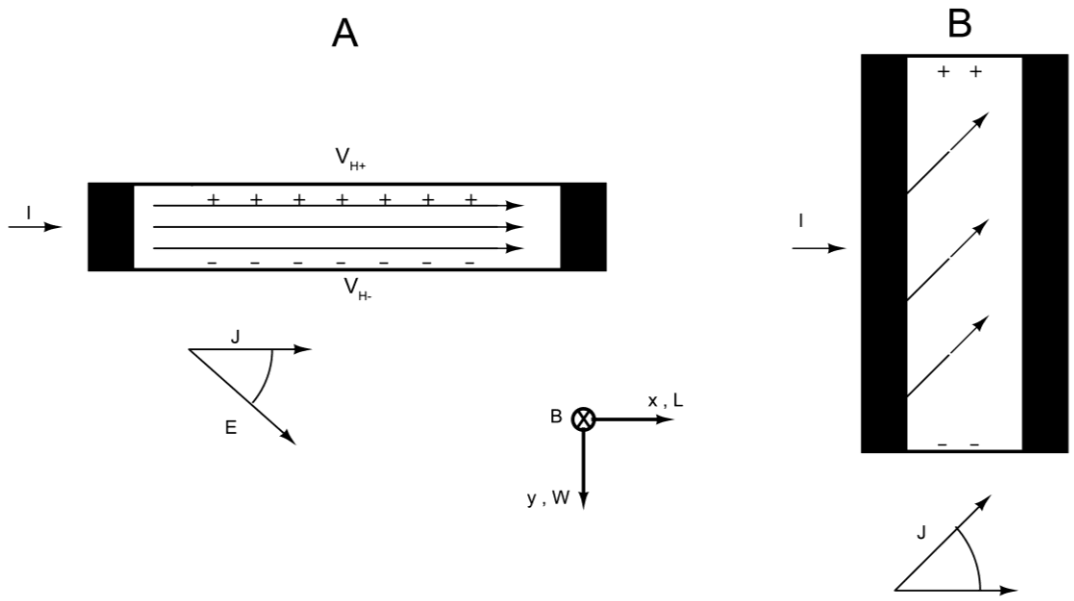

Fig. 2-1 Long (A) and short (B) hall plates with current density (J), electric field (E), magnetic field (B), and Hall angle (θ) indicated in vector diagrams.

The Lorentz force distorts the current density vector near the electrodes and causes an accumulation of charge at the top and bottom of each hall plate away from the injecting electrodes. For a long Hall plate (L >>W) as in Fig. 2-1(A), this accumulation of charge produces a transverse voltage, the Hall voltage, and balances the Lorentz force. This results in parallel current density vectors for the large region away from the electrodes, a very small net current deflection and thus a small change in resistance. In the short Hall plate (W>>L) of Fig. 2-1(B) the space charge generated by the Lorentz force is shorted by the injecting electrodes and the current density vectors are distorted

in the majority area of the device. This distortion leads to a longer path length for current through the device under a transverse magnetic field. The corresponding increase in resistance in the presence of a magnetic field is called the geometric MR effect.

Hall plates have a quadratic dependence on magnetic field for small hall angles but display a linear dependence at larger hall angles [12]. In contrast, a Corbino disk retains the quadratic dependence of the MR regardless of Hall angle since there is no boundary for a balancing charge to accumulate. As illustrated in Fig. 2-2, the Corbino geometry permits unimpeded current deflection throughout the entire area. This results in a nearly tangential direction of current flow between the center and outer electrodes at high values of $\mu_H B$.

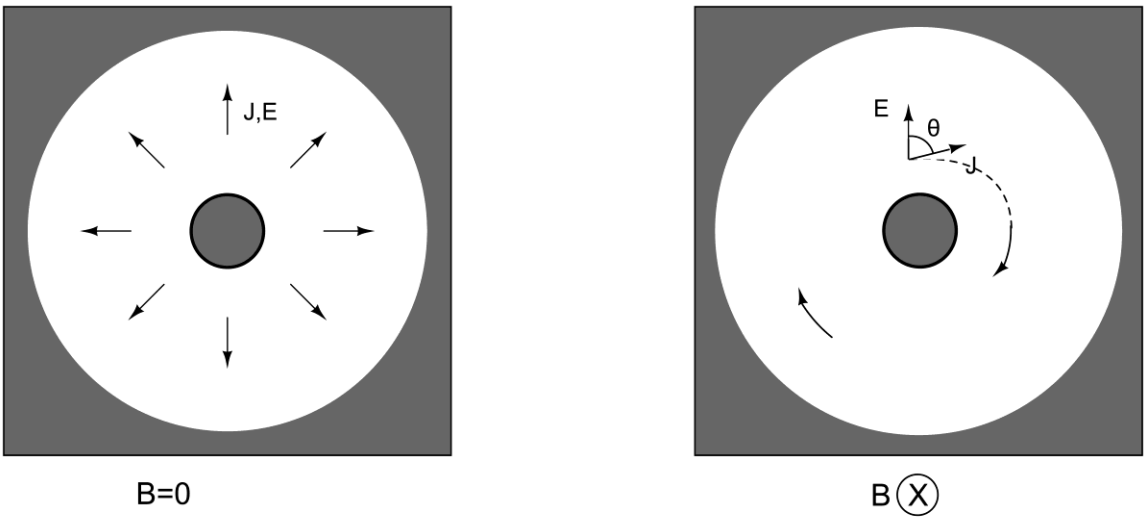

Fig. 2-2 A Corbino disk with current density and electric field vectors shown in (left) the absence of and (right) in the presence of a transverse magnetic field.

The Corbino geometric MR is given by

$$\frac{R(B) - R(B=0)}{R(B=0)} = \mu_H^2 B^2 \tag{2.3}$$

where μ_H is the Hall mobility and B is the transverse magnetic field magnitude. This is the same geometric MR exhibited by a short Hall plate only for small Hall angles (μB <<1).

2.2 Hall-Effect MR Devices for Pulsed Power Applications

While small signal and sensor applications are numerous for Hall-effect devices in the MR mode of operation, power applications have been less emphasized in the literature [13]. One notable power application has been in the switching of large scale, rep-rated inductive circuits. As described in [14], for large scale inductive circuits, opening switches with the properties of being fast (< 10^{-3}s) and non-destructive have advantages over mechanical and explosively-ruptured circuit breakers, respectively. These potential benefits of a solid-state circuit interrupter with spurred the development of a Hall-effect circuit interrupter in the form of the InSb Corbino cylinder shown in Fig. 2-3.

Some results of note in this application include:

- A peak MR ratio R(B)/R(B=0) on the order of 100 for a 6T field and low current density (~$3x10^3$ A/cm^2)
- A decaying MR ratio with increasing current density(~$5x10^3$ A/cm^2)
- melting of radial InSb filaments at high current densities and magnetic fields, which was attributed to current concentration resulting from breakdown

- a reported power density of 1.2 MW cm^{-3} as limited by avalanche breakdown at a field of 10^5 V/m

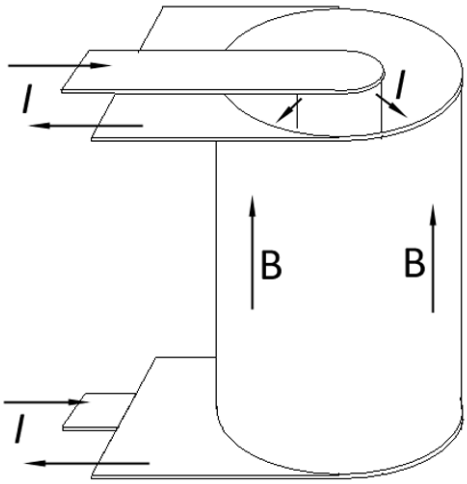

Fig. 2-3 A Coaxial mounting of InSb Corbino cylinder for inductive switching applications.

2.3 Extraordinary Magnetoresistance

Inhomogeneities such as accumulation layers, precipitates, doping variations, and metallic inclusions have been studied to explain anomalously-high measured mobilities in high-mobility semiconductors [15-17]. These studies concluded that the mobility of a semiconductor is not an accurate indication of sample quality unless the purity is well known.

More recently, Solin et al. have taken this effect that might have been considered a nuisance, and turned it into an asset. It has been shown that the geometric optimization of conducting inhomogeneities indeed improves the apparent mobility, but

it also improves as the geometric MR effect in inhomogeneous semiconductors [1-3, 18]. Of major importance in this enhancement is the effect of electric-field boundary conditions on the current at the metal-semiconductor interface. This effect is illustrated in Fig. 2-4. For $\sigma_m >> \sigma_s$ the local electric field is orthogonal to the metal-semiconductor interface. At zero magnetic field (Fig. 2-4B), the current density vector (J) is parallel to the applied electric field (E) resulting in a large current density through the shunt which approximates a short circuit. For a large transverse magnetic field (Fig. 2-4C), the Hall angle approaches 90° (J ⊥ E) and current is deflected away the shunt which now approximates an open circuit. The resulting enhanced geometric MR from boundary conditions at the metal/semiconductor interface is called extraordinary MR (EMR).

In further investigations of this effect a modified vdP disk of n-type InSb with a concentric metallic shunt has shown room temperature geometric MR up to 9,100% at 0.25 T as in [2]. The MR in the proof-of-principal vdP disk was shown to be extremely sensitive to the size of the conducting inhomogeneity. The EMR effect has important implications for magnetic field sensing applications that include position/speed sensing and high-density magnetic data storage. In particular, prospective non-magnetic EMR read-head sensors would exhibit higher sensitivity and significantly faster response times than conventional multi-layer metallic (spin-valve) read heads [4]. Since EMR read heads are non-magnetic, they would not be subject to limitations of magnetization dynamics at the superparamagnetic density limit of ~ 100 Gb/in^2, such as the spin-valve read heads [5]. These scaling properties of EMR read-head sensors indicate the possibility of ultra-high areal density magnetic recording on the order of 1 Tb/in^2 [6].

.

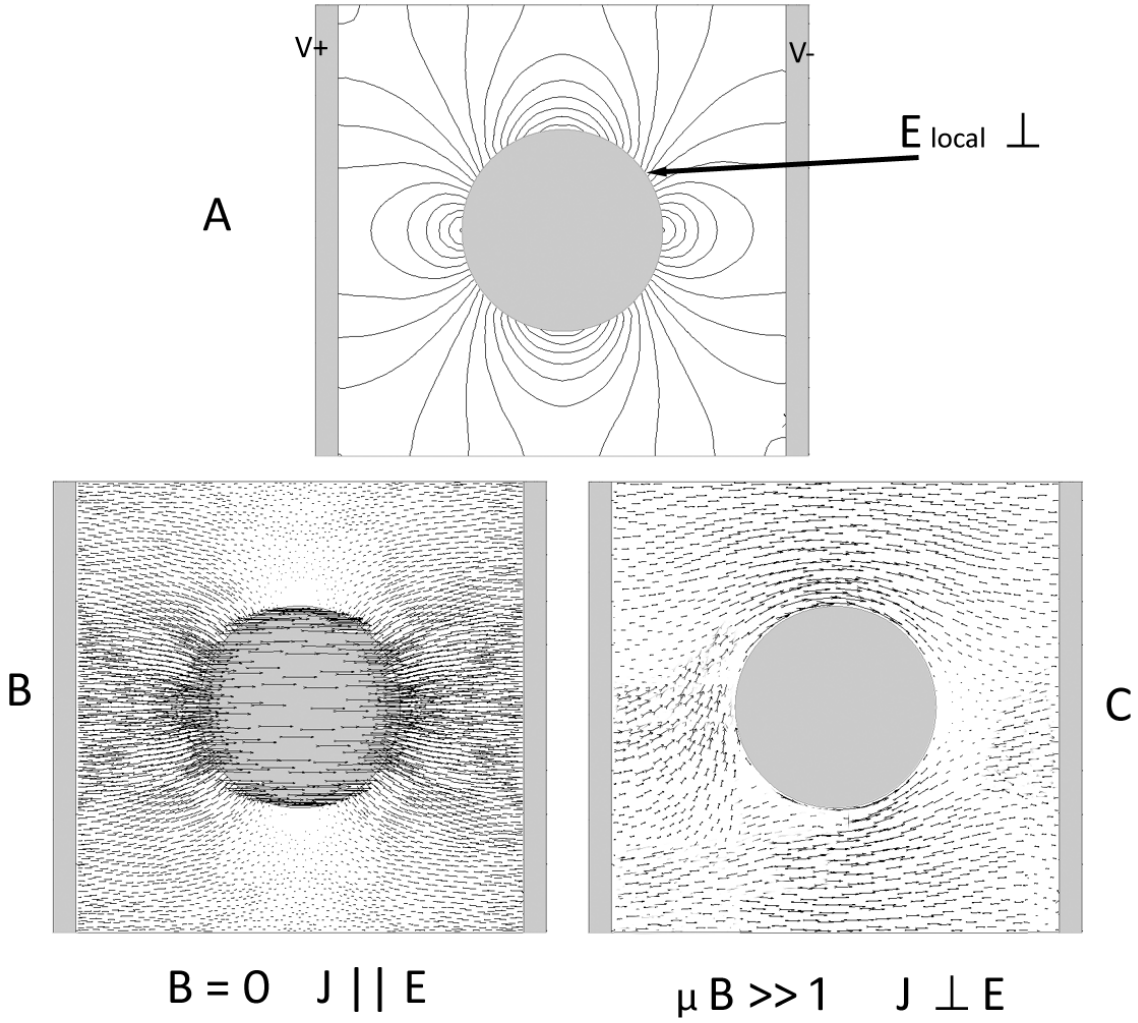

Fig. 2-4 The EMR effect in a high mobility semiconductor-metal hybrid. (A) For $\sigma_m >> \sigma_s$ the local electric field at is orthogonal to the metal-semiconductor interface. (B) In a zero magnetic field the current density vector (J) is parallel to the electric field (E). For large magnetic fields (C) the Hall angle approaches 90° (J ⊥ E) and the current is deflected away from the shunt. Dark lines represent electric field contours in (A), arrows represent current density in (B) and (C). Grey areas represent metallic regions and white areas represent semiconductor regions.

3. Finite-Element Modeling of Extraordinary Magnetoresistance in PSPICE

Methods used to determine electrical characteristics of Hall-effect devices include conformal mapping, solutions of finite-difference equations, classical analytical solutions of the Laplace equation, and approximate expansion for homogenous hall plates as a function of the L/W ratio [12, 19, 20]. However, theoretical derivations are difficult for more complex geometries that include the vdP disk, the shunted Corbino disk, and shunted Hall plates [21]. The numerical solutions can be made accurate but are also computationally expansive and not easy to optimize for a variety of applications.

Another method used to numerically determine the electrical characteristics of a Hall plate consists of the construction a FEM model via a matrix of lumped circuit elements which can be solved using a circuit simulation program such as PSPICE. This method has been demonstrated for a number of device applications which include MOS magnetic field sensors and bipolar magnetotransistors [22]. The development of the circuit model used for the analysis of semiconductor-metal hybrids will be discussed in this section. But first, a conformal mapping procedure commonly used in the design and modeling of EMR devices is described.

3.1 Conformal Mapping

Conformal mapping was first suggested for obtaining analytical solutions to the Laplace equation in two dimension for Hall devices in [23]. It remains a useful analytical tool to transform a complex geometry into a simpler or more useful one. The resulting

transform has advantages for analytical calculations, finite element methods (FEM), manufacturing, and practical implementation of devices in series and parallel [24, 25]. The bilinear conformal mapping will be presented and demonstrated in this section.

3.1.1 The Bilinear Transform

A circular device of unit radius in the 2-D complex *t* plane with perpendicular axes *r* and *is* where *t = r +is* can be mapped onto the complex positive half Cartesian *z* plane with perpendicular axes *x* and *iy* where *z = x +iy* by applying the bilinear transform

The real and imaginary parts of z are expressed by

$$z(t) = -i\left[\frac{t+i}{t-i}\right]. \tag{3.1}$$

where

$$\mathrm{Re}(z) = \frac{1}{2}(z+\overline{z}) \tag{3.2}$$

and

$$\mathrm{Im}(z) = \frac{1}{2i}(z-\overline{z}) \tag{3.3}$$

Under this transformation, each point on the perimeter of a unit circle in the *t* plane is mapped to the y = 0 line in the *z* plane as in Fig. 3-1. The utility of this transform is that it produces a simple rectangular and electrically equivalent device from a circular, more complex structure. This technique will be illustrated with a real device in the next section.

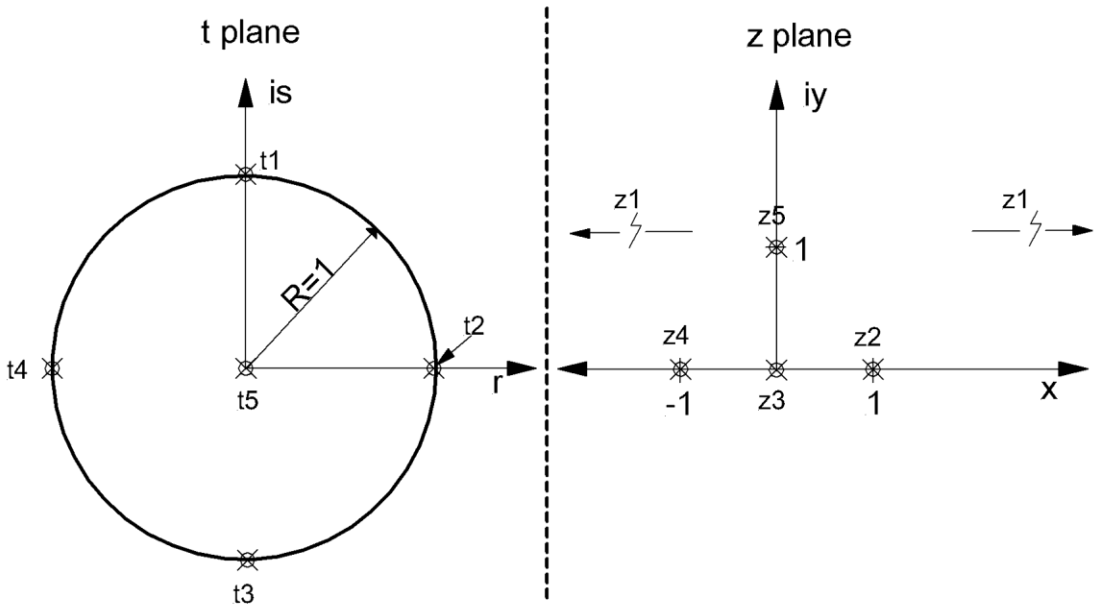

Fig. 3-1 The bilinear transform of (3.1) applied to principle points of the unit circle. Here points t_i in the t plane map to points z_i in the z plane. Point t1 (r=0, s=1) maps to x = +/- infinity.

3.1.2 Finite Cuts and Associated Error

Since (3.1) maps real points in the *t* plane to infinity in the *z* plane, several modifications or cuts must be made to the *t*-plane device in order to produce a practical and finite device in the *z* plane. In practice, bounds are introduced into the *z*-plane region and mapped back to the *t*-plane to view the results on a disk shaped device. The first cut eliminates the *z*-plane for all Im(z) > y_1 as in Fig. 3-2(D). Mapping back into the t plane is done by eliminating the real part of (3.1), substituting (3.1) into (3.3), $t\,\bar{t} = r^2+s^2$, and Im(z) = y_1. This leaves an equation for a circle in the t plane centered at (0, $y_1/(y_1+1)$), with radius

$$R_1 = \frac{1}{y_1 + 1}. \tag{3.4}$$

This circular cut is shown in Fig. 3-2(A). In a similar manner, the elimination of all Re(z) > x_2 in the *z* plane is done by eliminating Im(z) from (3.1), substituting (3.1) into (3.2), and Re(z)=x2. This gives the equation for a circle shown centered at ($1/x_2$, 1) with radius

$$R_2 = \frac{1}{x_2} \tag{3.5}$$

as shown in Fig. 3-2(B). The same procedure performed for all Re(z) < x3 results in the circle C3 in Fig. 3-2(C).

Since the modified t-plane device in Fig. 3-2(C) is not identical to the original there will be some error in the resistance of the z-plane device when compared to the unmodified parent disk. One method to estimate the error introduced is to assume a relatively uniform current density in the parent disk. Under this assumption, the resistance of the modified disk is increased by an amount proportional to the total area of the cuts made. The error or change in resistance due to the cuts is then given by

$$\frac{\Delta R_m}{R_p} \lesssim \frac{A_1 + \frac{1}{2}(A_2 + A_3)}{A}. \tag{3.6}$$

where ΔR_m is the change in resistance due to the cuts, R_p is the resistance of the unmodified parent device, and A_i is the area corresponding to circular cut C_i as in Fig. 3-2. This treatment follows that in [9], where more detail can be found.

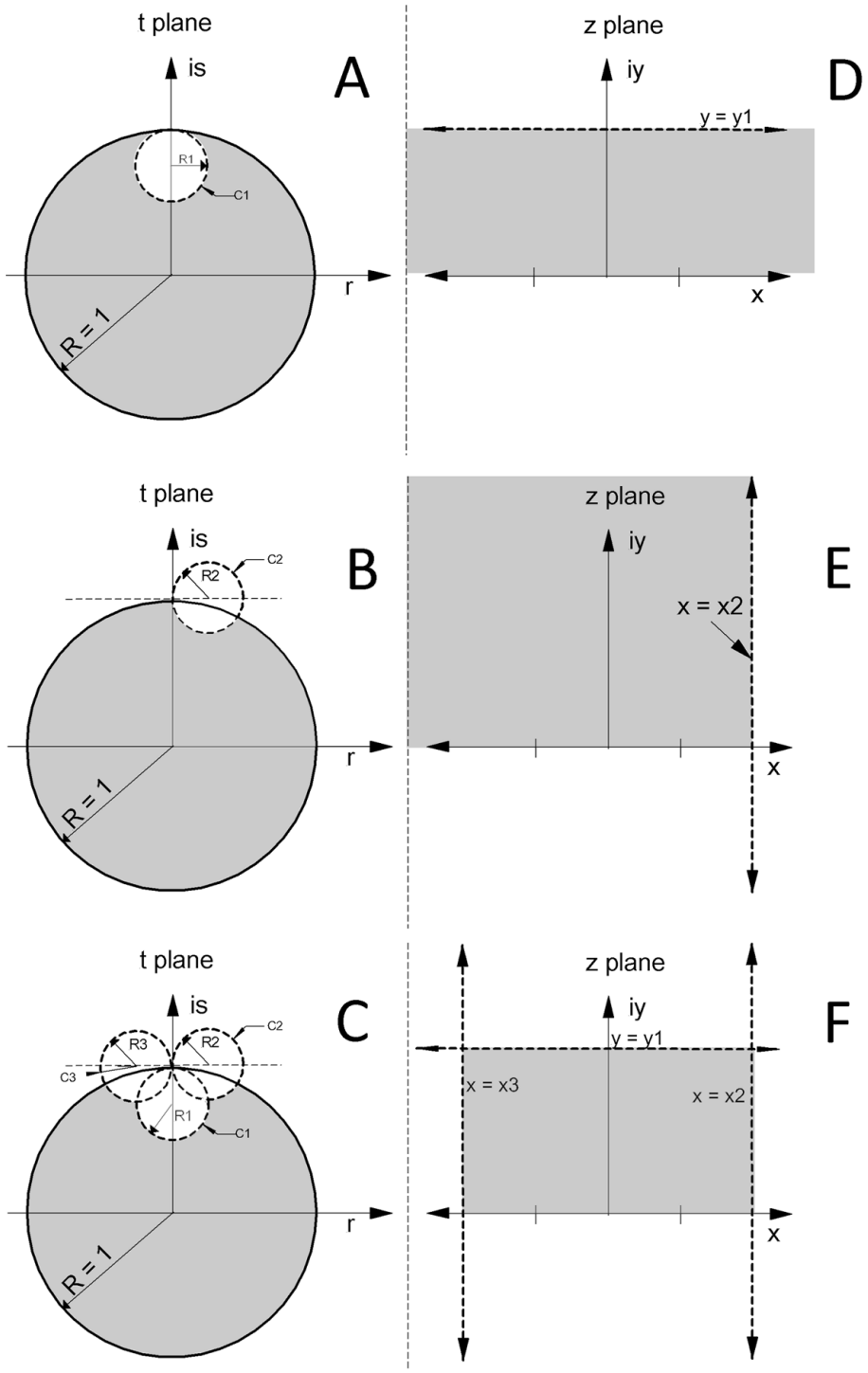

Fig. 3-2 Cuts taken (dashed lines) from the *z*-plane device (D-F) ensuing from the bilinear transform in (3.1), mapped back onto the parent *t*-plane device (A-C). These cuts must be made in the parent device to ensure the transformed device is finite.

It has been shown in [25] and [20] that the EMR displayed by a symmetric internally-shunted vdP disk can also be obtained by a rectangular, electrically equivalent and externally-shunted structure derived via the bilinear transformation. The mapped, externally shunted device allows simpler analytical solutions, it is easier to model in FEM or finite-difference analysis, permits simpler fabrication, and it is easier to integrate multiple devices in series or parallel [20]. The bilinear conformal mapping is especially useful for mesoscopic magnetic sensor applications since the traditional circular geometry is not feasible for fabrication.

3.2 Finite-element Model Assumptions and Basic Equations

Several assumptions are made in the construction of the finite-element model:

- The device is uniform in the z direction.
- The magnetic field is completely transverse (B_x, B_y=0) and uniform over the active area of the device.
- The physical contribution to the MR of the device is neglected in cases where the geometric effect dominates.
- Each material's mobility is magnetic-field independent.

The general equation governing current flow can be simplified in the case of the uniform perpendicular magnetic field (assumption 2) by dropping the planar field term. The simplification is detailed in [11]. This leaves the current density in the region described by any component cell in the circuit as

$$J_n = \frac{1}{1+(\mu_n B)^2}\left[\left(q\mu_n n\vec{E} + qD_n\nabla n\right) + \mu_n\vec{B}\times\left(q\mu_n n\vec{E} + qD_n\nabla n\right)\right] \tag{3.7}$$

where *n* is the local electron density, *D* is the diffusion coefficient of electrons, and μ_n is the electron mobility. The local electric field in 2-D is given by

$$\vec{E} = \nabla V(x, y). \tag{3.8}$$

Substituting (3.8) into the (3.7) and integrating over the thickness (z) the two dimensional equations become:

$$J_{nx} = \frac{1}{1 + (\mu_n B)^2} (J_{nox} + \mu_n \, B \, J_{noy}) \tag{3.9}$$

$$J_{ny} = \frac{1}{1 + (\mu_n B)^2} (J_{noy} + \mu_n \, B \, J_{nox}) \tag{3.10}$$

where J_{nox} and J_{noy} are the respective current densities in the x and y directions of the cell in the absence of a magnetic field and (3.3) and (3.4) are subject to the condition

$$\frac{dJ_{nx}}{dx} + \frac{dJ_{ny}}{dx}. \tag{3.11}$$

(3.9) and (3.10) can be converted into finite-element form by introducing the general finite line segments Δx and Δy so that

$$\Delta I_x = \frac{1}{1 + (\mu_n B)^2} \left(\Delta I_{xo} + \mu_n \, B \, \frac{\Delta y}{\Delta x} \, \Delta I_{oy} \right) \tag{3.12}$$

$$\Delta I_y = \frac{1}{1 + (\mu_n B)^2} \left(\Delta I_{yo} + \mu_n \, B \, \frac{\Delta x}{\Delta y} \, \Delta I_{ox} \right) \tag{3.13}$$

and

$$\Delta I_x + \Delta I_y = 0. \tag{3.14}$$

Next, in order to generate a form more suitable for implementation in the circuit model, the following substitutions are made

$$\Delta I_{ox} = \frac{\Delta V_x}{R_x} = \frac{\Delta V_x \sigma A_x}{\Delta x} \tag{3.15}$$

$$\Delta I_{oy} = \frac{\Delta V_y}{R_y} = \frac{\Delta V_y \sigma A_y}{\Delta y} \tag{3.16}$$

so that (3.7) and (3.8) can be written as

$$\Delta I_x = \left(\frac{\sigma_{xx} A_x}{\Delta x}\right) \Delta V_x + \left(\frac{\sigma_{xy} A_y}{\Delta y}\right) \Delta V_y \tag{3.17}$$

$$\Delta I_y = \left(\frac{\sigma_{yy} A_y}{\Delta y}\right) \Delta V_y + \left(\frac{\sigma_{yx} A_x}{\Delta x}\right) \Delta V_x \tag{3.18}$$

where A_x and A_y are the cross-sectional areas normal to the x and y directions respectively. The effective conductivity matrix is then written as

$$\overline{\boldsymbol{\sigma}} = \begin{bmatrix} \dfrac{\sigma}{1+(\mu B)^2} & \dfrac{\sigma \mu B}{1+(\mu B)^2} \\ \dfrac{\sigma \mu B}{1+(\mu B)^2} & \dfrac{\sigma}{1+(\mu B)^2} \end{bmatrix} \tag{3.19}$$

A circuit model that obeys (3.17) and (3.18) can be constructed using conventional elements in the unit cell of an electrical network as in Fig. 3-3. The current controlled by the resistor elements, R_x and R_y in the model is due to drift and diffusion and modified by the MR effect through the diagonal σ_{xx} and σ_{yy} terms from (3.19). The effect of the magnetic field is simulated by the two voltage controlled current sources F_{xy} and F_{yx} which apply the gain represented by theoff-diagonal σ_{xy} and σ_{yx} terms to the voltage sensed across the element normal to the direction of current flow. For example,

$$I(F_{xy}) = \left(\frac{A_y \sigma_{xy}}{\Delta y}\right) [V(y_1) - V(y_2)]. \tag{3.20}$$

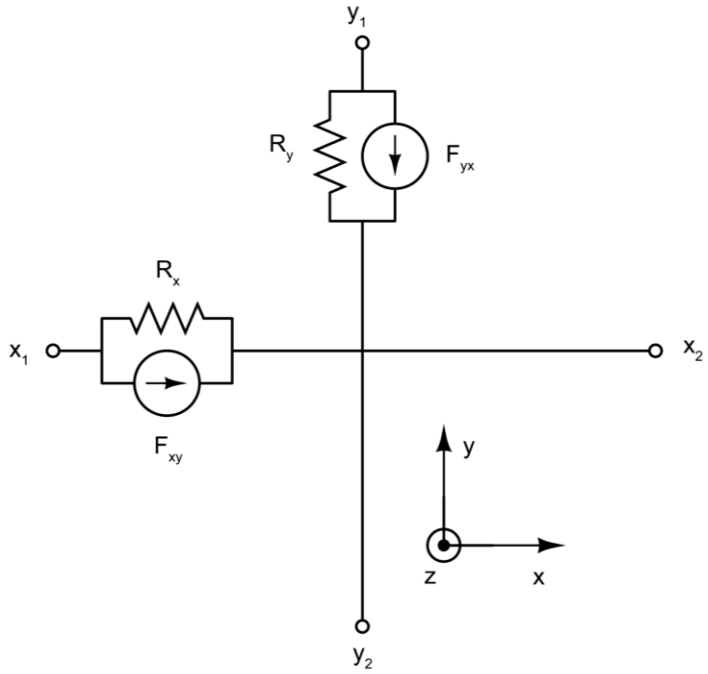

Fig. 3-3 Semiconductor unit cell of the finite-element model showing the conventional elements: a resistor and a current source for the x and y dimensions.

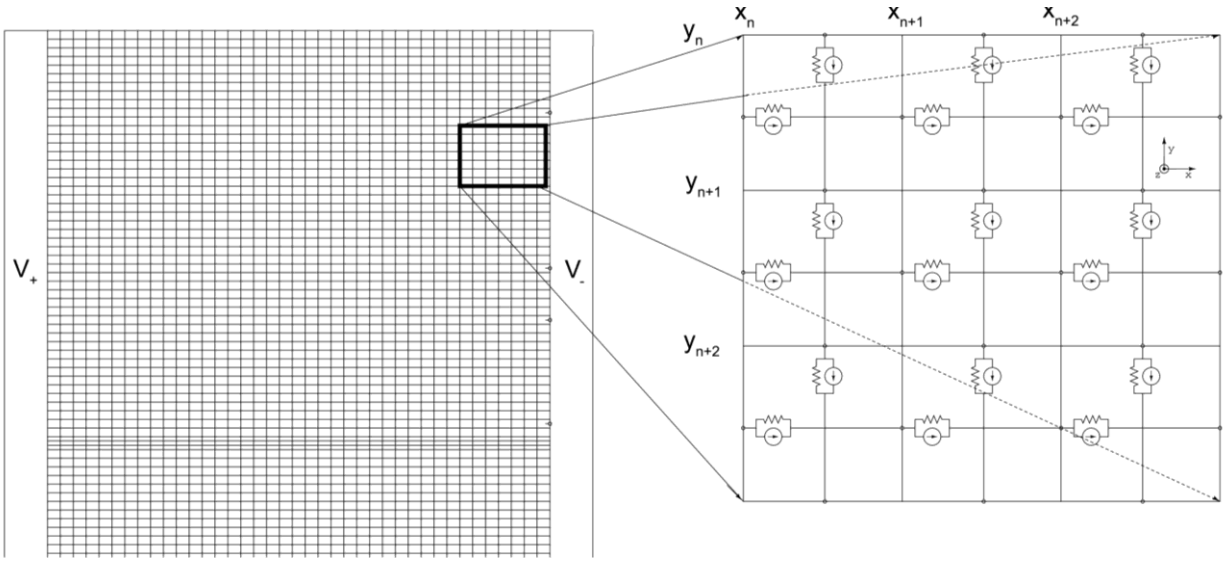

Fig. 3-4 Electrical network used to model the electrical properties of a simple Hall plate with inset of constituent unit cells.

Upon construction of a circuit model tailored to the geometry of the device under consideration, all that is left is to solve the associated boundary value problems with a

circuit-analysis program such as PSPICE. In this way it is easy to incorporate both simple and magnetic field dependant circuit elements into a simulation. The scheme of implementing this for a simple hall plate is shown in Fig. 3-4.

4. PSPICE FEM Calculations of Magnetoresistance in the Externally-Shunted van der Pauw Plate

In order to assess the FEM described in the previous section and contrast the 2-point and 4-point resistance in an EMR sensor, a model was generated to study an externally-shunted van der Pauw (vdP) plate. This device geometry was chosen so the results could be gauged against previous measurements and the well documented 4-point resistance could be compared to the 2-point resistance [24, 25]. The externally shunted vdP plate is the result of a bilinear conformal mapping applied to a symmetric internally-shunted vdP disk, as described in [25]. This device consists of n-type InSb as the bulk semiconductor and an external metal shunt as shown in Fig. 4-1. Typical modeled-device properties are listed in Table 4-1. The following sections will present the effect of shunt conductivity, semiconductor mobility, and semiconductor carrier density on the device resistance and MR as measured in the 4-point configuration and the 2-point configuration. The default device dimensions are labeled in Fig. 4-1 and listed in Table 4-1.

The original vdP disk traditionally employs a four-probe resistance measurement where current is injected in two contacts on one side and the voltage is measured across two contacts symmetrically placed on the opposite side. After the bilinear transform (3.1) is applied to the parent disk, the equivalent resistance measurement requires both current injection and voltage contacts to appear on the bottom surface of

the externally-shunted vdP disk as in Fig. 4-1. The resistance associated this 4-terminal probe configuration is here called the 4-point resistance or R_{4p}.

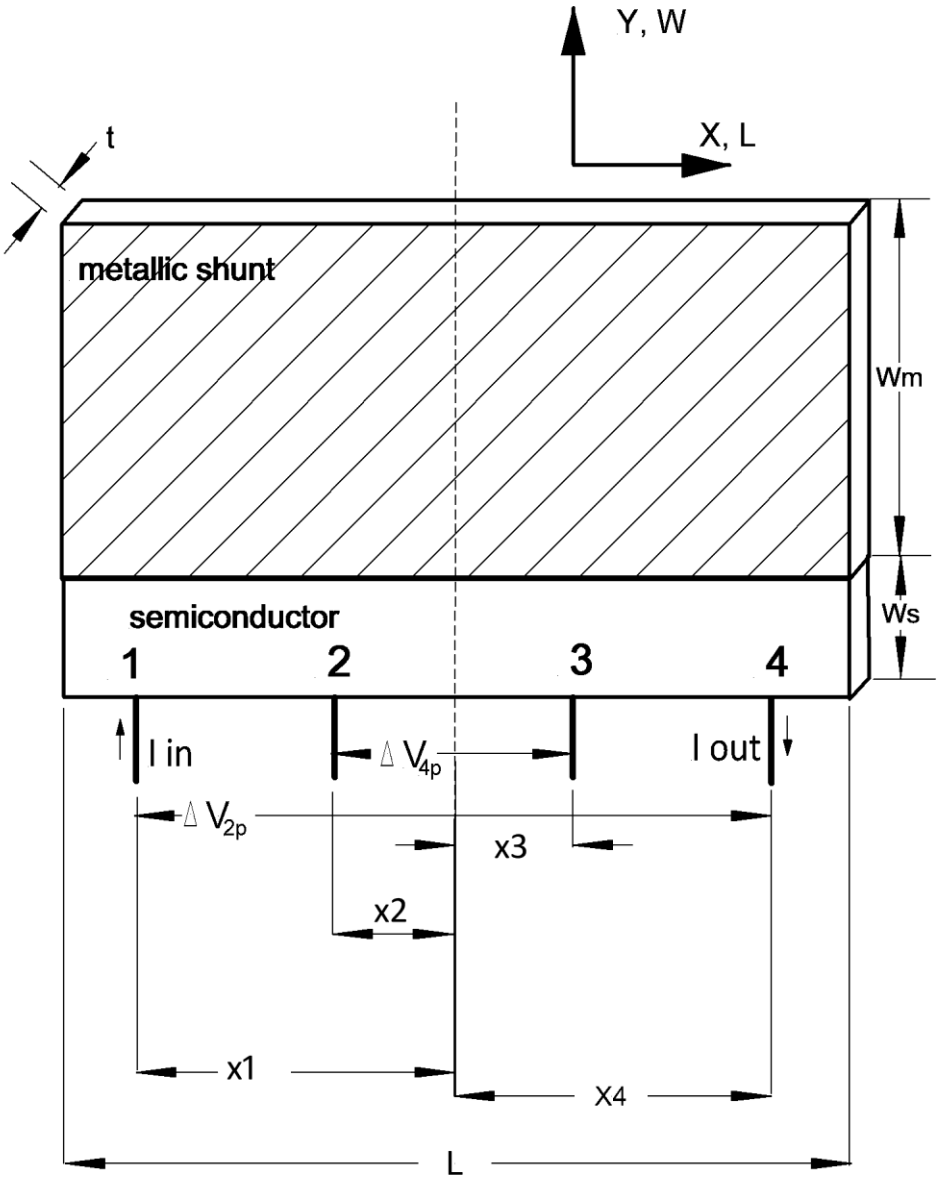

Fig. 4-1 Diagram of the modeled externally shunted vdP plate. The default dimensions of the device are: [L=2140 µm, T=1.30 µm, Ws=300 µm, Wm=900 µm, x1=336 µm, x2=336 µm, x3=795 µm, x4=795 µm].

The 4-point resistance and corresponding MR is measured by the potential difference measured between points 2 and 3 divided by the current injected at points 1

and 4. In contrast, the 2-point device resistance (R_{2p}) is defined by the voltage across the current injection contacts or

$$R_{4p} = \Delta V_{2,3}/I_{1,4} \tag{4.1}$$

$$R_{2p} = \Delta V_{1,4}/I_{1,4}. \tag{4.2}$$

TABLE 4-1 MODEL PARAMETERS AND TYPICAL VALUES FOR EXTERNALLY-SHUNTED VDP PLATE

Model Parameter Symbol	Description	Default Value	Units
Bmag	transverse magnetic field magnitude	0	T
t	thickness (z)	1.3	µm
L	semiconductor region length (x)	2140	µm
W	semiconductor region width (y)	900	µm
µ	semiconductor mobility	4.02	m^2/Vs
n	semiconductor carrier density	2.11×10^{22}	m^{-3}
N_y	number of semiconductor cells in the y direction	32	-
N_x	number of semiconductor cells in the x direction	70	-
W_m	shunt width (y)	2140	µm
L_m	shunt length (x)	300	µm
μ_m	shunt mobility	5.3×10^{-3}	m^2/Vs
n_m	shunt carrier density	5.90×10^{28}	m^{-3}
N_{ym}	number of shunt cells in the y direction	18	-
N_{xm}	number of shunt cells in the x direction	70	-
σ_o	semiconductor conductivity	$nq\mu$	$S\ m^{-1}$
σ_{om}	shunt conductivity	$n_m q \mu_m$	$S\ m^{-1}$
R_{sub}	non-contact boundary resistance	10^9	Ω

The actual PSPICE schematic showing both semiconductor and shunt regions, terminal locations, bias current source, and parameter table is shown in

Fig. 4-2. In the PSPICE interface, the user controls the number of hierarchical blocks in the schematic which generates the net list.

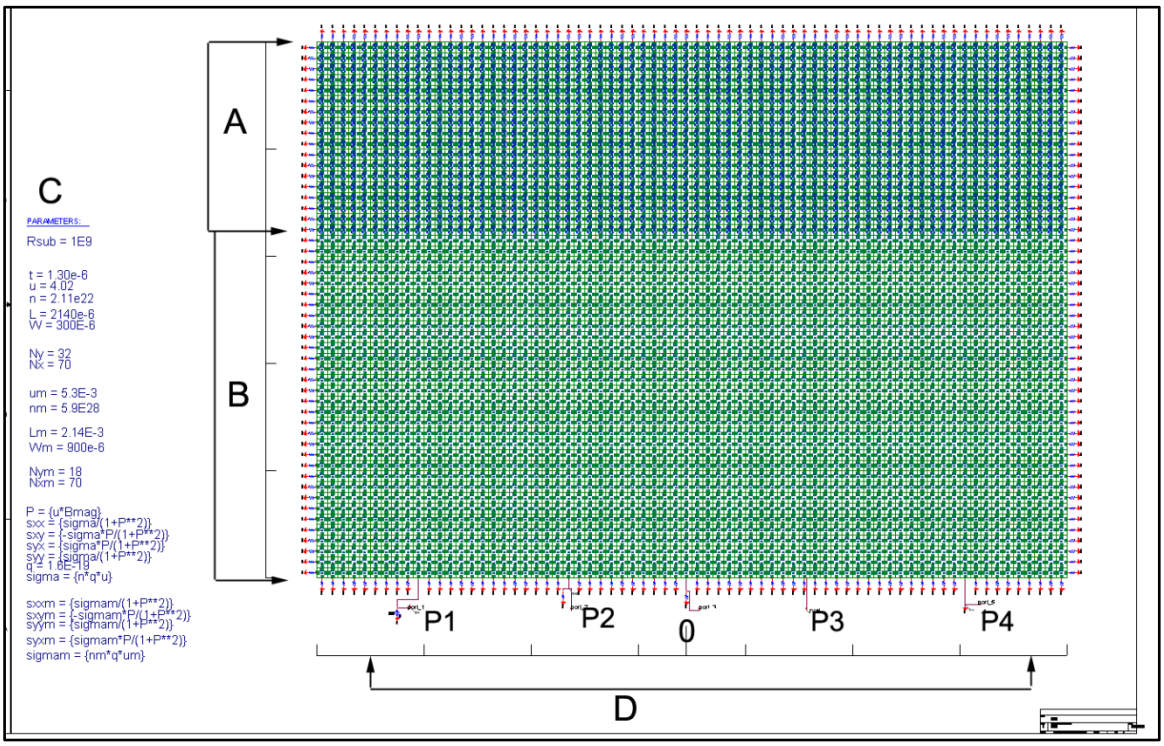

Fig. 4-2 Screen capture of PSPICE schematic showing (A) shunt region, (B) semiconductor region, (C) parameter input table, and (D) terminal locations(Pi). The parameters in this schematic are listed in Table 4-1.

Each hierarchical block contains one or more unit cells that represent the appropriate material's material properties and response to magnetic field. At the outer device boundary each hierarchical block is referenced to ground through a large resistor representative of the substrate material. At the interface between semiconductor and shunt, a contact resistance can be represented by installing a single layer of pre-defined resistive elements. In this examination the contact resistance was considered to be zero

in order to isolate the effects of other material properties, but previous FEM efforts have shown its effect on EMR [24]. The material parameters listed in Table 1 can all be adjusted and independently varied to view its effect on device performance.

4.1 The Effect of Probe Position on Device Resistance

The probe position of a conformally mapped vdP plate is determined by the probe placement on the parent disk and its size. The effect of probe position in an externally shunted vdP plate has been reported in [25] where it was shown that an asymmetric probe placement can result in larger MR values than the placement ensuing from mapping symmetric probe positions.

Since the 4-point behavior has been well addressed in the literature and the 2-point behavior is relevant to power applications, the two configurations will be compared in the following sections. First, to show the sensitivity of the device to probe placement, the voltage was probed at x3, referenced to the plate's midpoint at x2 = 0 as labeled in Fig. 4-1. The resistance was recorded as a function of magnetic field for selected set of x3 values. The resulting resistances R(B,x3) are shown in Fig. 4-3 for transverse magnetic field magnitudes between -1 and 1 T.

As in Fig. 4-3, the minimum resistance point shifts to more negative B, as the point-3 probe position moves further away from the center. The two probe positions with distinctly different behavior are the two positions outside of the current injection point where x3 > x4. For these values of x2, the negative value indicates a change in polarity of the $\Delta V(x2 > x4)$ factor in the resistance as defined by (4.1) and (4.2). This result

displays the extremely large and asymmetric MR that can be obtained by the externally-shunted vdP plate in applications that can utilize a 4-point resistance measurement, e.g. magnetic field sensing.

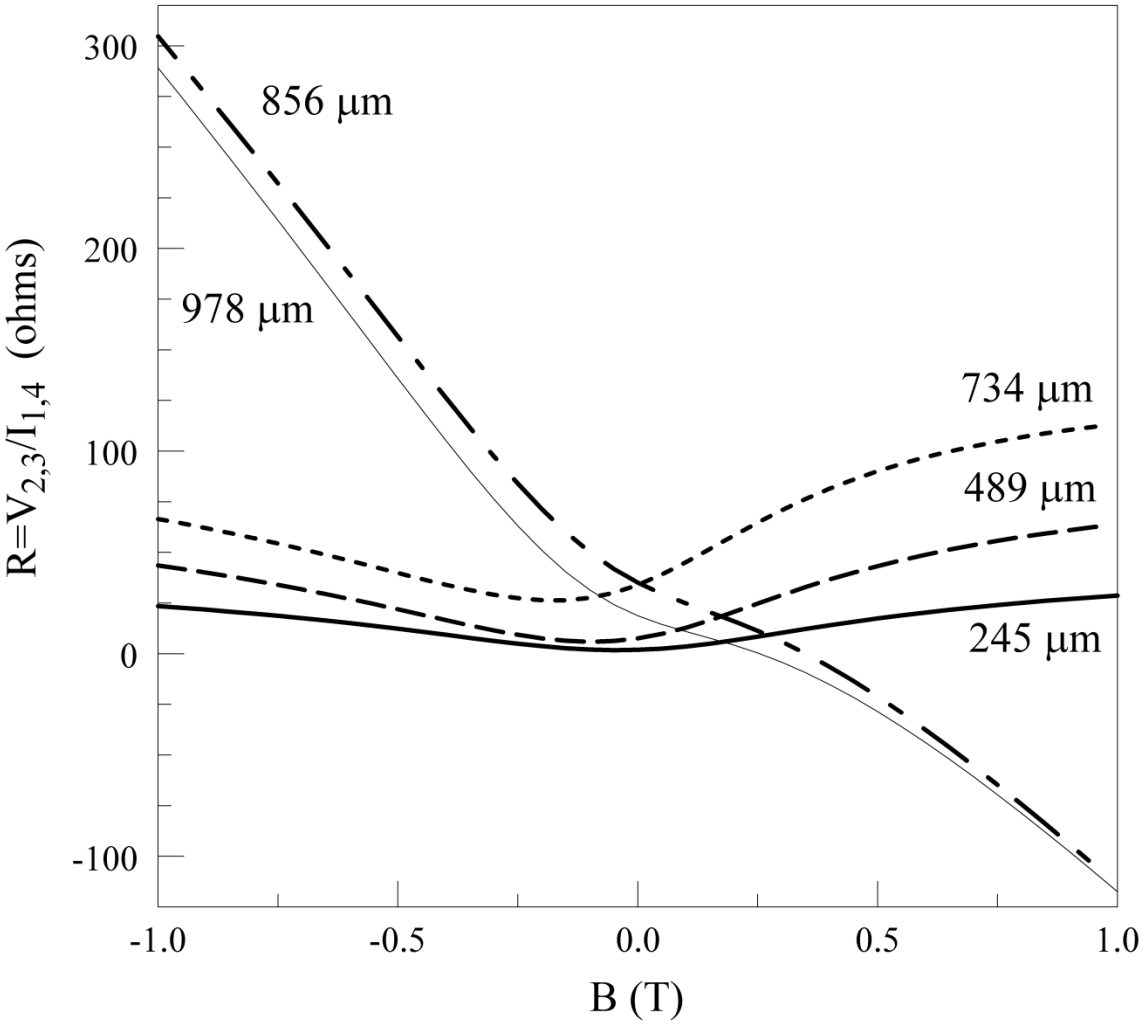

Fig. 4-3 Resistance as a function of transverse magnetic field and the position of probe 3 (x3) with respect to midpoint (x2 = 0 in Fig. 4-1). The current injection points (1 and 4) are held at constant position Resistance traces are labeled in the plot by the corresponding value of x3.

4.2 The Dependence of Magnetoresistance on Semiconductor Mobility and Carrier Density

The semiconductor mobility enters the model through the Drude conductivity ($\sigma = nq\mu$) and the Hall effect as described by the conductivity matrix of (3.19). In this model, the mobility and the carrier density can be varied independently. The bulk semiconductor mobility was varied between 0 and 40 m^2/Vs and the symmetric 4-point resistance was probed. Fig. 4-4 shows the effect of semiconductor mobility on R_{4p} for transverse magnetic field magnitudes of 0, 50 mT, 500 mT, and 1 T. For this simulation carrier concentration was kept constant at $n_o = 2.11\times10^{22}$ m^{-3}.

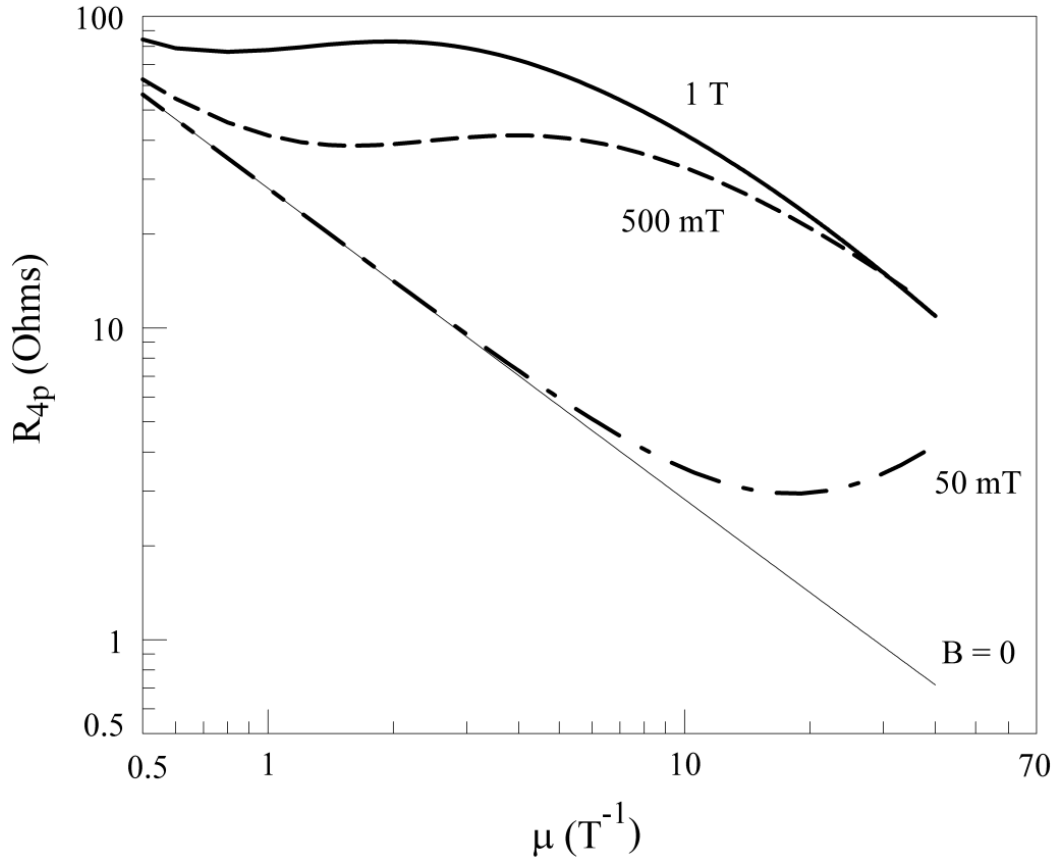

Fig. 4-4 Four-point device resistance as a function of bulk semiconductor mobility. Curves shown are for transverse magnetic field magnitudes of 0, 50 mT, 500 mT, and 1 T.

Using the same device parameters, the resistance is next probed at the current injection contacts to determine the 2-point resistance. Fig. 4-5 shows the 2-point resistance plotted as a function of bulk semiconductor mobility with carrier density held constant as before.

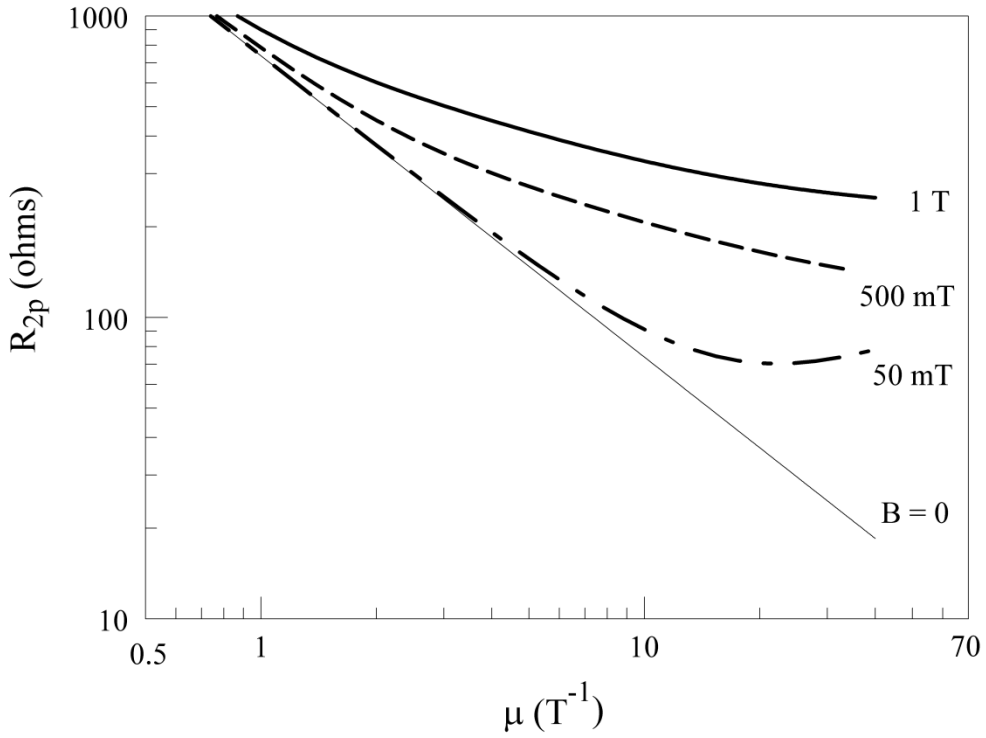

Fig. 4-5 Two-point device resistance as a function of bulk semiconductor mobility. Curves shown are for transverse magnetic field magnitudes of 0, 50 mT, 500 mT, and 1 T.

In both simulations, the zero field resistance decreases with increasing mobility since it is heavily influenced by the Drude conductivity of the bulk semiconductor. The 4-point resistance simulation distinguishes itself not only by a lower resistance value for all values of μ, but also by the presence of local maxima for values of μ >1. These local peaks are more pronounced and shifted toward lower values of μ with increasing field magnitudes as in Fig. 4-4. For very low inductions (50 mT) this peak is not pronounced

as the current path through the semiconductor is minimized. For higher magnetic inductions and large values of μ the current is largely confined to the bulk semiconductor region and the device resistance begins to display the 1/μ dependence that would be expected in the absence of a shunt.

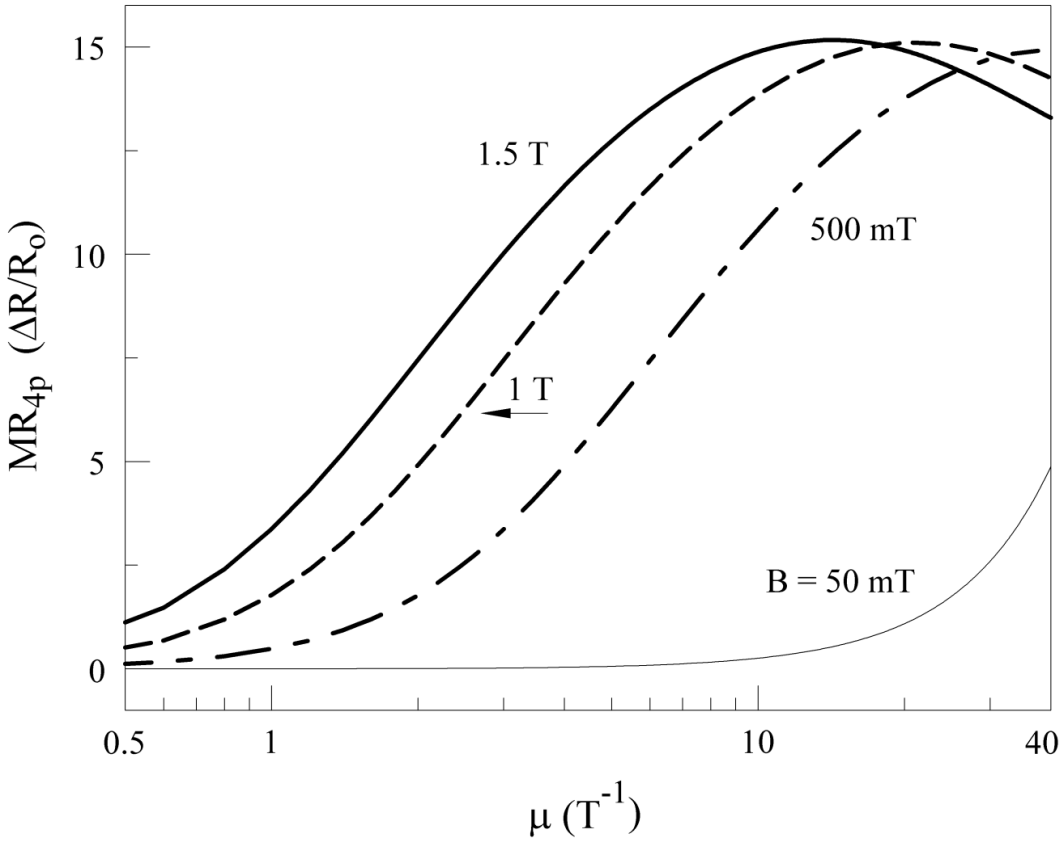

Fig. 4-6 The effect of semiconductor mobility on the 4-point MR of the externally shunted vdP plate. Curves shown are for transverse magnetic field magnitudes of 0, 50 mT, 500 mT, 1 T, and 1.5 T.

The R_{4p} and R_{2p} simulations have corresponding MR measurement here referred to as MR_{4p} and MR_{2p} where,

$$\mathrm{MR_{2p}} = \frac{R_{2p}(B) - R_{2p}(B=0)}{R_{2p}(B=0)} \tag{4.3}$$

and

$$\mathrm{MR}_{4\mathrm{p}} = \frac{R_{4p}(B) - R_{4p}(B=0)}{R_{4p}(B=0)}. \tag{4.4}$$

The 4-point MR of the device in

FIG. 4-6 displays an increasing slope for increasing magnetic fields, and larger values of B result in smaller values of μ at which the MR_{4p} peaks. The 2-point MR shown in Fig. 4-7 is quadratic with low values of the product μB (<1) and approaches a linear relationship with higher values (>1). This behavior follows from the quadratic dependence of the conductivity matrix on the μB product.

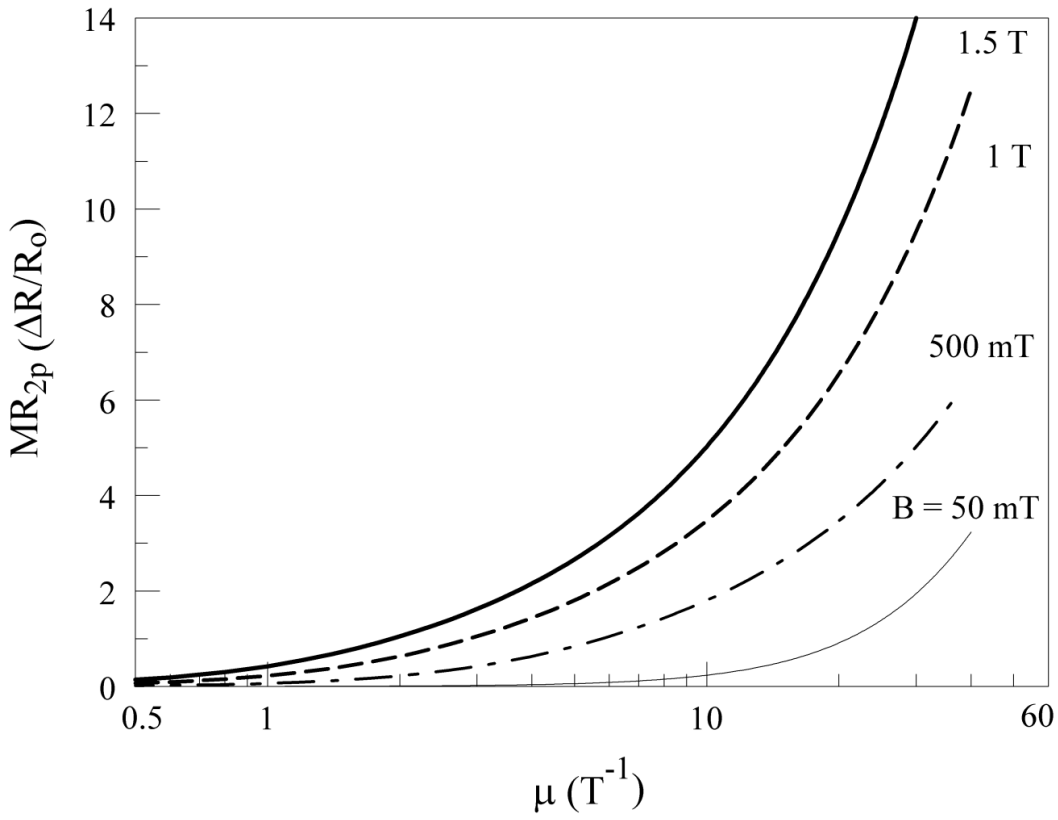

Fig. 4-7 The effect of semiconductor mobility on the 2-point MR of the externally shunted vdP plate. Curves shown are for transverse magnetic field magnitudes of 0, 50 mT, 500 mT, 1 T, and 1.5 T.

The dependence of device resistance on semiconductor carrier concentration is shown in Fig. 4-8 for 4-point configuration and in Fig. 4-9 for the 2-point configuration. In these calculations, the semiconductor mobility (μ) and shunt parameters (μ_m,n_m) are fixed at the values listed in Table 4-1 in order to isolate the influence of carrier concentration.

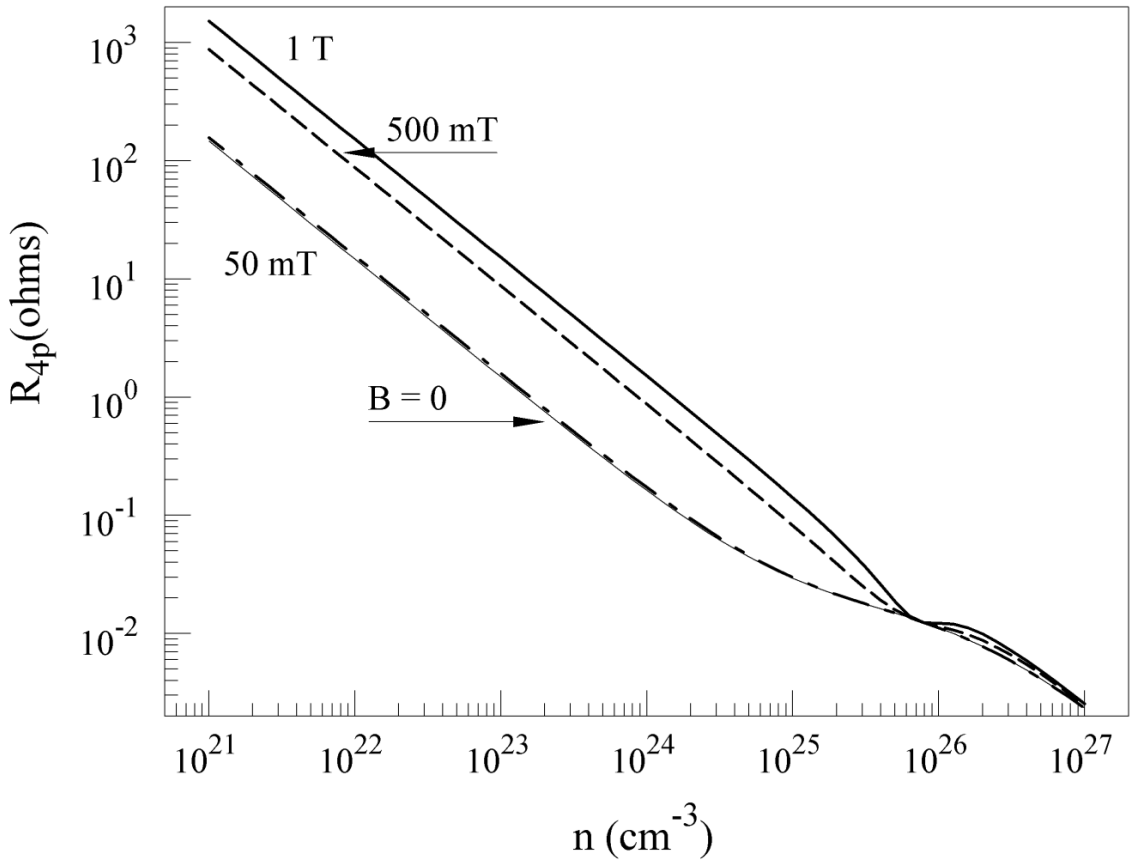

Fig. 4-8 The effect of semiconductor carrier density on the 4-point resistance. As the carrier density approaches n_{crit} =7.8×10^{25} m^{-3} the distinction in device resistance for all listed values of magnetic field disappears.

An increase in carrier density increases the conductivity of the semiconductor thereby decreasing the 2 and 4-point resistance. At a carrier density of n_{crit}=7.8×10^{25} m^{-3} the

conductivity of the semiconductor equals that of the metallic shunt, as a result the magnetic field has little effect on current distribution. As the carrier density approaches n_{crit} the distinction in device resistance for all listed values of magnetic field diminishes.

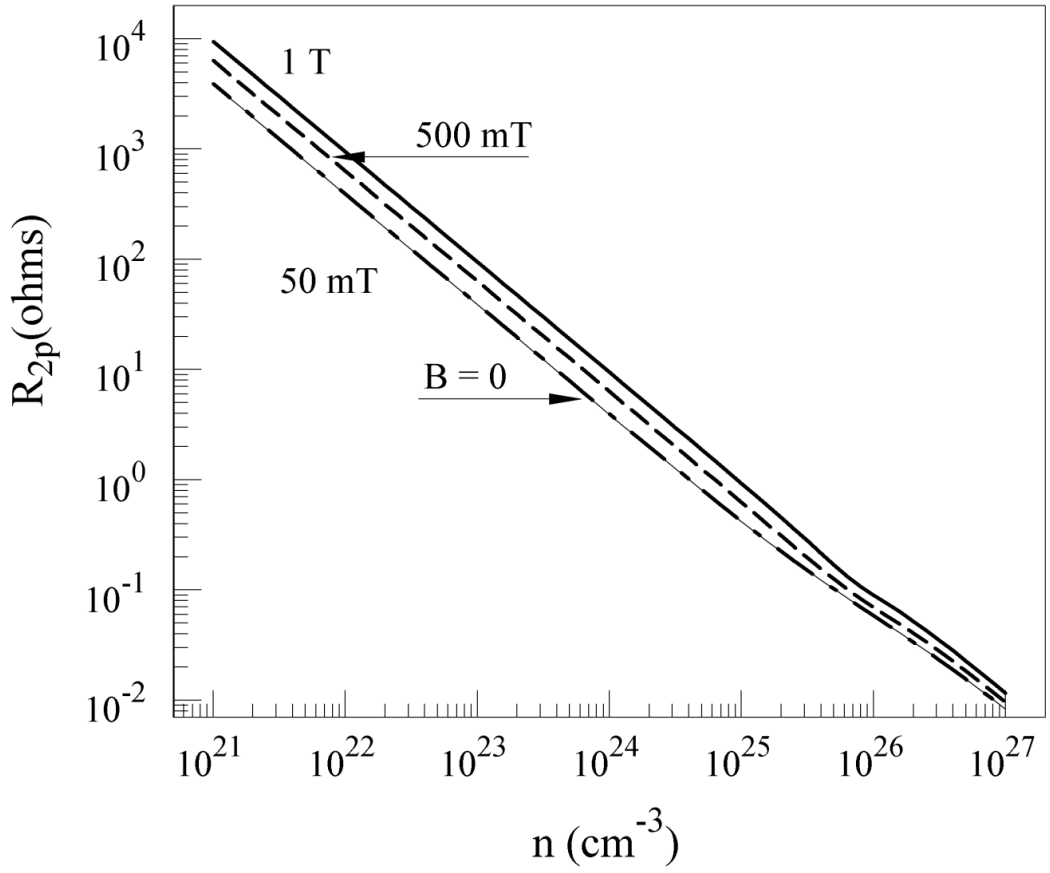

Fig. 4-9 The effect of semiconductor carrier density on the 2-point resistance. As the carrier density approaches n_{crit} =7.8×10^{25} m^{-3} the distinction in device resistance for all listed values of magnetic field diminishes.

This behavior is better illustrated in Fig. 4-10and Fig. 4-11 which display the MR versus carrier density for the 4-point and 2-point configurations respectively. The MR_{4p} goes to zero for all fields as n →n_{crit}. The MR_{2p} is less diminished at n=n_{crit} as the magnetic field

still influences the current path, but the shunt no longer acts as a shunt in either configurations for both $n \sim n_{crit}$ and $n > n_{crit}$.

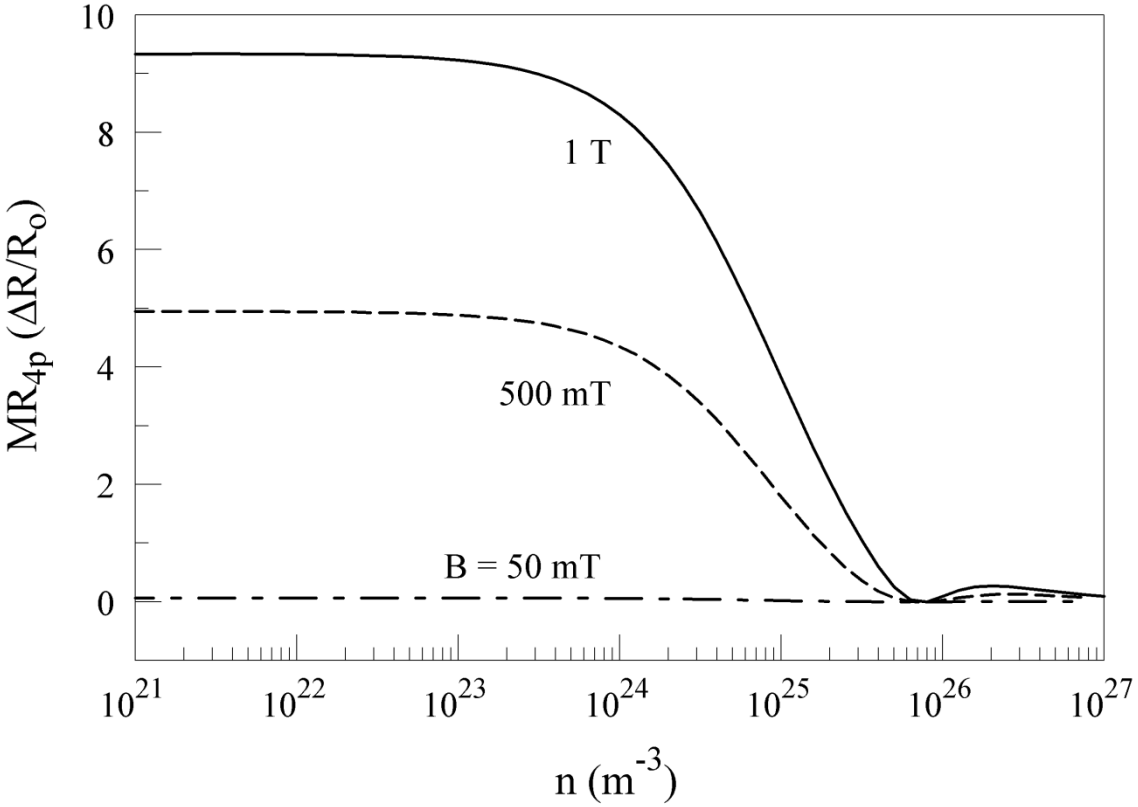

Fig. 4-10 The effect of semiconductor carrier density on the 4-point MR. The MR is essentially constant in the n<< ncrit =7.8×1025 m-3 region, it decays as n → ncrit and is negligible for n ≥ ncrit.

These results illustrate the difference in MR behavior due to the presence of a shunt in a hybrid structure compared to a simple modification of current path length for a homogenous structure. These results also suggests a degree of freedom in device design as the carrier density can be varied over several orders of magnitude (in the $n << n_{crit}$ range) to increase or decrease the device resistance with little or no effect on the device's magnetic sensitivity (dR/dB) and MR for both 2 and 4 point configurations.

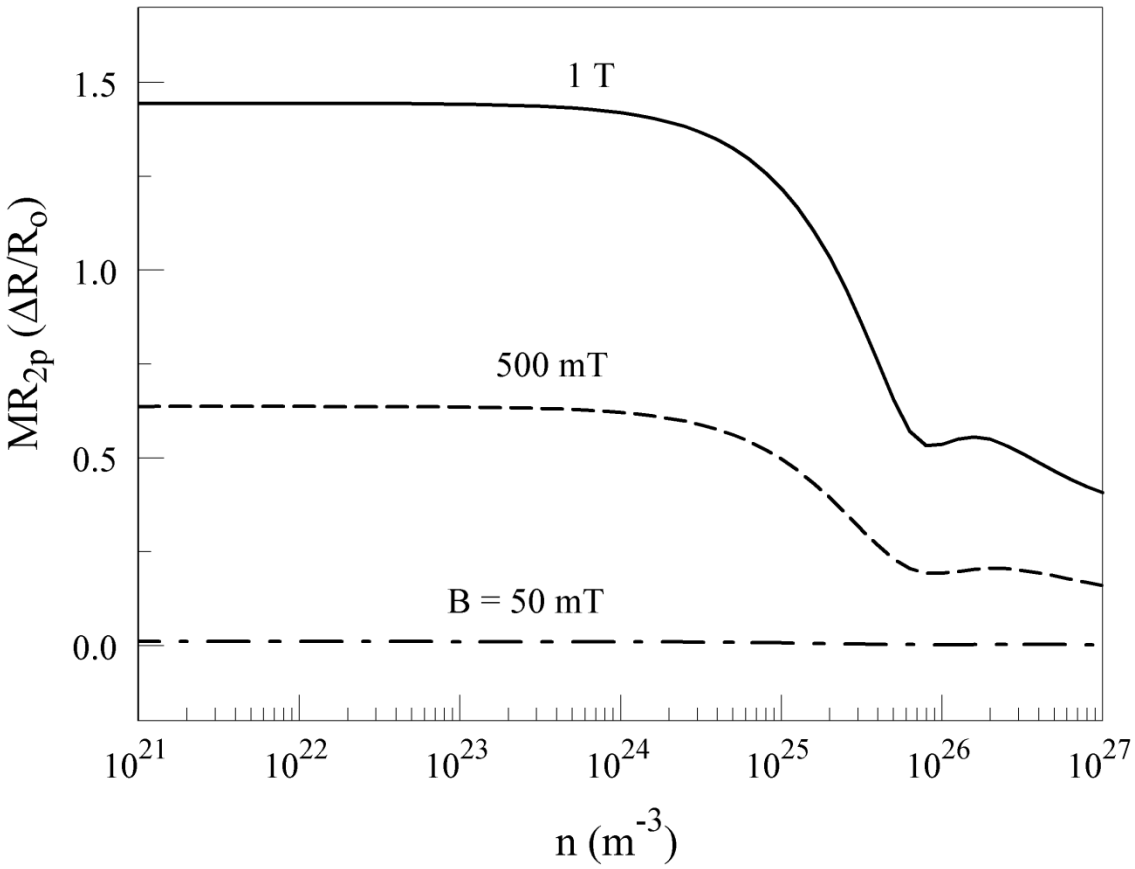

Fig. 4-11 The effect of semiconductor carrier density on the 2-point MR. The MR is essentially constant in the $n << n_{crit} = 7.8\times10^{25}$ m^{-3} region, it decays as $n \rightarrow n_{crit}$ and is minimal, but present for $n \geq n_{crit}$. For carrier densities greater than n_{crit}, the shunt conductivity is lower than that of the bulk semiconductor and thus fails to act as a shunt in a magnetic field, although the current distribution is still affected.

4.3 The Effect of Shunt Conductivity

The conductivity of the metallic shunt shown in Fig. 4-1 is affected by two model parameters: the number of charge n_m carriers or the mobility μ_m. The typical values for each are listed in Table 4-1. The unit cell for the shunt takes into account both n_m and μ_m as opposed to just the conductivity so that the Hall effect is accounted for in the metal region even though it is small when compared the semiconductor region ($\mu >> \mu_m$).

In order to examine the effect of the shunt conductivity, the shunt charge carrier density was varied and all other model parameters were held constant as listed in Table 1. At $n_m = 1.60\times10^{25}$ m^{-3} the corresponding conductivity value is 1.36×10^{4} S m^{-1} which is equal to the conductivity of the bulk semiconductor. This point is apparent in Fig. 4-12 for the 4-point resistance and in Fig. 4-13 for the 2-point resistance; in both cases this value is only a minimum for moderate to high magnetic field intensities.

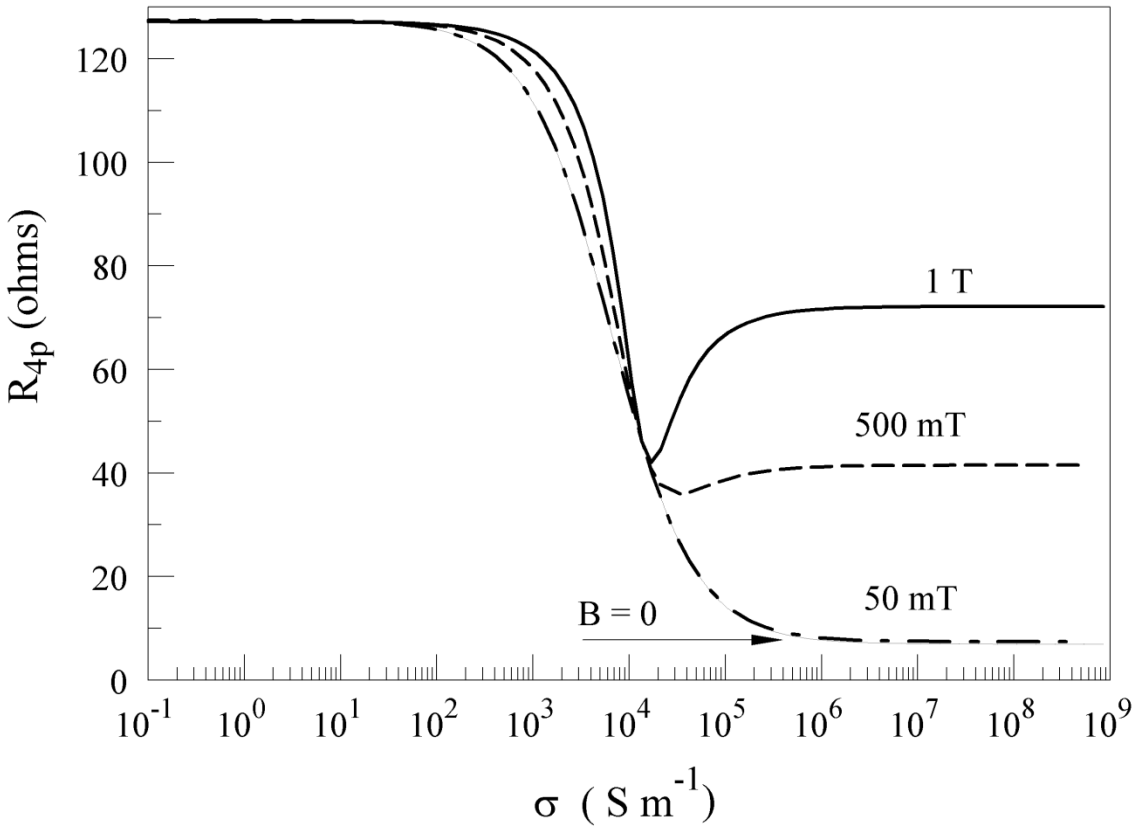

Fig. 4-12 Four-point resistance as a function of shunt conductivity. Minimum resistance values for B ≥ ~500 mT occur when shunt conductivity equals the bulk semiconductor conductivity ($\sigma_m=\sigma$).

In each configuration, the device resistance begins to change only when the conductivity of the shunt approaches the conductivity of the bulk semiconductor. It is in

this range (σ_m~ σ) that small changes in shunt conductivity have the largest effect on device resistance and sensitivity (dR/dB).

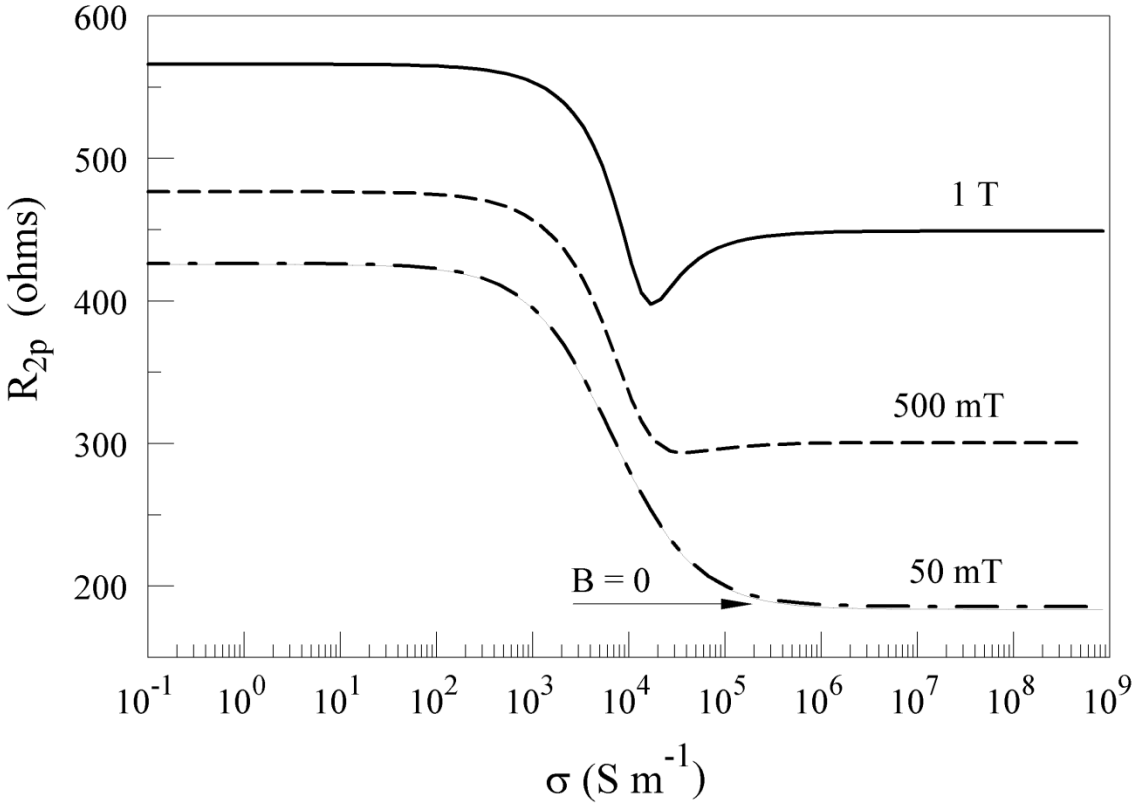

Fig. 4-13 Two-point resistance as a function of shunt conductivity. As with the 4-point resistance plots, minimum resistance values for B > ~500 mT occur when shunt conductivity equals the bulk semiconductor conductivity (σm=σ).

The 4-point resistance becomes strongly dependent upon the magnetic field when the shunt conductivity (σ_m) exceeds the semiconductor conductivity (σ); once σ_m reaches ~100σ no further increase in field dependence is realized. This feature is also illustrated by the variation in MR with shunt conductivity shown in Fig. 4-14 for the 4-point MR and Fig. 4-15 for the 2-point MR. This result implies that extremely conductive

or pure shunt material is not necessary for the device to exhibit enhanced MR, this has previously concluded in [24].

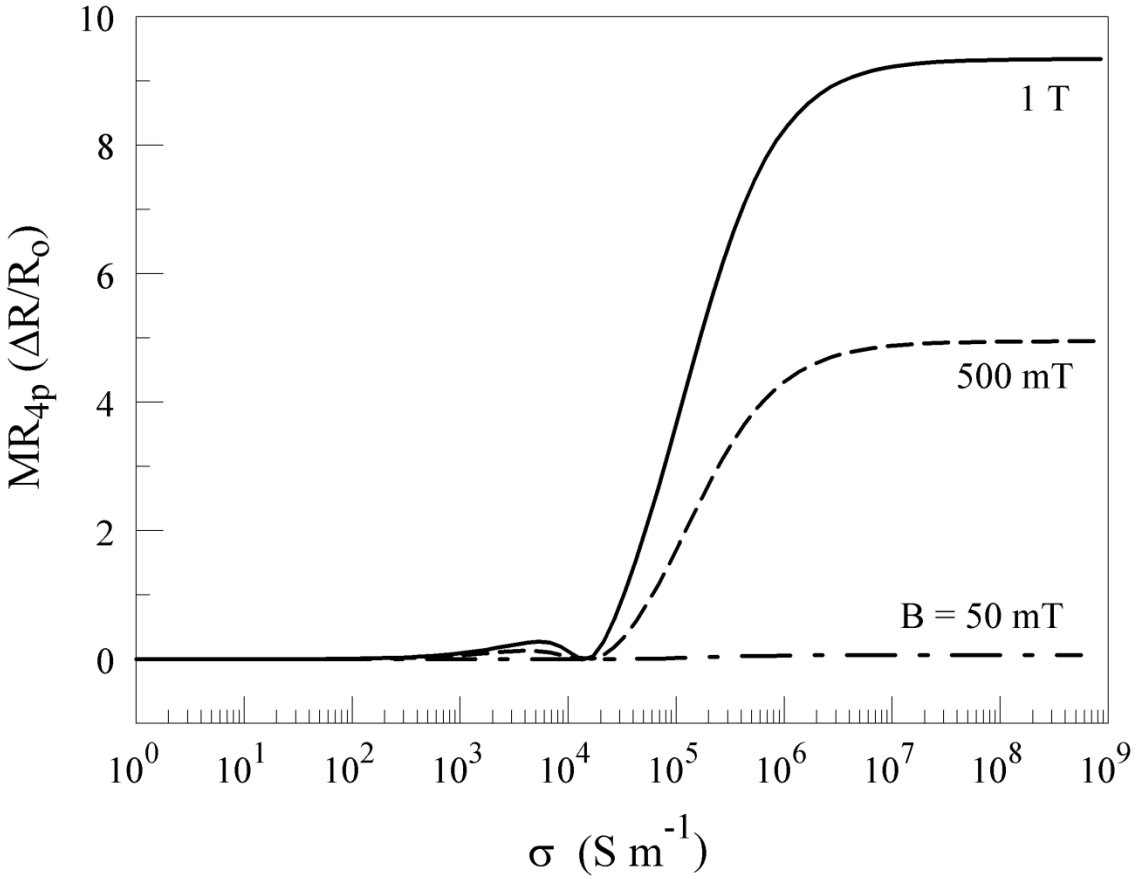

Fig. 4-14 Variation in MR_{4p} with shunt conductivity. For all values of B, the MR does not change until the shunt conductivity approaches the semiconductor conductivity at which point the MR rises rapidly with increasing σ_m. Once $\sigma_m >> \sigma$ no further increase in MR is realized.

One notable feature in this series of calculations is the effect of magnetic field for $\sigma_m << \sigma$. In the 4-point calculation, the magnetic field has a negligible effect on device resistance. For the same shunt conductivity range in the 2-point calculations, the MR is more noticeable, but very small when compared to the $\sigma_m >> \sigma$ range. This illustrates the magnetically induced change in current path length for $\sigma_m << \sigma$ and a change in current path medium for $\sigma_m >> \sigma$. This result quantifies the ability of the magnetic field

to affect the distribution of current for the three general shunt conductivity ranges ($\sigma_m >> \sigma$, $\sigma_m << \sigma$, and $\sigma_m \sim \sigma$).

The primary difference in MR between the 2-point and 4-point is the much higher resistance when probed using the 2-point method. This higher resistance partially accounts for the much lower MR in the 2-point case.

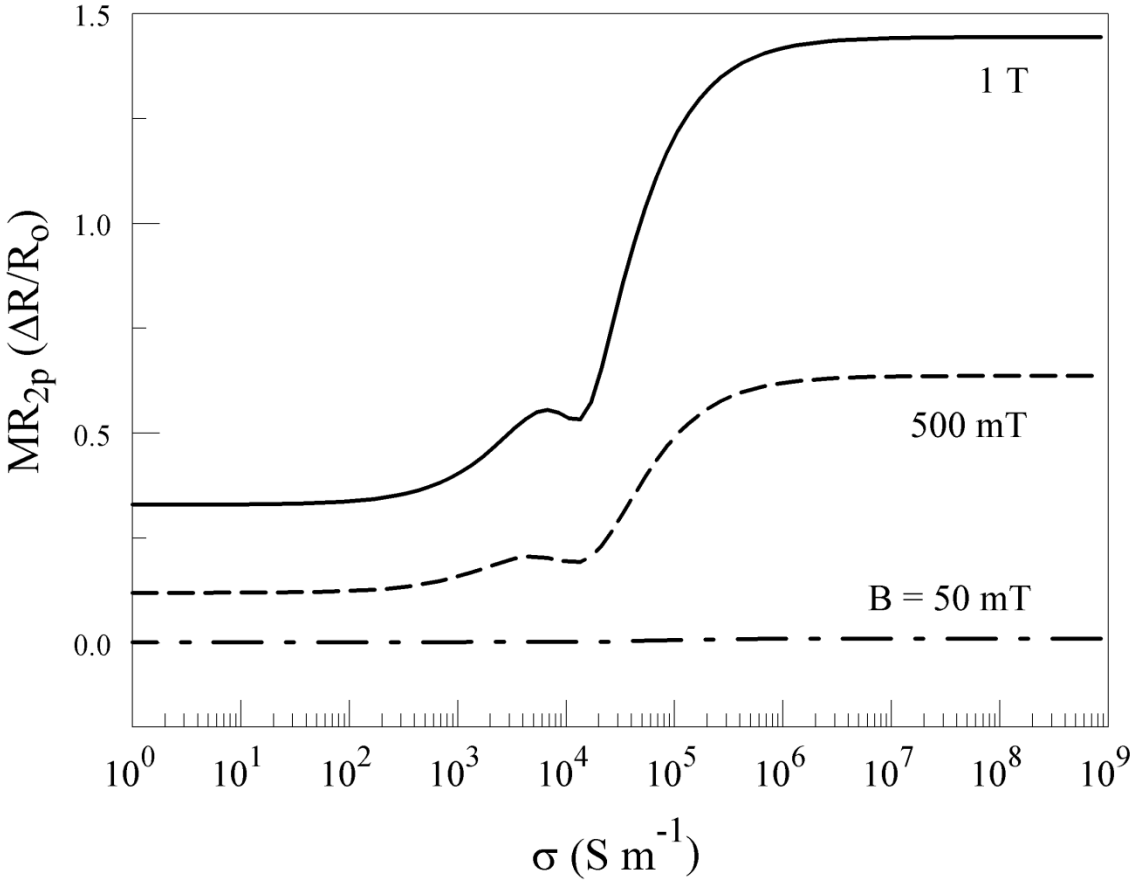

Fig. 4-15 Variation in MR_{2p} with shunt conductivity. For all values of B, the MR does not change until the shunt conductivity approaches the semiconductor conductivity at which point the MR rises rapidly with increasing σm. Once σm >> σ no further increase in MR is realized.

4.4 Summary

The theory and implementation of a PSPICE FEM model for the analysis of semiconductor-metal hybrids have been described. The PSPICE model has the benefit of

being versatile, simple, and computationally stable. The use of a PSPICE program also allows conventional and magnetic field dependent circuit elements to be easily combined into a single circuit. This modeling method was used to analyze the externally-shunted vdP plate which has been of interest for sensor applications for its EMR.

Model results include the effect of probe position, semiconductor mobility, semiconductor carrier density, and shunt conductivity on the resistance and MR. While 4-point results from FEM calculations have been reported previously for EMR devices in [19, 24, 25], the results from this model include a comparison to the 2-point behavior which is of prime importance to any practical power application based on the EMR effect. These calculations show that at 1 T, the 4-point MR is ~5X larger than the 2-point MR for the typical material properties listed in Table 4-1. The results from this finite-element model provide confidence in the model's accuracy and flexibility for its future use in developing optimized geometries for power applications.

5. Prototype Semiconductor-Metal Hybrid Power Devices

Two device topologies were identified as promising candidates for a semiconductor-metal hybrid magnetoresistive power switch. These two device families are here called the shunted Corbino plate (SCP) and the externally-shunted Hall plate (ESHP). In this chapter, the two topologies are described and their origins will be explained. Next, the PSPICE FEM model is used to assess device geometry and semiconductor material properties' effects on resistance and MR. The effect of geometry and material properties on the peak pulsed current and breakdown voltage of these devices are then examined.

5.1 Externally-Shunted Hall Plate

The ESHP is derived from a traditional Hall plate with an embedded circular shunt by applying the bilinear conformal mapping and making post-mapping simplifications. As illustrated by Fig. 5-1, A Hall plate is internally shunted with a circular conductive inhomogeneity. The original internally shunted Hall plate operates on the EMR principle as described in [18]; the shunt acts as an open circuit in high magnetic field and a short circuit in zero field. The bilinear conformal mapping is applied to the internally-shunted Hall plate. The result is shown in Fig. 5-1(B); by choosing the shunt radius to be unity in the t plane and making the appropriate cuts (R2-R4), the shunt is mapped to a rectangle in the z plane. Since the contacts lay outside of the unity radius in the t-plane, they are warped into arc sections below the y = 0 line in the complex z-plane. The device in Fig.

5-1(B) is electrically equivalent to the device in Fig. 5-1(A), except for the small error introduced by the cuts R2, R3, and R4.

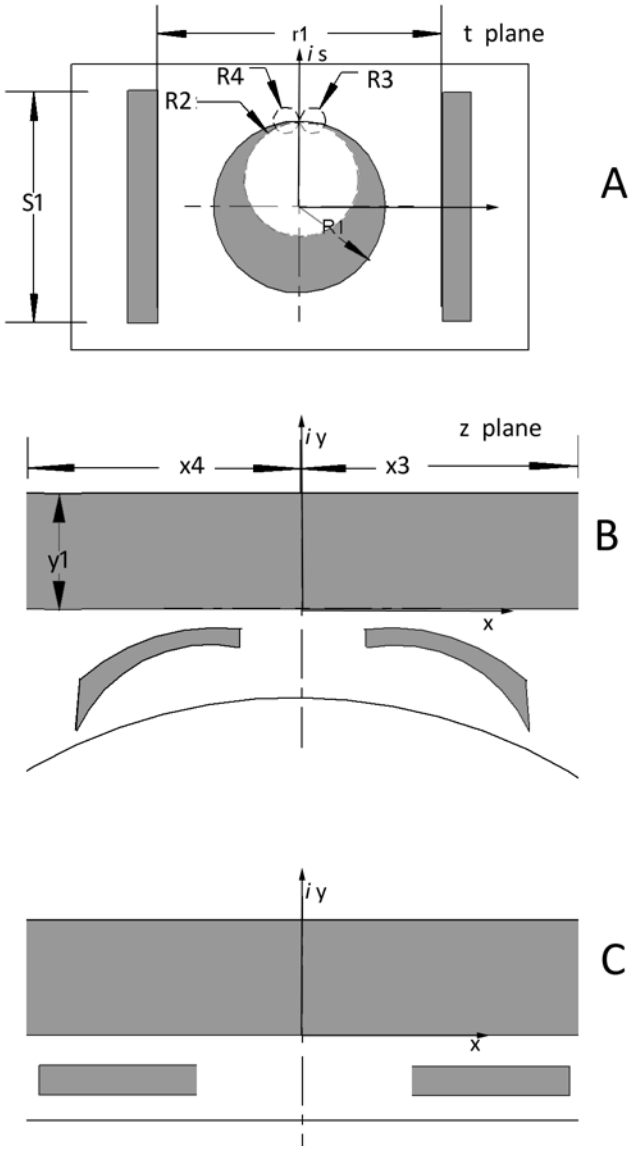

Fig. 5-1 The development of a simplified externally-shunted Hall plate. (A) a Hall plate with a circular metallic shunt embedded between the electrode, (B) actual bilinear transform of (A) with R1 = unity in the t-plane. R2, R3, and R4 define the +y, +x, and –x bounds respectively. (C) The simplification of (B) to a rectangular structure. Grey areas represent metallic regions and white areas represent semiconductor regions.

The device in Fig. 5-1(C) is a simplification of Fig. 5-1(B). Though no longer electrically equivalent to the internally shunted Hall plate, it is electrically similar and simpler. This

method, apart from the post-mapping simplification, is similar to the process for developing the externally-shunted vdP disk in [25]. In particular, the application of the bilinear transform to an internally-shunted device to render an externally-shunted device is the same.

5.2 Shunted Corbino Plate

The shunted Corbino plate (SCP), as it is called here, originates from the shunted Corbino sensor described in in [18]. The shunted Corbino plate operates on the EMR principle whereby at low fields the shunt acts as a short circuit to injected current which reduces the zero-field resistance of the structure. At high fields, the electric field is orthogonal to the shunt-semiconductor interface and the Lorentz force at the boundary expels current from the shunt and deflects it through the shunt gaps. This behavior produces an increase in resistance with applied transverse magnetic fields. The SCP retains the MR behavior of its parent disk, and its simpler rectangular structure is an advantage for analytical solutions, modeling, and fabrication. The process for generating the SCP includes generating a suitable off-center SCD then applying the bilinear conformal mapping. This process will be described in the following section.

The first step in generating a suitable SCD basis for the bilinear transform is to convert any concentric circular features to off-center circular features. As discussed in Chapter 3 and in [20], this step must be performed in the t-plane to produce a finite *and* rectangular device in the z-plane under the bilinear transform. Concentric features can be retained in the t-plane though appropriate cuts, but are then transformed into non-rectangular features in the z-plane. Introducing non-rectangular features into the z-

plane defeats the main purpose of the conformal mapping, which is to produce a *simpler* and electrically equivalent geometry. By shifting circular features of a given SCD off center, a new device is created which retains several properties of the concentric device as illustrated in Fig. 5-2. These properties include inner electrode diameter, outer electrode diameter, inner shunt radius, outer shunt radius, and shunt fill factor. The circular features of the SCD are shifted off center according to their radii and (3.4).

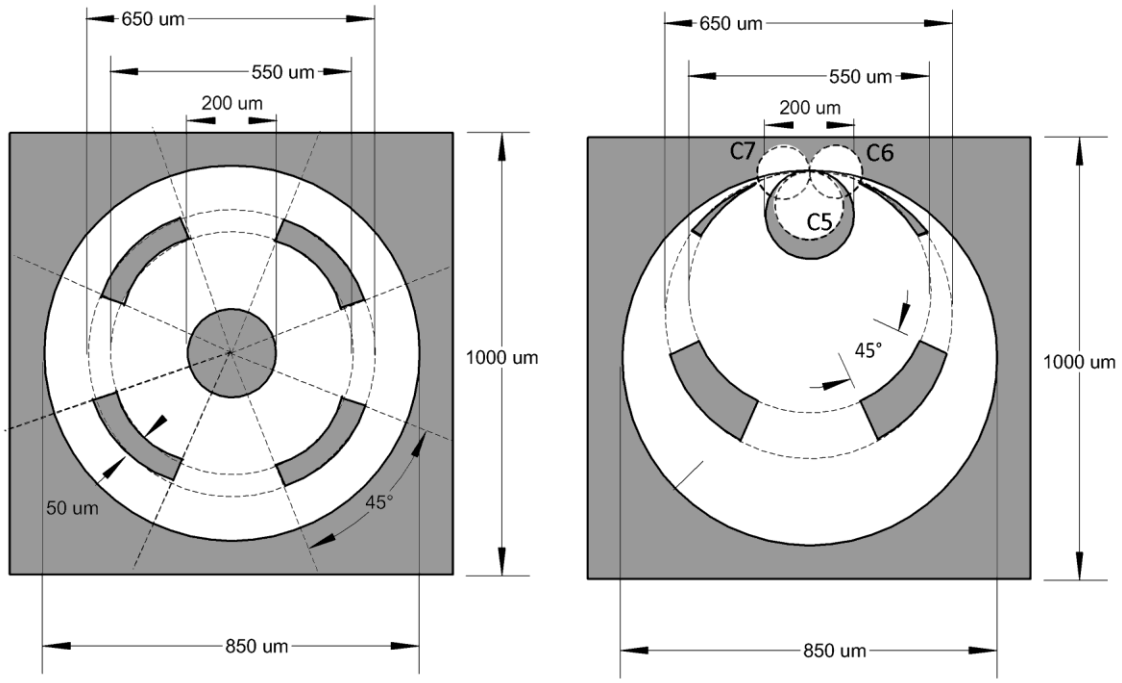

Fig. 5-2 Shunted Corbino disk sensor (A) and off-center shunted Corbino disk sensor (B). Dashed lines (C5, C6, C7) (B) indicate finite cuts that must be made prior to conformal mapping. Grey area represents metallic region, the white area represents the semiconductor.

Next, the off-center SCB must be abbreviated with circular cuts as previously described in section 3.1.2. The off-center SCD now becomes the parent t-plane device to which the bilinear transform can be applied. The bilinear transform of (3.1) maps each circular element in the off-center SCD in the t-plane to a line in the z plane. The z-

plane device corresponding to a SCD in the t plane is now called a shunted Corbino plate. Each circle (*C1-5*) in Fig. 5-3 (A) that is centered at (0, y_i / (y_i+1)), maps to the horizontal line y_i in Fig. 5-3 (B). The circles (*C6* and *C7*) centered at (1/x_2, 1) map to the vertical lines *x6* and *x7*, respectively.

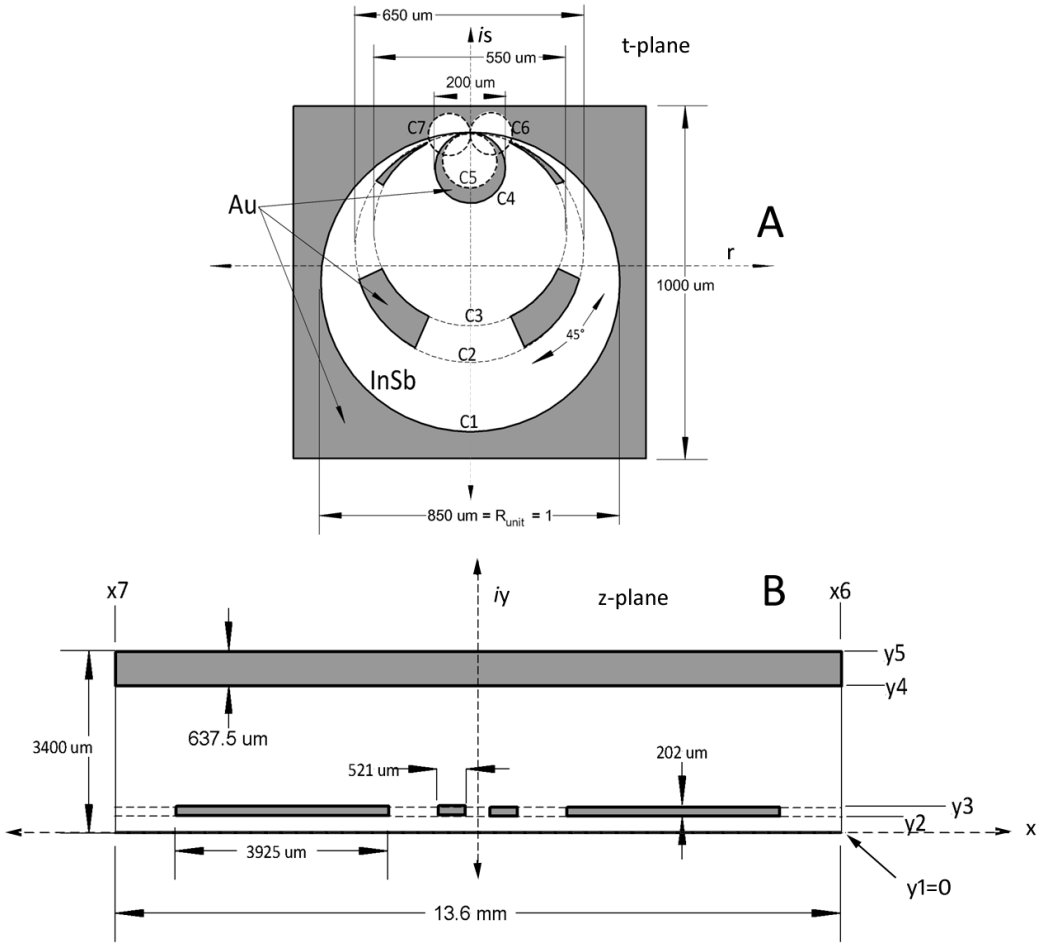

Fig. 5-3 (A) Off-center SCD in the t-plane and (B) the conformally mapped plate in the z-plane. Each circle in the t-plane (C_i) corresponds to either a horizontal line (y_i) or a vertical line (x_i) in the z-plane. The dashed circles (C5-C7) represent cuts made to the t-plane device to keep the device finite in the z-plane. Dimensions are labeled here for scale example.

5.3 The Effect of Geometry on Device Magnetoresistance

MR, dR/dB, and B^{-1} dR/dB are critical figures of merit in assessing the performance of MR and EMR sensor devices [2, 21]. The magnetoresistive behavior is also the starting point for the assessment of an EMR device designed for a power application. Other characteristics fundamental for power devices such as transition time, breakdown voltage, and critical current density become extraneous if the MR behavior does not suit a given application. In this section, geometric ratios characteristic to each topology (SCP and ESHP) are identified and their effect on magnetoresistive behavior is examined using the PSPICE FEM model.

5.3.1 Shunted Corbino Plate

For an arbitrary scale SCP, the most critical geometric parameter to MR is the shunt fill ratio in the y-direction, or γ. Here, this is defined as

$$\gamma \equiv \frac{\Delta y_1}{b} \tag{5.1}$$

where b is the distance between the electrodes in the y direction and $\Delta y1$ is the y-direction thickness of the embedded shunt as labeled in Fig. 5-4. When γ = 0/16, the SCP becomes a traditional (un-shunted) Hall plate. When γ = 16/16, the SCP does not become completely metallic due to the x-direction gaps in the shunt. These semiconductor gaps represent parallel conducting channels that do not compete with the metallic-shunt channels for current density ($\sigma_o << \sigma_{om}$). Other geometric factors (*e.g.* Δx1 and Δx2) and material properties will effect device MR, but are held constant as

listed in Table 5-1 to isolate the effect of the γ ratio. Material properties effect on resistance and MR will be considered in section 5.4.

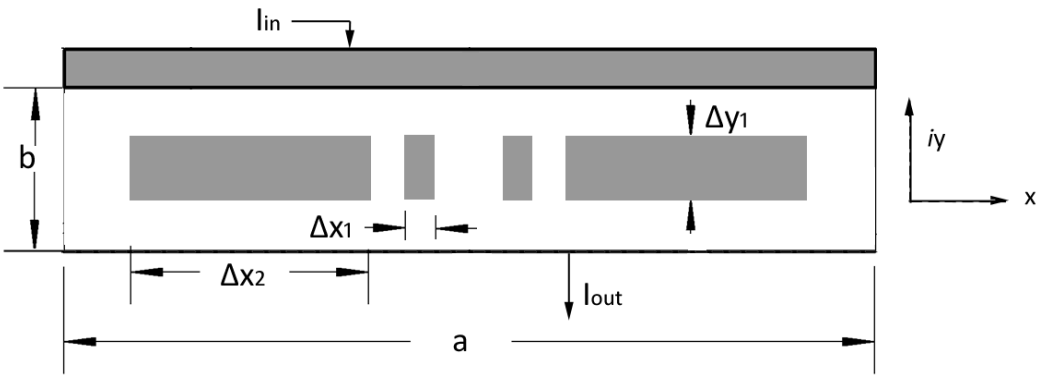

Fig. 5-4 Diagram of SCP with γ = 8/16, where γ ≡ Δy1/b. Grey represent metallic regions and white represents semiconductor. The values of Δx1 and Δx2 are fixed for this series of FEM calculations.

Using the FEM model with material properties held constant, the magnetic field was swept from -5 T to 5 T for SCPs with selected values of *γ.* The results are shown in Fig. 5-5 for values of 16*γ* = 0, 4, 6, 8, 12, and 14. The calculated resistance is symmetric about *B*=0 as expected since the SCP is symmetric about its centerline at *x* = 0. At all fields, the resistance of the device falls with increasing *γ*, but the magnitude of d*R*/d*γ* is at its peak for high fields (±5 T). The magnitude of dR/dB is highest at low fields (<1 T) for all values of *γ.* d*R*/d*B* begins to decay at fields > 2 T for all values of *γ*, but this is more pronounced for low *γ* ratios. This result is likely due to the accumulation of charge at the $\pm$ *x* bounds of the device, away from the internal shunt. This accumulation generates a Hall voltage that begins to balance the Lorentz force experienced by charge carriers. For high values of *γ*, there is less semiconductor volume located away from the internal shunt, which minimizes amount of accumulated charge. In effect, for large

values of *γ,* the internal shunt shorts the Hall voltage that would otherwise be generated at high fields, as in a traditional Hall plate.

TABLE 5-1 PSPICE FEM MODEL PARAMETERS AND TYPICAL VALUES FOR THE SCP

Model parameter symbol	Description	Value	Units
B	transverse magnetic field magnitude	0	T
t	thickness (z)	1.0	mm
a	width (x)	13.6	mm
b	length (y)	3.4	mm
μ	semiconductor mobility	5.0	m^2/Vs
n	semiconductor carrier density	2.0×10^{21}	m^{-3}
Ny	number of semiconductor cells in the y direction	20	-
Nx	number of semiconductor cells in the x direction	80	-
Δy1	shunt length (y)	variable	μm
γ	shunt Fill ratio in y direction (Δy1/b)	$\Delta y1/b$	
μ_m	Au mobility	5.3×10^{-3}	m^2/Vs
n_m	Au carrier density	5.90×10^{28}	m^{-3}
Δx1	inner shunt width		
Δx2	outer shunt width		
σ_o	semiconductor conductivity	1.6×10^{3}	$S\ m^{-1}$
σ_{om}	Au conductivity	5.0×10^{7}	$S\ m^{-1}$

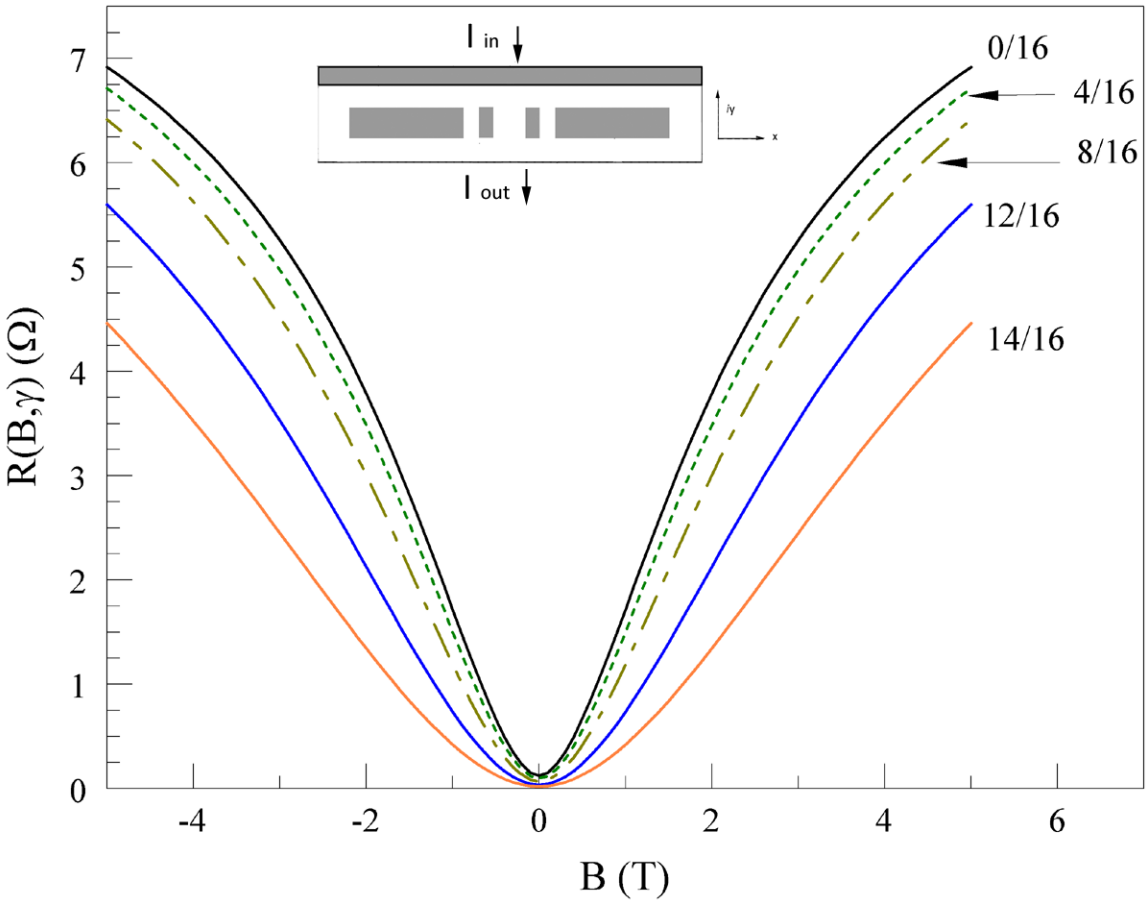

Fig. 5-5 High-field resistance of the SCP as a function of magnetic field. Traces shown are for γ values of 0, 4/16, 8/16, 12/16, and 14/16 as labeled.

Another way to represent this data is shown in Fig. 5-6 where the MR is shown for each *γ* value for magnetic fields between ±5 T. All MR behavior is quadratic at low magnetic field (< 0.1 T), but d(MR)/d*B* quickly saturates for low *γ* values due to the charge accumulation previously mentioned. The large values of MR for *γ* values of 14/16 and 12/16 at high magnetic fields are the result of the internal shorting of the Hall voltage, as well as the lowering of the zero-field device resistance by the large internal

shunt.

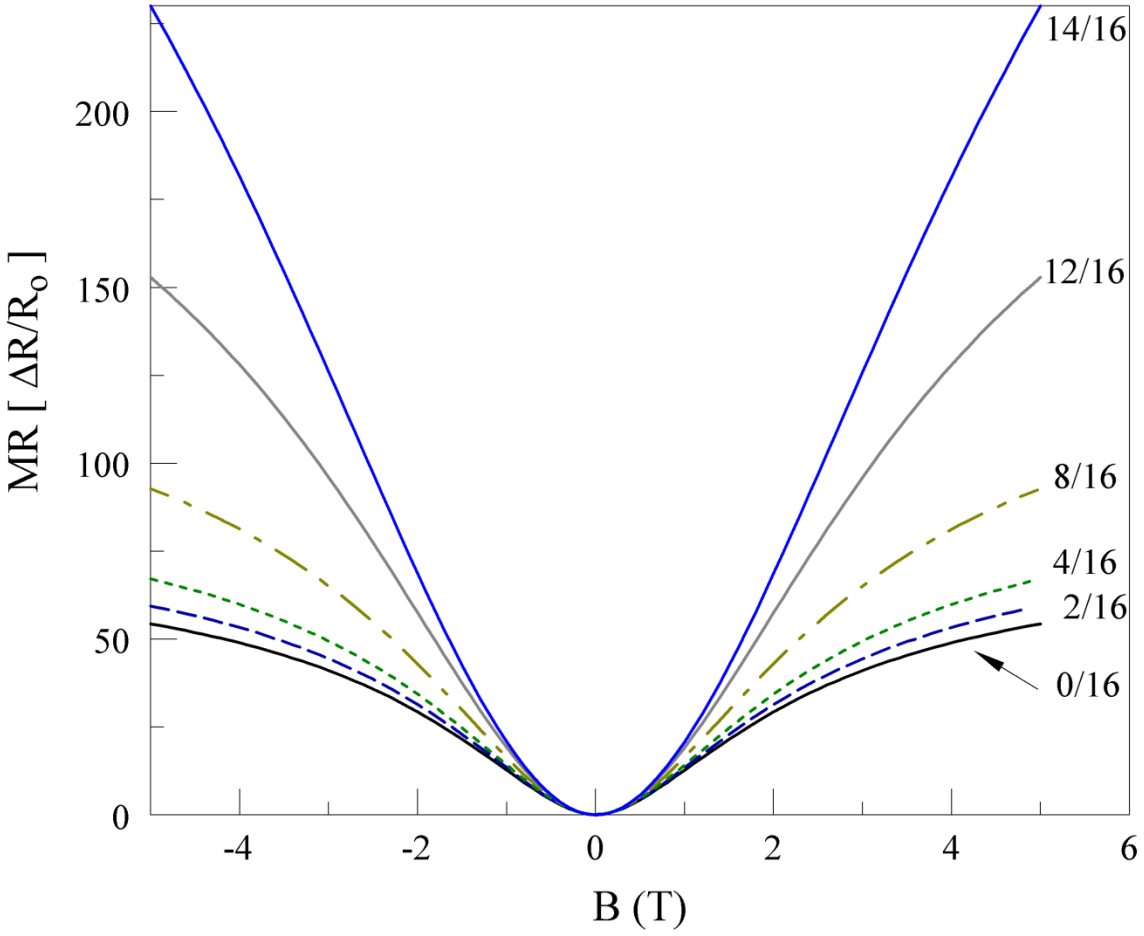

Fig. 5-6 MR of SCP as a function of magnetic field from -5 to 5 T. Traces shown are for γ values of 0/16, 4/16, 8/16, 12/16, and 14/16 as labeled.

5.3.2 Externally-Shunted Hall Plate

The ESHP is similar in form to the externally-shunted vdP plate. The physical principal of operation is the same, but the ESHP is designed for the 2-point resistance operation as opposed to the vdP plate's 4-point resistance. This difference is manifested in the wide current injection contacts at the base of the plate as in Fig. 5-7. Important geometric factors for the ESHP include semiconductor L/W ratio, contact length and

separation and the ratio of shunt length to semiconductor length (L_m/L_s). A ratio that involves the semiconductor L/W ratio and the ratio of semiconductor length to shunt length will be introduced by fixing the device width (W) and defining

$$\tau \equiv \frac{b_1}{b_2 + b_1} \tag{5.2}$$

where b_1 is the metallic shunt length and b_2 is the semiconductor length as diagramed in Fig. 5-7.

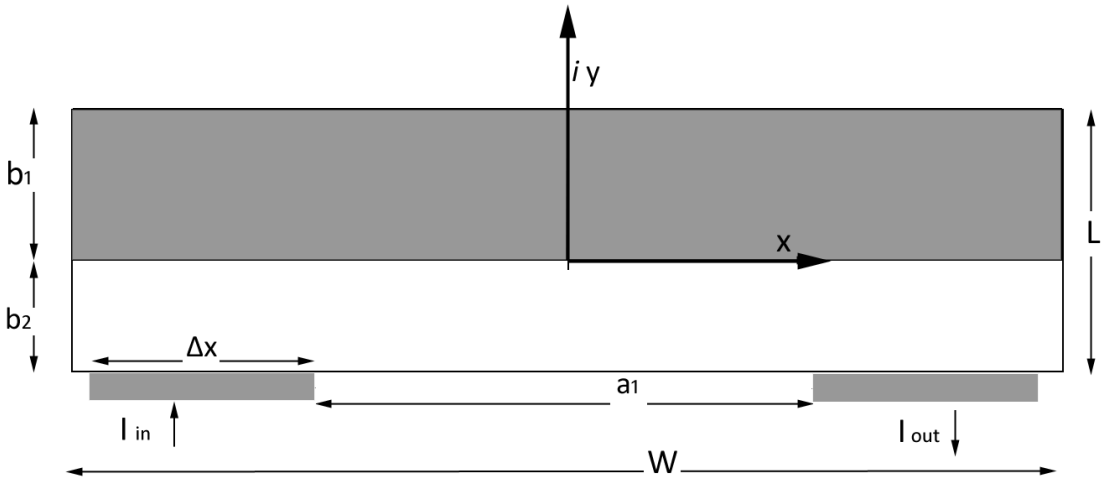

Fig. 5-7 Externally-shunted Hall plate with τ = 12/20. Grey areas represent metallic regions and white areas represent semiconductor regions. $\tau \equiv b_1/(b_1+b_2)$

Using the PSPICE FEM model, the ESHP resistance was calculated as a function of applied magnetic field between ±5 T. Material properties were held constant as listed in Table 5-2. The result is shown in FIG. 5-8 for device resistance and in Fig. 5-9 for MR, both plots include traces for shunt ratios corresponding to 20τ = 0, 4, 8, 12, 16, and 18. The zero-field resistance decreases with increasing τ. This result is due primarily to the decreasing path length through the semiconductor at zero field. The MR of the two homogenous cases (τ = 0 and τ = 1) is due to conventional current deflection described

by the Hall angle. In the $\tau = 0$ case, the device becomes a homogenous semiconductor slab and an applied magnetic field causes in increase in path length through the high-mobility ($\mu = 5\ m^2/Vs$) semiconductor, and thus an increase in resistance. For the case of $\tau = 1$, the device becomes a metallic slab where all semiconductor resistance vanishes, leaving the conductive, low-mobility ($\sim 10^{-3}$) metal to vary in resistance only a few $\mu\Omega$ over the entire range. The resistance curve for the $\tau = 1$ case is off low scale in FIG. 5-8, but its sensitivity (dR/dB) can be seen in Fig. 5-10.

TABLE 5-2 PSPICE FEM MODEL PARAMETERS AND TYPICAL VALUES FOR ESHP

Model parameter symbol	Description	Value	Units
B	Transverse magnetic field magnitude	0	T
t	thickness (z)	1.0	mm
W	Width (x)	13.6	mm
L	Length (y)	3.4	mm
μ	Semiconductor mobility	5.0	m^2/Vs
n	Semiconductor carrier density	2.0×10^{21}	m^{-3}
Ny	Number of cells in the y direction	20	-
Nx	Number of cells in the x direction	80	-
b1	Shunt length (y)	variable	mm
b2	Semiconductor region length	variable	mm
τ	Shunt Fill ratio	b1/(b1+b2)	-
μ_m	Au shunt mobility	5.3×10^{-3}	m^2/Vs
n_m	Au shunt carrier density	5.90×10^{28}	m^{-3}
Δx	Contact width (x)	3.57	mm
a1	contact separation (x)	5.78	mm
σ_o	Semiconductor conductivity	1.6×10^{3}	$S\ m^{-1}$
σ_{om}	Au conductivity	5.0×10^{7}	$S\ m^{-1}$

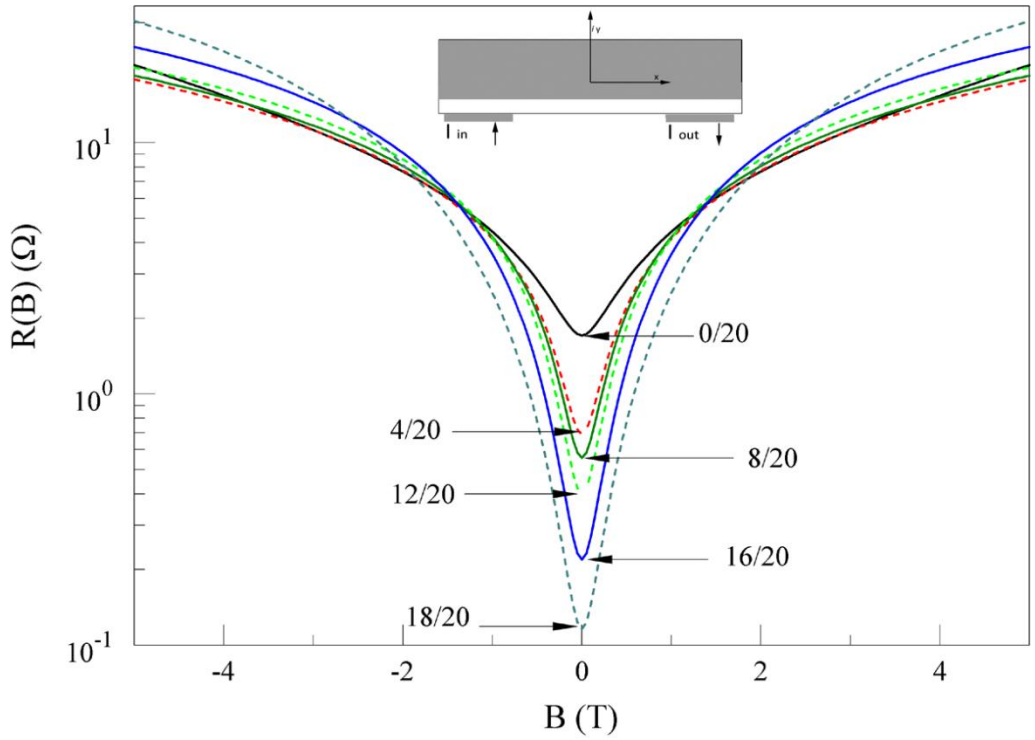

Fig. 5-8 Variation in resistance as a function of applied magnetic field for the ESHP with selected values of τ. Traces shown are for values of 20τ = 0, 4, 8, 12, 16, 20.

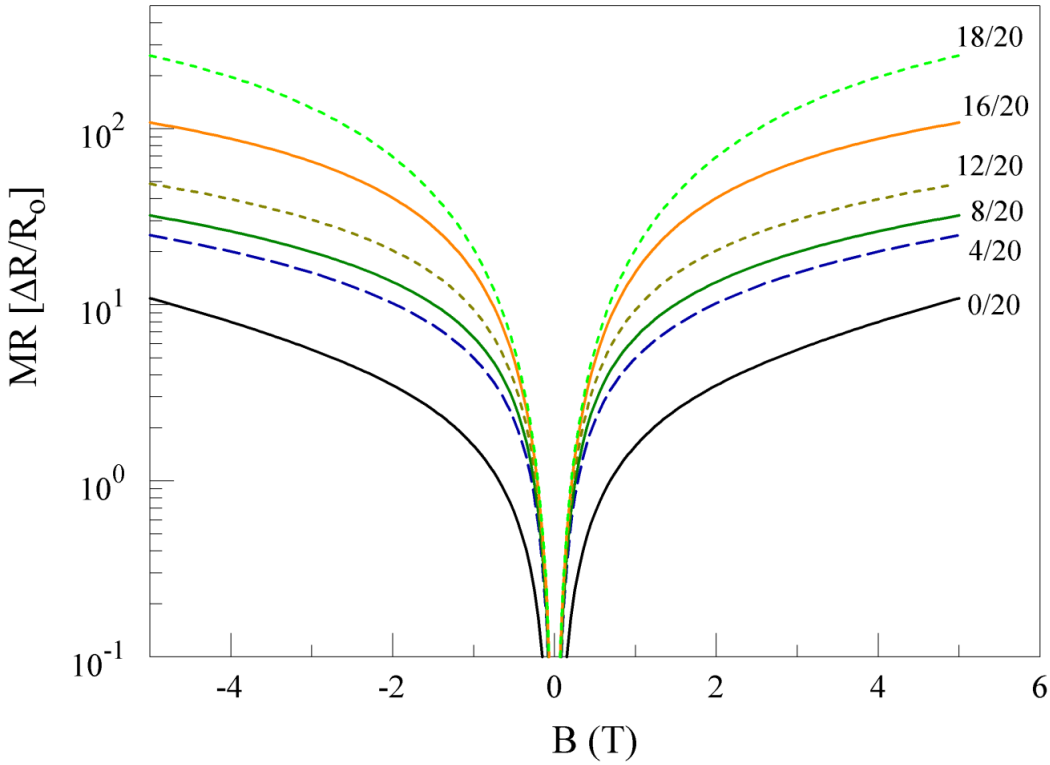

Fig. 5-9 Magnetoresisatance of ESHP as a function of applied magnetic field. Traces shown are for τ values between 0/20 and 18/20 as labeled on the plot.

The traces of more interest are of the hybrids for which $0< \tau <1$. These cases generally have a low resistance at zero field due to the current density in the shunt being at its maximum and the current density through the semiconductor being at its minimum with respect magnetic field. As indicated by Fig. 5-10, the curvature (d^2R/dB^2) for $4 \leq 20\tau \leq 18$ is very large for fields less than 1T. This is partially due to the current deflection effect in the semiconductor, but also because the current is beginning to be deflected away from the shunt because of the boundary conditions of the electric field at the interface and the increasing Hall angle.

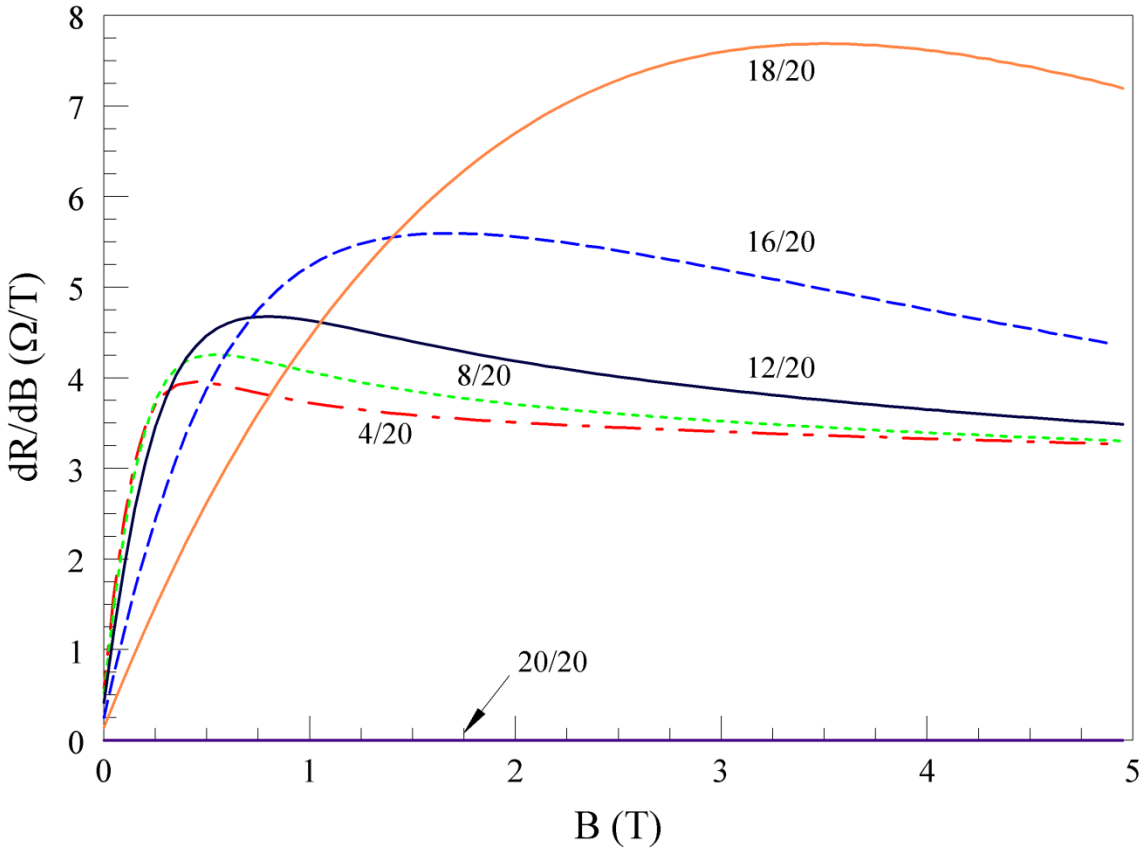

Fig. 5-10 Sensitivity (dR/dB) of the ESHP as a function of magnetic field for selected values of τ. Traces shown are for 20 τ= 4, 8, 12, 16, 18, and 20 as labeled on the plot.

The other interesting feature displayed in Fig. 5-10 is the point at which the sensitivity reaches its peak. For the smaller values of τ (4/20 and 8/20), the peak occurs at relatively low magnetic fields (<500mT). As the value of τ increases, the peak sensitivity shifts to higher values of B. These peaks occur at 800 mT, 1.65 T, and 3.5 T for 20τ values of 12, 16, and 18 respectively.

5.4 Effect of Semiconductor Properties on Magnetoresistance

It has been shown in Chapter 4 and concluded in [24] that MR is not sensitive to the conductivity of the metallic shunt so long as it is approximately two orders of magnitude more conductive ($\sigma_m >> \sigma_s$) than the semiconductor. The second requirement of the shunt material for EMR behavior is that the contact resistance be insignificant compared to the device resistance. This was shown in [26]. With these results in mind, the semiconductor material properties become of prime interest for prospective power applications. Semiconductor mobility is critical for its impact on device sensitivity to applied magnetic field (dR/dB). Semiconductor carrier density a critical factor in total device resistance at all fields. The effect of these two properties on device resistance and MR will be presented in this section.

5.4.1 Semiconductor Carrier Mobility

The mobility of a semiconductor is the principle factor in its usefulness in any device in which the geometric MR dominates [13]. This is why narrow band gap semiconductors with large room-temperature mobilities such as InSb, InAs, and HgCdTe are used, almost exclusively, in room-temperature Hall-effect sensors, EMR sensors, and

power Hall-effect devices [1, 12, 14]. For the semiconductor-metal hybrid devices under examination here it would seem that the semiconductor mobility must simply be maximized for optimum device sensitivity to magnetic field. While this assertion is essentially correct, other factors such as material cost, feasibility of fabrication, and desired range of magnetic-field operation make useful the characterization and comparison of the MR dependence on semiconductor mobility.

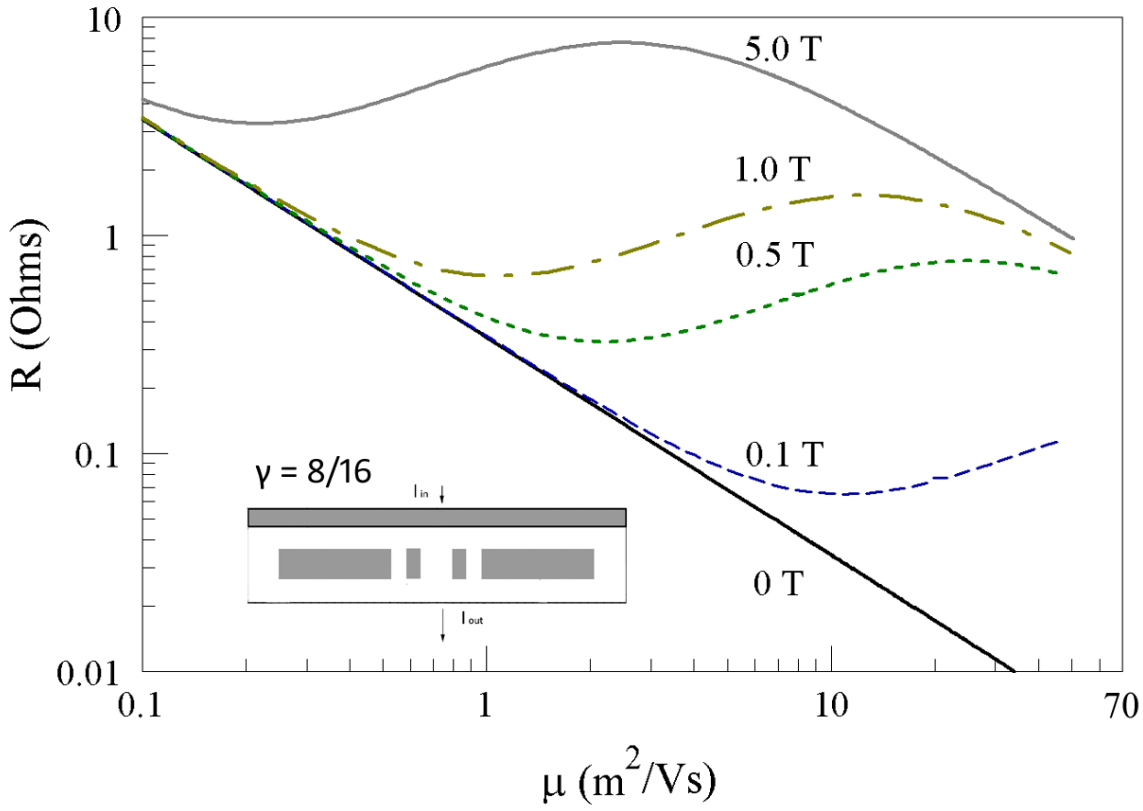

Fig. 5-11 Resistance as a function of semiconductor mobility for SCP with γ = 8/16 and material properties listed in Table 5-1. Traces shown here are for constant magnetic field values of 0 T, 0.1 T, 0.5 T, 1.0 T, and 5.0 T as indicated on the plot.

In order to isolate the effect of semiconductor mobility on device resistance and MR for the SCP device, geometry and other material parameters are held constant as the

semiconductor mobility is varied from 0.1 m^2/Vs to 50 m^2/Vs for selected values of constant applied magnetic field. The PSPICE FEM model calculations for the SCP with γ =8/16 are shown in Fig. 5-11 for magnetic field values of 0, 0.1, 0.5, 1.0, and 5.0 T. The γ value of 8/16 was chosen because it is representative of the entire set of geometric ratios for the purpose of the material properties investigation.

The zero-field resistance of the SCP decreases linearly with increasing μ since the diagonal elements of the conductivity matrix (3.19) dominate at zero field. At low mobility values ($\mu < 1\ m^2/Vs$) the device sensitivity (dR/dB) is extremely low for values of ($\mu B < 1$), but increases significantly at high fields in the $\mu B > 1$ range. At large mobility values, dR/dB is at a maximum for low inductions (B~100 mT) and begins to saturate for B > 1T. This can be qualitatively explained by the large Hall angle for $\mu >> 1$ coupled with the electric-field boundary conditions at the shunt-semiconductor interface. These two pieces combine to allow the magnetic field to easily (i.e. at a low field) deflect current from the internal shunt. A critical magnetic field value is reached at which effectively all of the current travels through the shunt gaps. At magnetic fields higher than this critical field, no significant increase in resistance can be realized. This associated saturating behavior depends on semiconductor mobility, magnetic field, and device geometry.

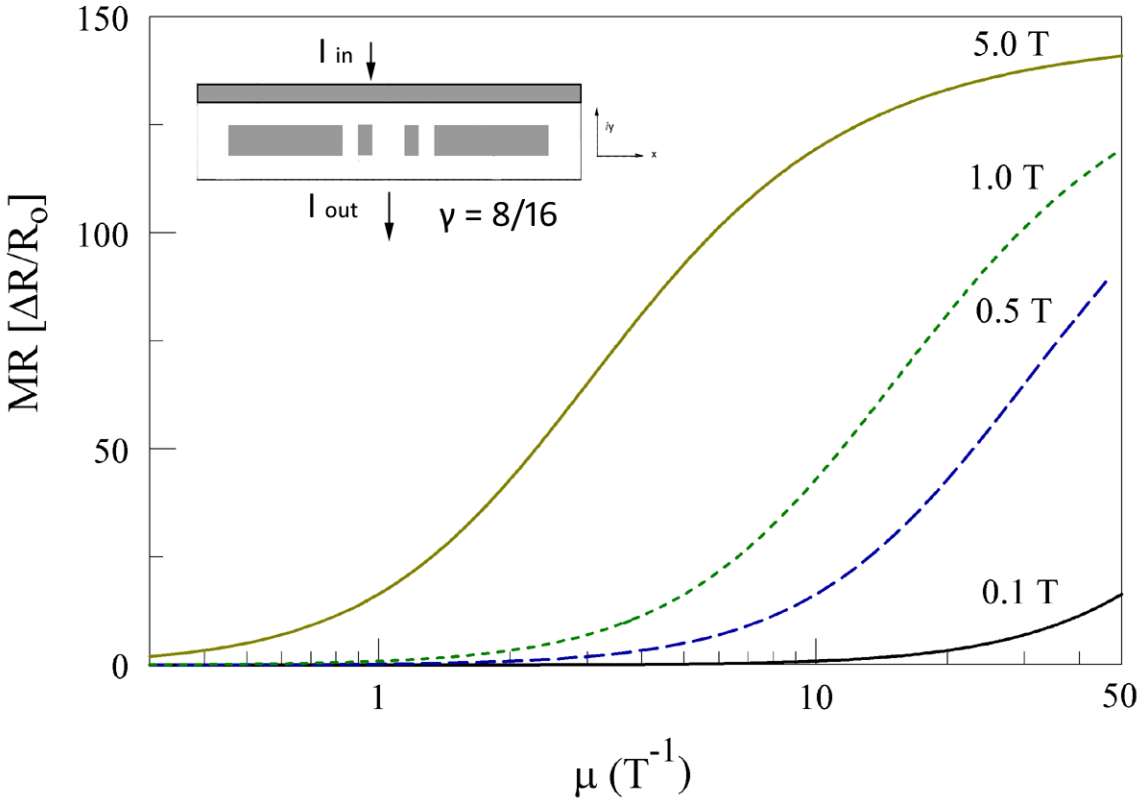

Fig. 5-12 MR as a function of semiconductor mobility for SCP with γ = 8/16 and material properties listed in Table 5-1. Traces shown here are for constant magnetic field values of 0 T, 0.1 T, 0.5 T, 1.0 T, and 5.0 T as indicated on the plot.

This behavior is also evident, thought to a lesser degree in Fig. 5-12, where the SCP MR increases at higher μ primarily due to a decrease in zero-field resistance. Just as diminishing returns are realized for higher fields at high μ, there are diminishing returns for increasing μ at all non-zero field values. The peak resistance for a given field occurs at low mobility for high fields and shifts to higher mobility values for low fields. This is because the MR behavior is controlled by the off-diagonal elements of the magnetoconductivity matrix which are quadratic functions of the product μB.

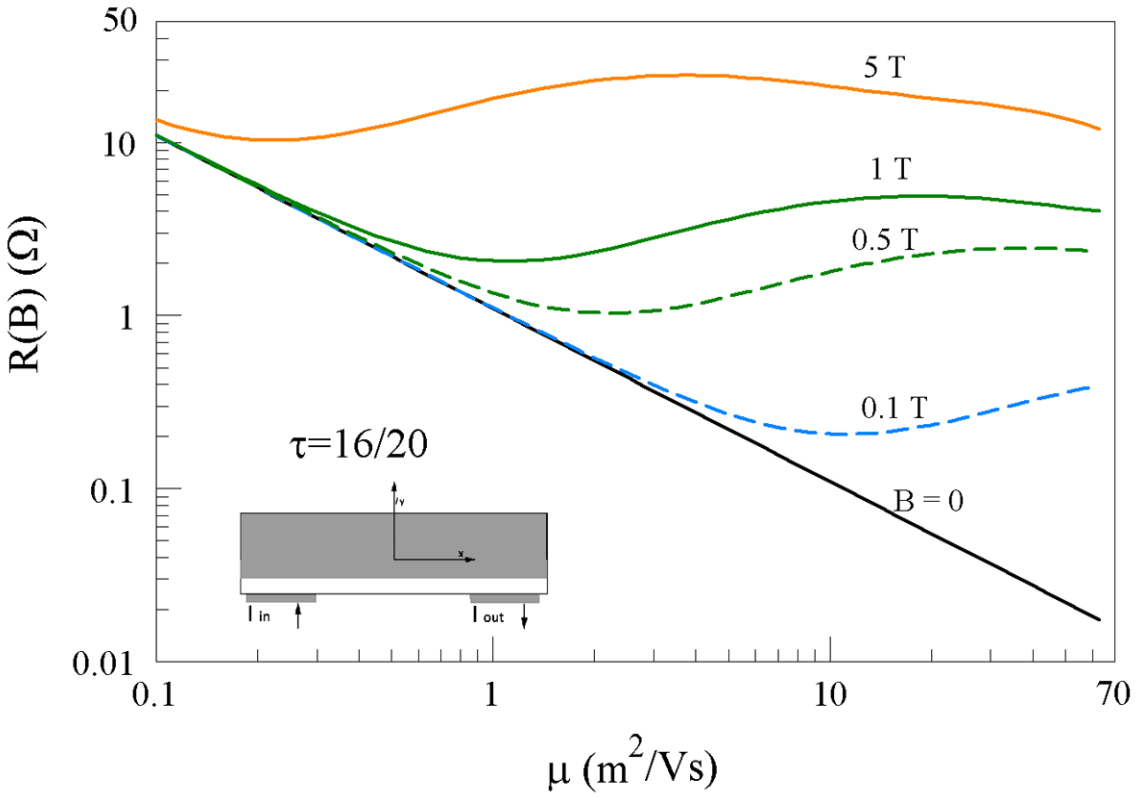

Fig. 5-13 Resistance as a function of semiconductor mobility for ESHP with τ =16/20. Traces shown are for applied magnetic fields of 0, 0.1, 0.5, 1.0, 5.0 T as labeled on the plot.

Just as with the SCP, a typical geometry from the ESHP family was selected for this investigation of material properties. Using the FEM model, the semiconductor mobility was varied between 0.1 and 50 m2/Vs for the ESHP (τ = 16/20) in order to examine the effect on device resistance and MR. Fig. 5-13 shows the device resistance andFig. 5-14 shows the MR for magnetic field values between 0 and 5 T as a function of μ. The resistance peaks for constant inductions as in the SCP case but are less pronounced here.

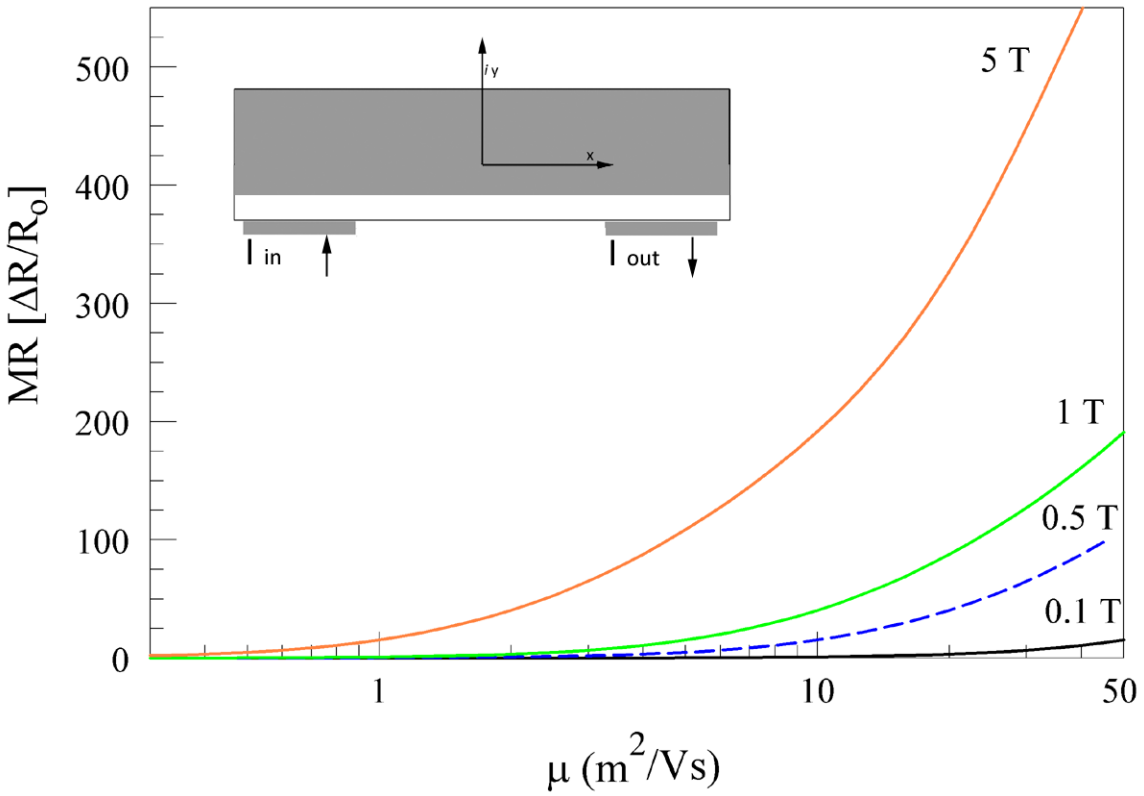

Fig. 5-14 MR as a function of semiconductor mobility for ESHP with τ =16/20. Traces shown are for applied magnetic fields of 0, 0.1, 0.5, 1.0, 5.0 T as labeled on the plot.

The peaks for low fields (B <200 mT) are off scale high for the mobility range shown here. One interesting feature in Fig. 5-14 is that the slope of the MR does not begin to level out in this mobility range for any applied field magnitudes. This difference compared with the SCP is because the ESHP requires a larger value of μB to begin displaying saturating behavior, i.e. a larger value of μB is needed to deflect all current from the shunt.

5.4.2 Semiconductor Carrier Density

Semiconductors typically used in EMR devices are doped n-type for two reasons. First, they are *doped* to be majority carrier devices since the alternative (minority) has a carrier density, and thus conductivity, which is exponentially dependent upon temperature. In effect, it reduces dR/dT for operation near room temperature. For the semiconductors traditionally used in EMR devices, this is possible because mobility does not decrease drastically with increasing doping [5]. Second, they are doped *n-type* because the mobility of electrons is much larger than that of holes ($\mu_n >> \mu_p$). This results in an n-type device with a much higher sensitivity (dR/dB) than an otherwise similar p-type device.

In order to examine the influence of carrier density within the constraints of being n-type and heavily doped, the same SCP and ESHP representative device geometries discussed in 6.5.1 were modeled using the PSPICE FEM model. The semiconductor carrier density was varied between 10^{19} m^{-3} and 10^{26} m^{-3} and the resistance was calculated for magnetic field magnitudes between 0 and 5 T. Other material properties were held constant at values listed in Table 5-1 and Table 5-2. The results are shown for the SCP device in Fig. 5-15 and for the ESHP device in Fig. 5-16.

In both devices, the resistance for all fields varies linearly with carrier concentration in the semiconductor until the critical carrier density is approached. The critical carrier density is the semiconductor density at which its conductivity equals that of the shunt ($\sigma_s = \sigma_m$). At this point, the device loses its hybrid composition and its EMR character. This behavior is typical for EMR devices as shown in Chapter 4 and in [24].

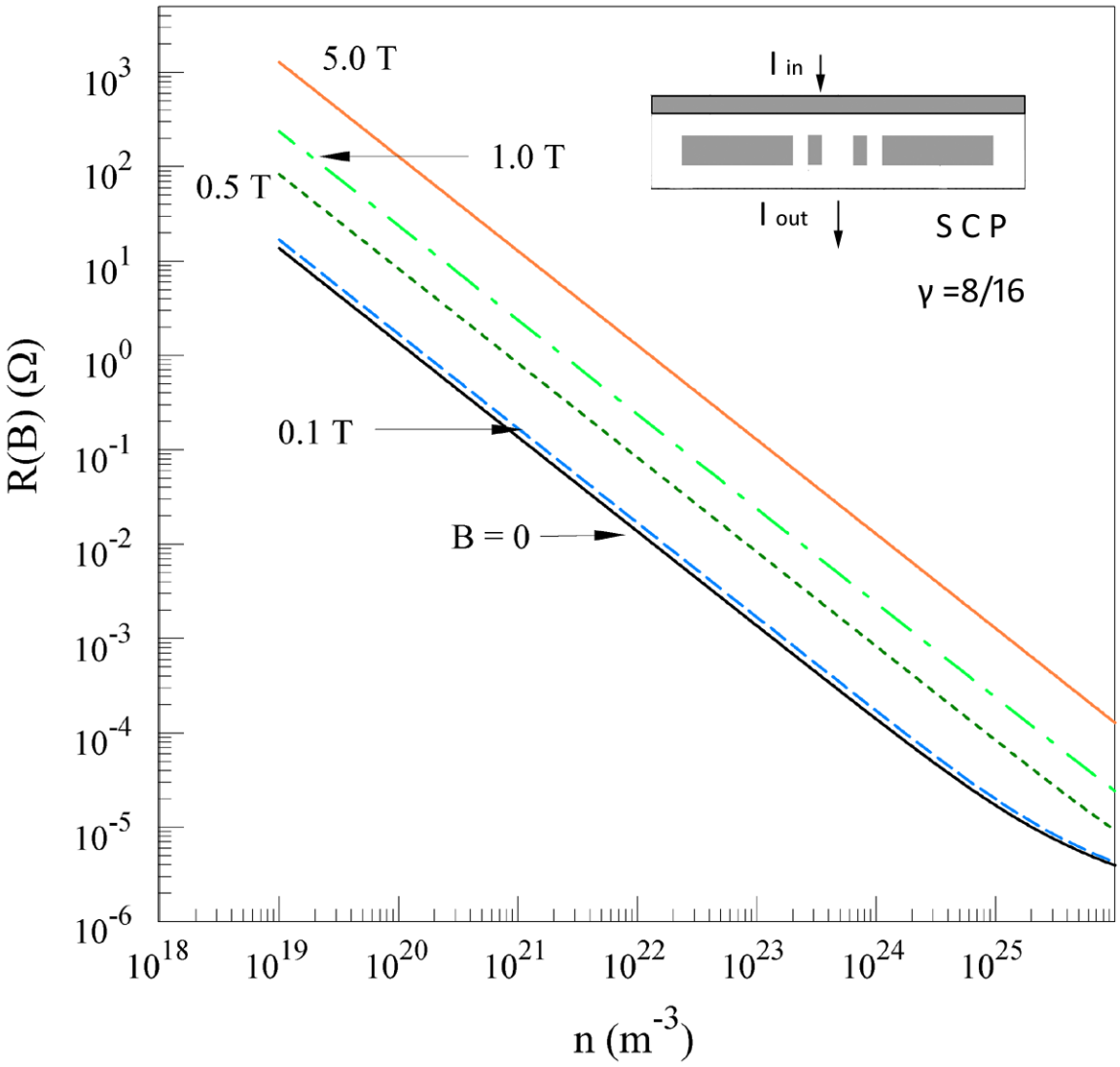

Fig. 5-15 Device resistance for the SCP with γ = 8/16 as a function of semiconductor carrier density for magnetic field values of 0 T, 0.1 T, 0.5 T, 1.0 T, and 5.0 T.

The most important feature of these results shown in Fig. 5-15 and Fig. 5-16 is the predictable variation in device resistance with doping, coupled with the invariance of MR and dR/dB with doping density. This result suggests a degree of adjustability in zero-field resistance for each topology, while retaining the same MR characteristics over a broad range of dopant densities.

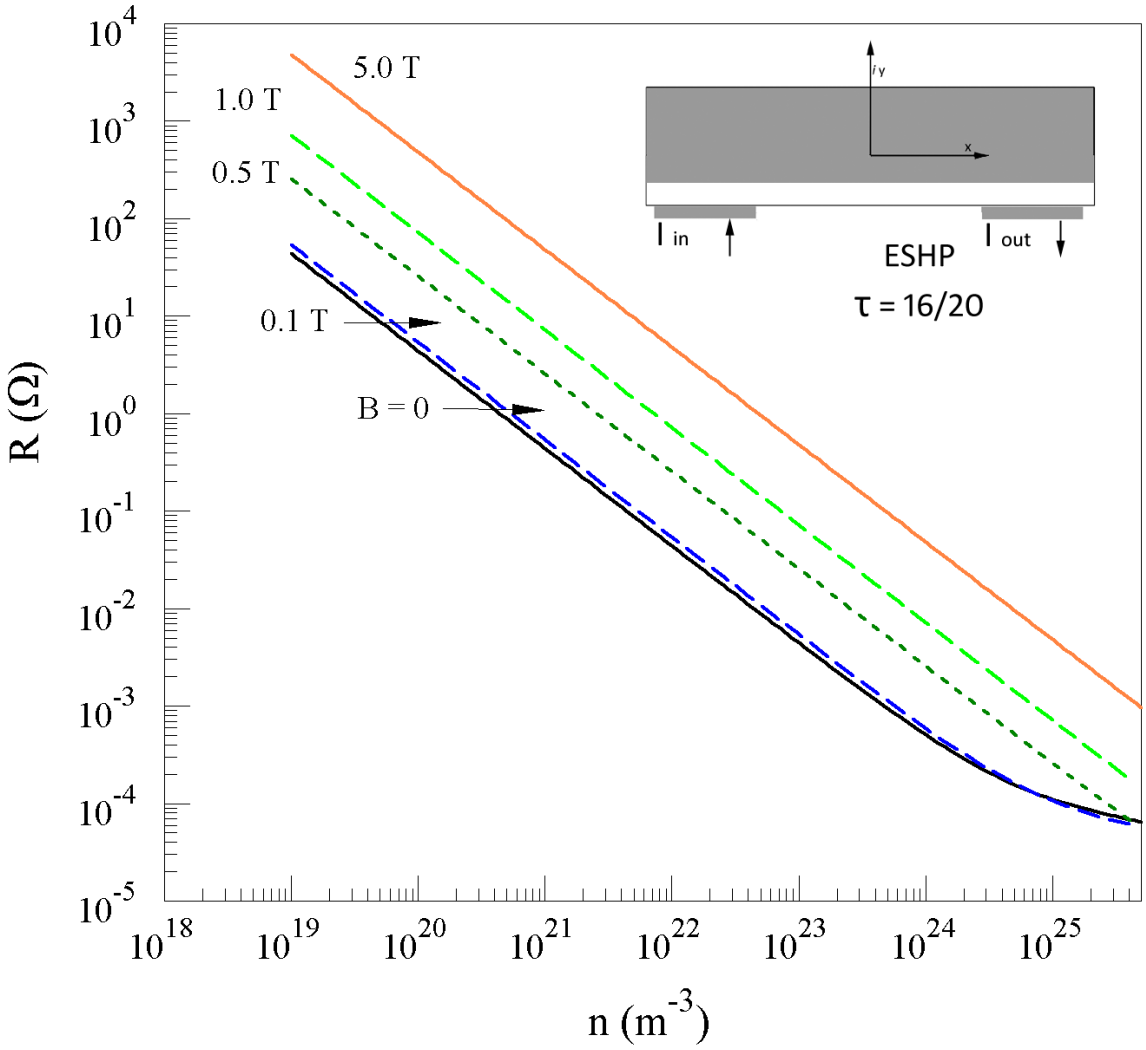

Fig. 5-16 Device resistance for the ESHP with τ = 16/20 as a function of semiconductor carrier density for magnetic field values of 0 T, 0.1 T, 0.5 T, 1.0 T, and 5.0 T.

5.5 Peak Pulsed Current Density

One characterization not emphasized for MR metal-semiconductor hybrid sensors is the peak device current density. EMR sensors are generally operated at very low bias currents which are necessary for constant-current operation in nano-scale devices [4]. This is however one limiting factor for MR for devices operating in pulsed-power applications.

Since these devices employ majority-carrier semiconductors with a positive temperature coefficient of resistivity, thermal runaway is not a potential failure mechanism [27]. However, the non-uniform distribution of current in EMR-based devices can result in large local current densities. These "hotspots" can result in local thermal damage, degraded performance, and eventually device failure.

The peak pulsed device current is limited by a number of factors. The first to be considered is the critical current density in the semiconductor. The semiconductor is the limiting factor since the highly conductive shunt material permits current densities orders of magnitude greater than the semiconductor critical current density, without degraded performance. Here we will define the semiconductor critical current density (J_c) as the current density which results in irreversible semiconductor damage due to joule heating for a given pulse duration. Here,

$$J_c = \sqrt{\frac{\rho_m C_m \Delta T_c \sigma}{\Delta t_p}} \tag{6.3}$$

where ρ_m is the mass density, σ is the conductivity, C_m is the specific heat capacity, and ΔT_c is the critical temperature increase, all for the semiconductor. Δt_p is the duration of the current pulse. The peak device current is then defined as the maximum current for which $J < J_c$ throughout the semiconductor region in the device.

A number of assumptions are then made in order to compare the devices' geometry factors effect on peak device current at zero magnetic field. The assumptions include temperature invariant density, specific heat capacity, and conductivity over the ΔT_c range. In addition, no external heat sinking is considered. In order to isolate the geometric factors' effects on zero-field pulsed current capacity, a model was generated in ElecNET for a range of geometry factors in each device family (SCP and ESHP) [28].

The maximum element size for the ElecNET mesh was set at 0.1 mm for all device elements as shown in Fig. 5-17for the SCP and in Fig. 5-18 for the ESHP.

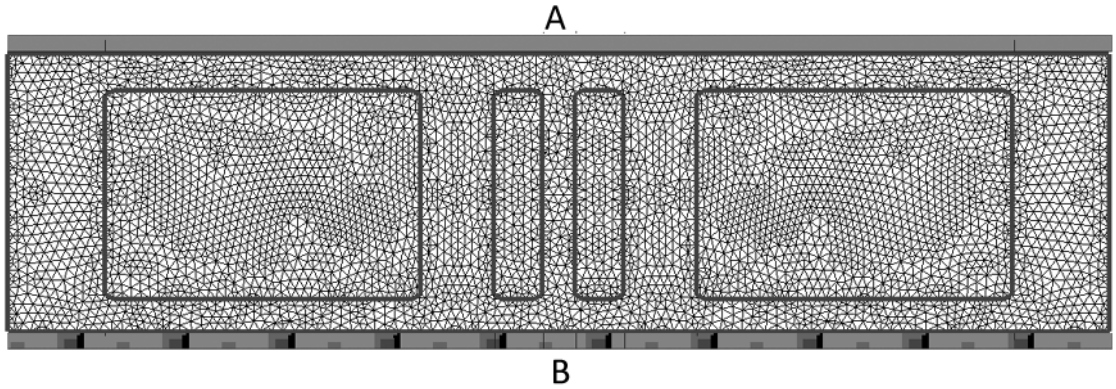

Fig. 5-17 ElecNET solution mesh generated for SCP model with γ = 12/16. Internal boxed region represents the shunt. (A) is the positive voltage contact, (B) is the ground contact in the model.

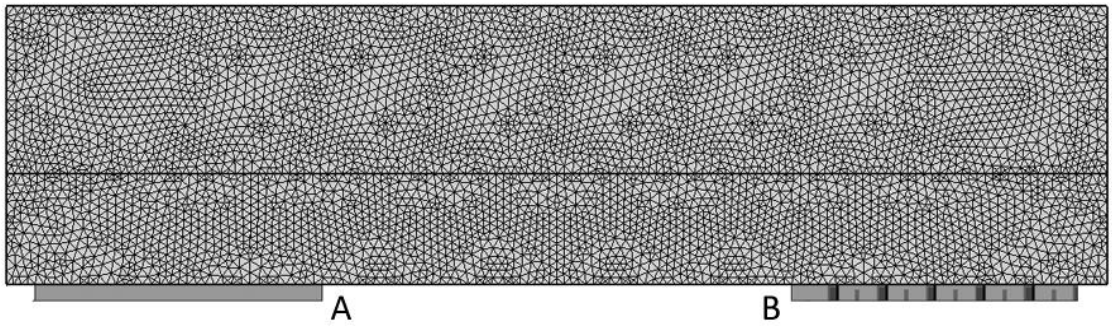

Fig. 5-18 ElecNET solution mesh generated for the τ = 16/20 ESHP device. The dark horizontal line is the metal-semiconductor interface. (A) is the positive voltage contact, (B) is the ground contact in the model.

Device dimensions and semiconductor material properties were set at the values listed in Table 5-1 and Table 5-2 respectively. Using a Newtonian iteration method, the voltage source was varied until the maximum semiconductor local current density fell below the value of J_c.

5.5.1 Peak Pulsed Current density in the Shunted Corbino Plate

Fig. 5-19 shows the calculated peak 1-ms pulsed current in the SCP family as a function of γ (6.1). A final-iteration voltage resolution of 0.2 V resulted in a peak pulsed

current uncertainties inversely proportional to each device's resistance. The γ uncertainty arises from the 50 μm resolution of the construction grid used in the ElecNET model and is constant for all values. These uncertainties are indicated in Fig. 5-19 with error bars.

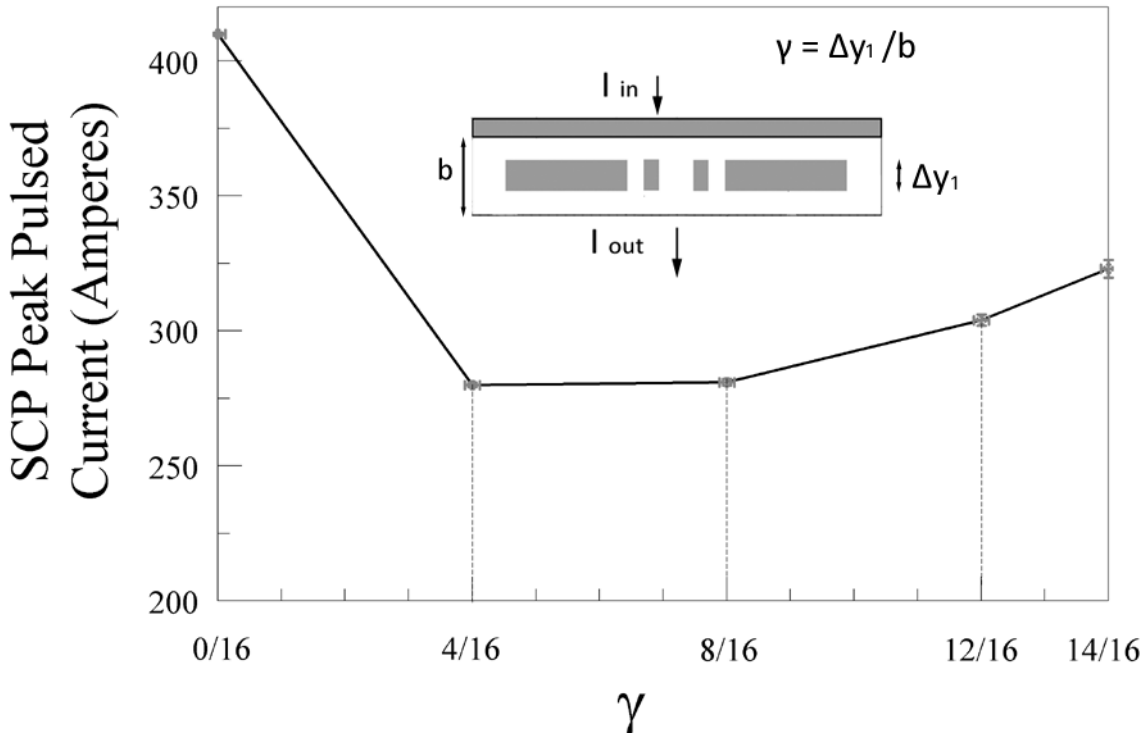

Fig. 5-19 Peak 1-ms Pulsed current for the SCP device family as a function of γ. Device dimensions and material properties are listed in Table 5-1.

The best way to interpret the results shown in Fig. 5-19 is with the help of Fig. 5-20. The maximum peak pulsed current is in the homogenous case of γ = 0/16. This is due to the uniform current density throughout the device as shown in Fig. 5-20 (A); there is no shunt to cause current hotspots. The absence of a shunt also means this is not a semiconductor-metal hybrid, in this examination it serves as a reference for the other devices. The introduction of a small shunt as in Fig. 5-20 (B) drastically redistributes the

device current and introduces the geometry feature that leads to the peak semiconductor current density. Each shunted device displays current crowding at the corners of the shunt segments. This is expected since the electric field gradient is highest at this point for each value of γ. As γ increases, the variance in local current densities increases. This is evident in Fig. 5-20 as the shunts reduce the current density in the lateral proximate semiconductor regions. As the shunt length increases (y-direction) the overall device resistance decreases and the peak pulsed-current capacity increases.

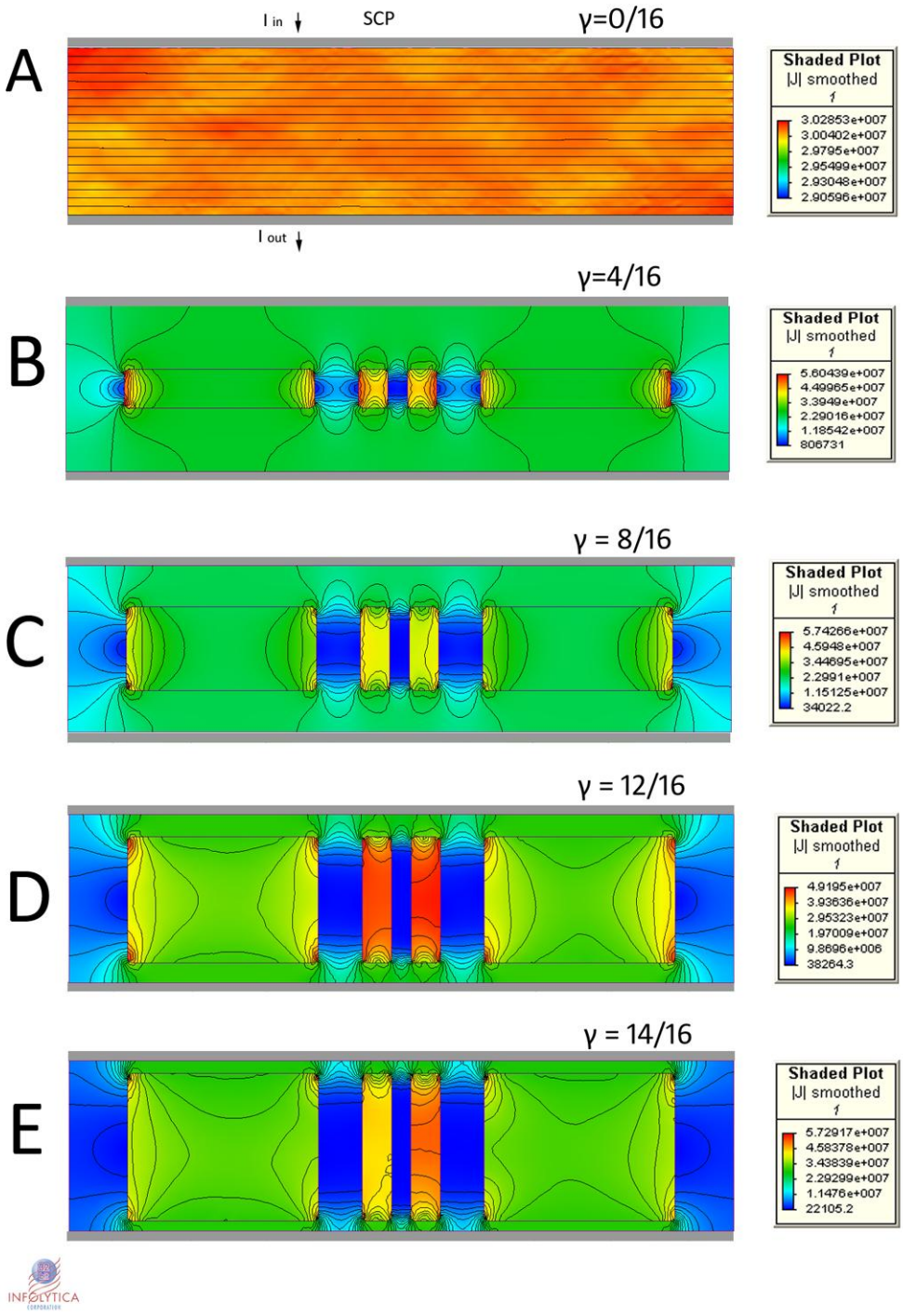

Fig. 5-20 Shaded plots of current density for the family of SCP devices when conducting at their respective peak pulsed current. Contour lines connect regions of constant-current density except for in (A) which displays contours for constant voltage. Each device (A-E) has a separate color key at the right which gives values for current density in A/m^2.

5.5.6 Peak Pulsed Current Density in the Externally-Shunted Hall Plate

The method of the previous section was used to calculate the peak 1-ms pulsed current for the ESHP family of devices. The semiconductor material properties and device dimensions are listed in Table 5-2. The semiconductor material properties are the same as those listed for the SCP calculations. For the two devices described in this chapter, the scale of the devices modeled is intended to be as similar as possible. The device thickness, total device active area, and material properties are identical. The only difference is the location and size of the contacts and the geometry as characterized by γ for the SCP and by τ for the ESHP. This was intended so that the calculations for each device could not only be compared within their respective device families, but also compared to each other.

The calculated peak 1-ms pulsed current for the ESHP device family is plotted as a function of τ in Fig. 5-21. The results are explained with the help of Fig. 5-22. In the absence of a shunt, the critical current density appears above the inner corners of the contacts where the electric field gradient is largest. Once a shunt is introduced into the geometry (τ = 4/20) as in Fig. 5-22 (B), a conduction path parallel to the direct path between contacts begins available. In this case the current density in the shunt is at a maximum for all values of τ, but the limiting semiconductor current density still occurs above the inner corners of the contacts. Larger shunts (τ = 8/20, 12/20) and correspondingly, a smaller semiconductor L/W ratio result in decrease shunt current density, but the region with the largest electric field gradient still occurs inside the

semiconductor region. As a result the peak pulsed current for 4/20 ≥ τ ≥ 12/20 does not change significantly, as shown in Fig. 5-21.

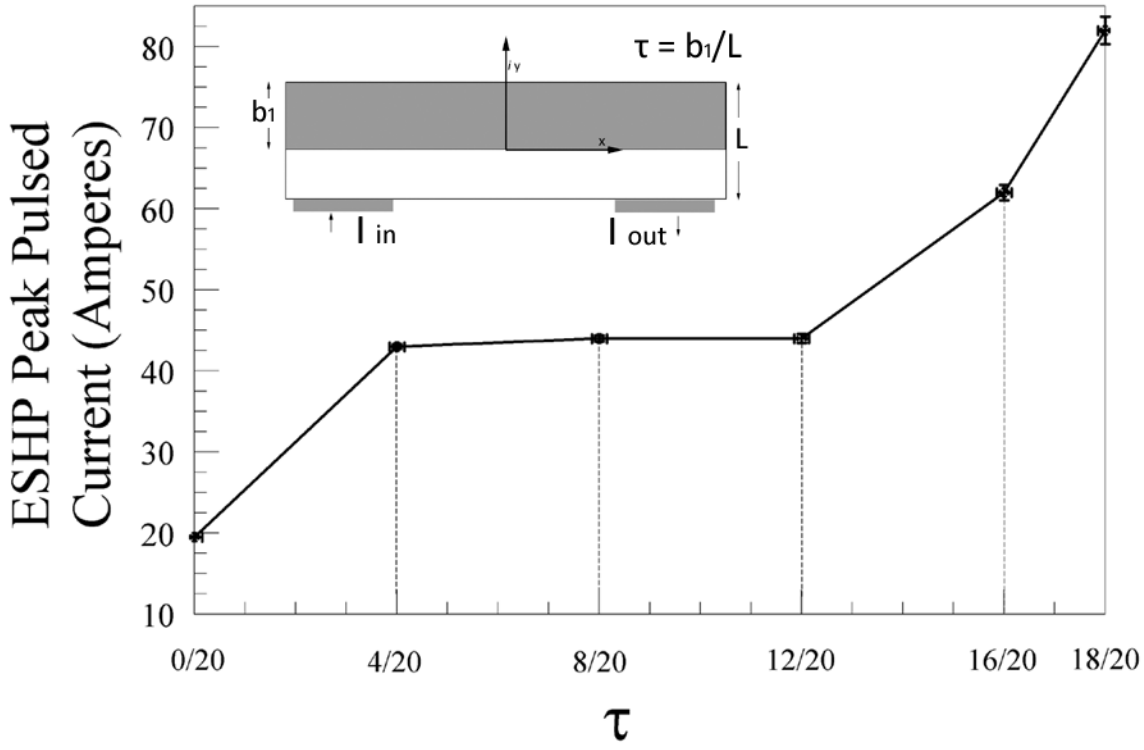

Fig. 5-21 Calculated Peak 1-ms pulsed current for the ESHP device family as a function of τ. Device dimensions and material properties are listed in Table 5-2.

The more interesting behavior begins to happen for larger τ values. For τ =16/20, the shunt current density drops as before, but now the parallel conduction path through the shunt begins to dominate over the direct path through the semiconductor. In Fig. 5-22 (E) (τ =18/20), the largest current density gradient now appears in the shunt and the current density between the semiconductor and shunt is much more uniform. In this case the current density in the direct semiconductor path between the contacts is at a minimum. This current distribution allows a significantly higher peak pulsed current.

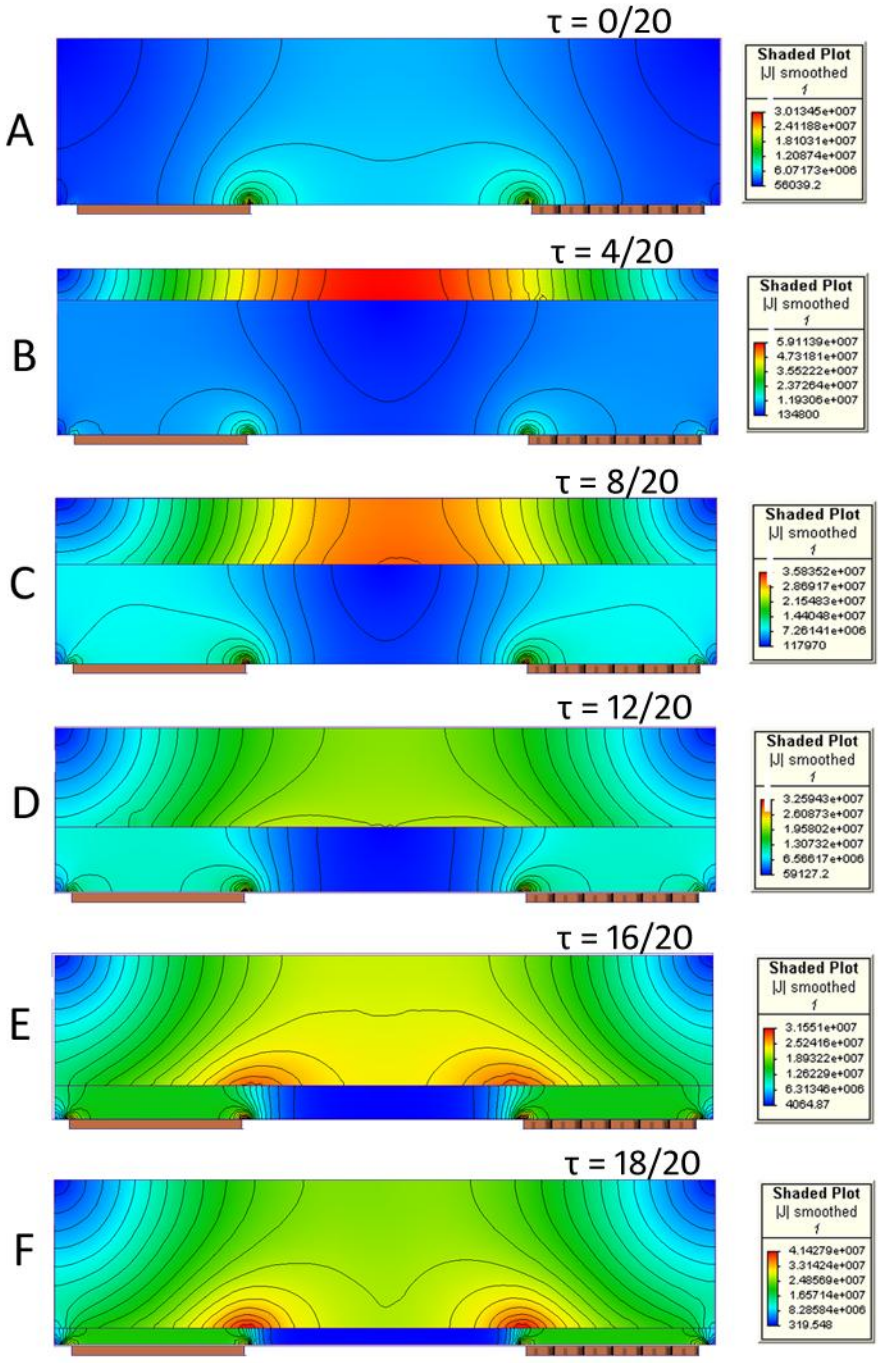

Fig. 5-22 Shaded plots of current density for the family of ESHP devices when conducting at their respective peak pulsed current. Contour lines connect regions of constant-current density. Each device (A-E) has a separate color key at the right which gives values for current density in A/m2.

5.6 Breakdown Voltage

InSb is typically used in EMR sensors because it has the highest room-temperature mobility of any conventional semiconductor. But, with this large mobility also comes a small gap energy (~0.17 eV) and the smallest effective mass ($0.015m_e$) of any candidate semiconductor [29]. Accordingly, InSb has an extremely low breakdown field. It is approximately two orders of magnitude lower than that of Si [29]. This is typically not a concern for EMR sensors because they have the freedom to operate at low voltages and correspondingly, low electric fields, even at nanoscale dimensions [4]. This is however an important characteristic of high-mobility, narrow-gap semiconductors for potential magnetoresistive power applications. The general trade-off is that one must choose a high mobility (large dR/dB) and a low breakdown field *or* a low mobility and high breakdown fields.

A MR power device can generally be considered "on" in the zero-field and "off" in high field. Thus, more important than breakdown as a function of electric field is the breakdown as a function of electric and magnetic field, i.e. breakdown in the $E \times B$ direction. This has been investigate experimentally in high-mobility semiconductors for transverse fields up to 0.4 T [30]. However, the examination of the zero magnetic field breakdown voltage serves the purpose of comparing electric field breakdown within one topology as a function of geometry (γ or τ), between the two topologies (SCP and ESHP), and for quantifying the trade-off with device sensitivity. Thus this section will examine breakdown in the case of $B = 0$.

Though more exact methods exist, e.g. [31, 32], the breakdown field in a semiconductor as set by impact ionization can be estimated as

$$E_{BD} \cong \sqrt{\frac{2E_g m^*}{q^2 t_c^2}} \tag{6.4}$$

where E_g is the gap energy, m^* is the effective mass, q is the electron charge, and t_c is the collision time [33]. The part of (6.4) that should be noted is that E_{BD} is proportional to the square root of the two unusually-low physical parameters of InSb, gap energy and effective mass. It is these two parameters that also give rise to the large mobility found in InSb [27].

Using (6.4), a room-temperature gap energy of 0.17 eV, an effective mass of 0.15 m_e, and a collision time of 3.87×10^{-13} s, the breakdown field in InSb (n, T) was calculated to be 4.4×10^5 V/m^2. For this calculation, the doping density was the same as in Table 5-1 and the collision time used is from [19].

In order to evaluate geometric effects on breakdown voltage, the two device families (SCP and ESHP) were analyzed using the same model described in section 6.6. Using the same Newtonian iteration technique, the source voltage was varied until the maximum nodal electric field was just below the breakdown field. In this process the final voltage iteration resolution was 1 V resulting in field uncertainties given by dE/dV at $E_{BD}(\tau)$ and indicated by the vertical error bars in Fig. 5-23 and Fig. 5-25. The horizontal error bars arise from the grid resolution used in the frame construction of each model.

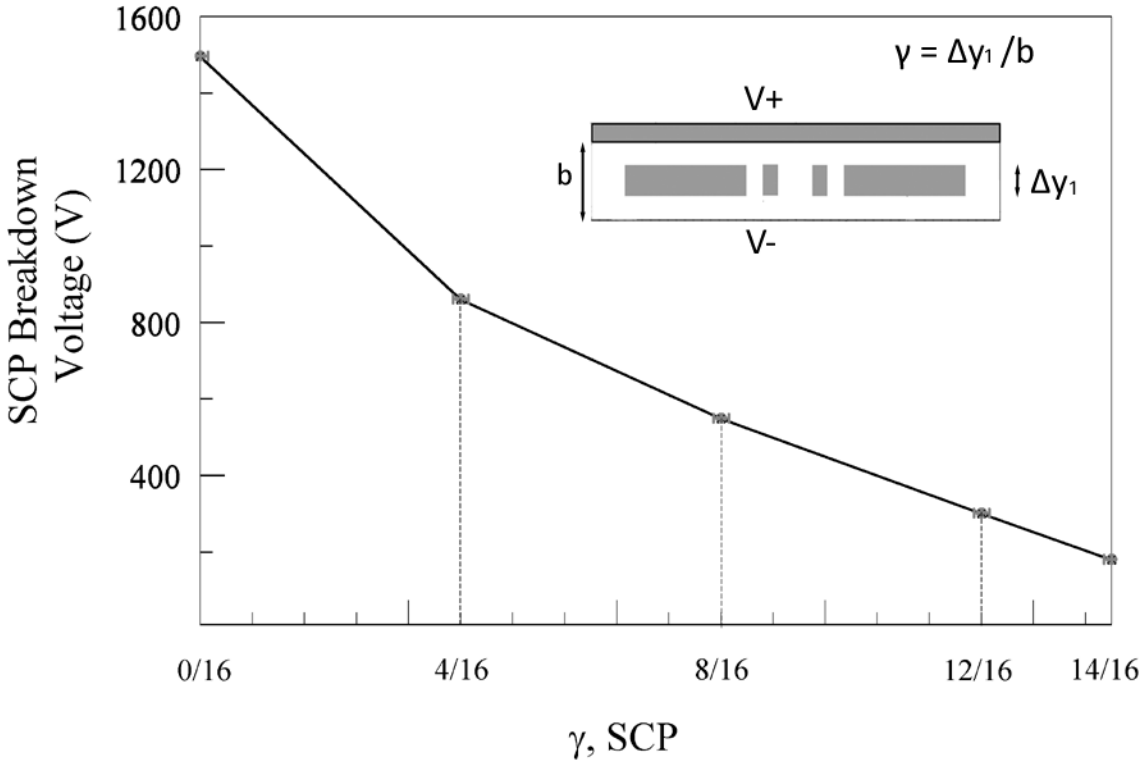

Fig. 5-23 Breakdown Voltage as a function of γ for the SCP device family.

For the SCP, the largest breakdown voltage is not surprisingly in the case of γ = 0/16. With no shunt, the electric field gradient is constant in the semiconductor region as in Fig. 5-24(A). For the cases that include a shunt, shown in Fig. 5-24(B)-(E), the breakdown voltage decreases steadily with increasing γ. This is simply because the region over which the voltage must change (γ direction) is decreasing as the shunt is an equipotential volume. In each shunted case, the peak electric field appears at the upper and lower corners of the shunt. For the γ = 14/16 case, Fig. 5-24(E), the device voltage at breakdown is the lowest, but the1-D potential gradient in the x direction (dE/dx) in the region between the shunt and the electrodes is a minimum.

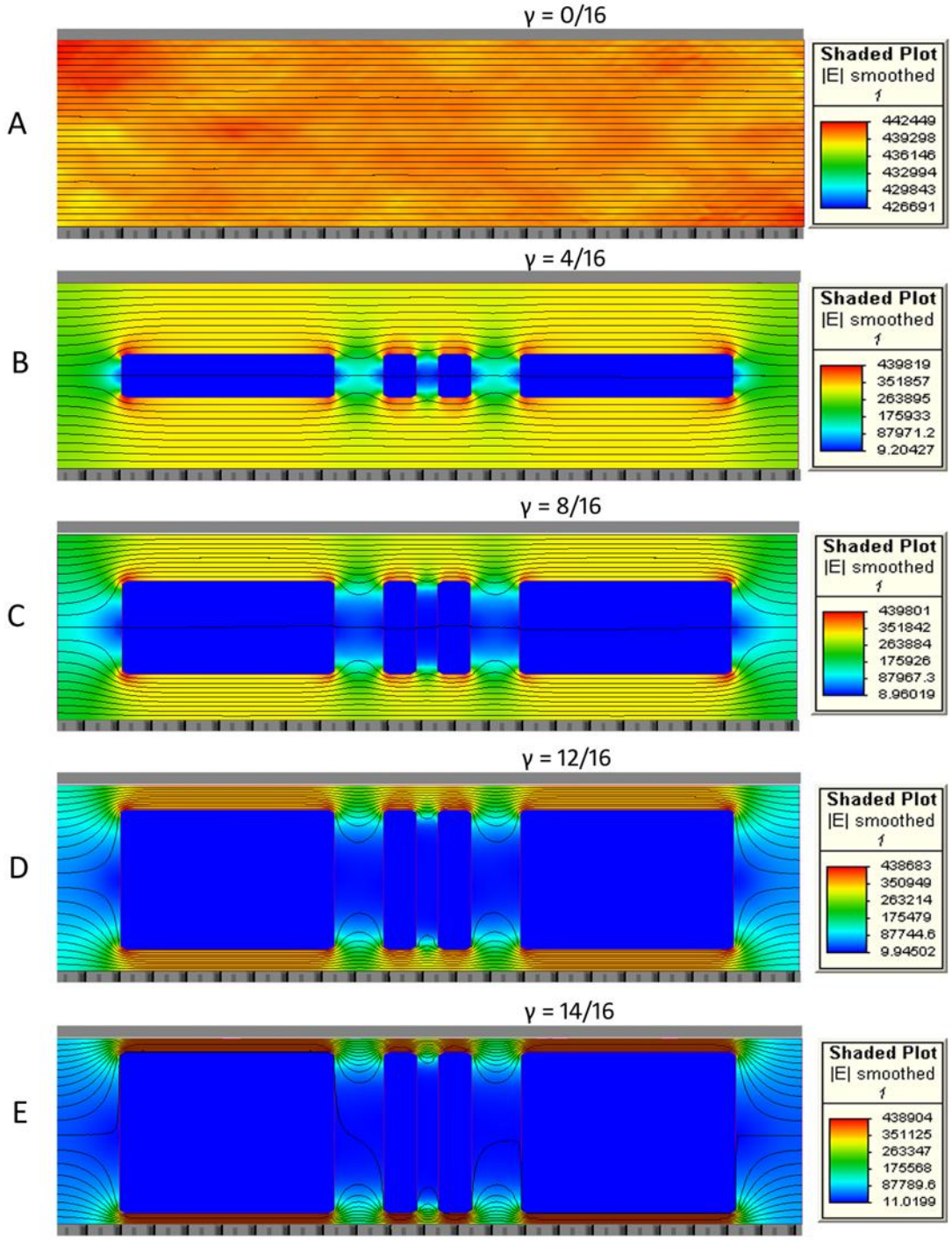

Fig. 5-24 Shaded plots of the electric field at breakdown voltage for selected values of γ in the SCP topology. Contour lines (black) connect regions of constant electric potential. Each device (A)-(E) has its own color key which gives electric potential in V/m.

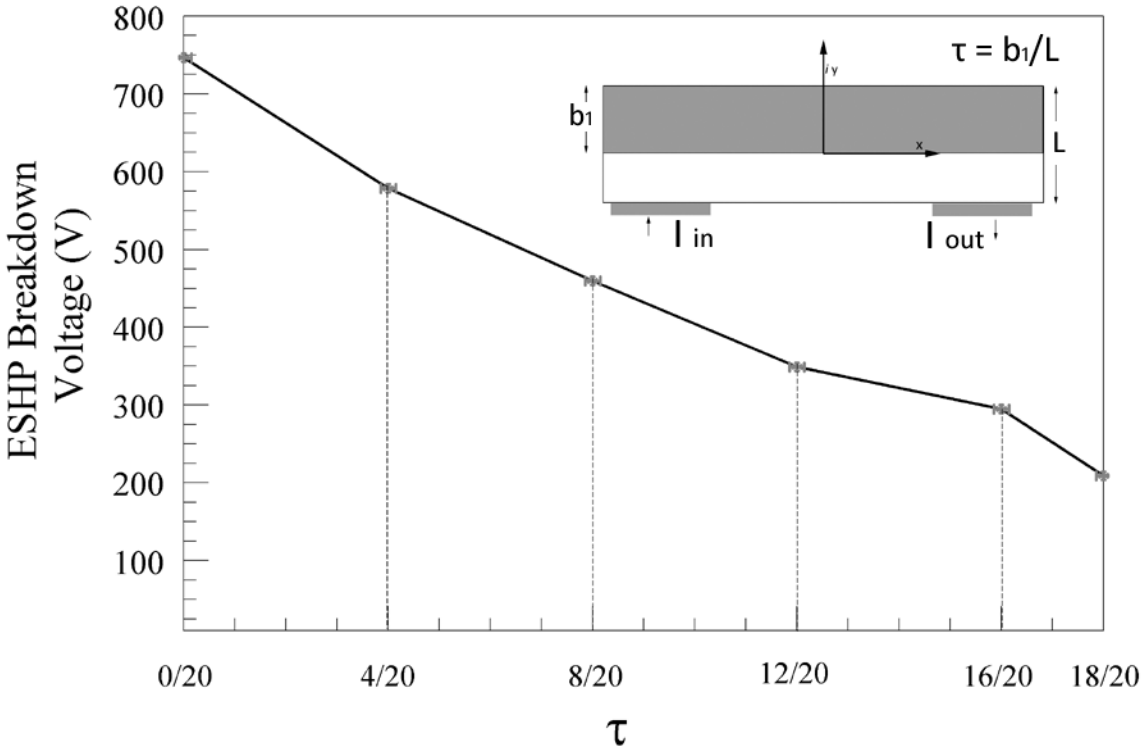

Fig. 5-25 Breakdown voltage as a function of τ for the ESHP device topology.

As shown in Fig. 5-25, the variation in breakdown voltage in the ESHP decreases steadily as τ increases. This is due simply to the reduction in semiconductor path length with increasing τ. The more interesting parts of these models are the 1-D electric field gradient in the x-direction between the electrodes (dE/dx) and the location of the peak electric field. These features can be seen in Fig. 5-26. With no shunt, the electric field is localized between the contacts and concentrated above the inner corners as shown in Fig. 5-26(A). In this case voltage contours that begin evenly spaced along the base fan out at the periphery and are nearly parallel at the midpoint. With increasing τ, the field intensity becomes less evenly distributed laterally between the contacts and localized between the contacts and the shunt. For τ =18/20, the electric field intensity quickly

falls to zero laterally between the contacts and the field is completely localized between the contacts and shunt. This is not due to the size of the shunt, but the semiconductor L/W ratio which is 0.025 for $\tau = 18/20$.

The peak field intensity is located above the inner contact corner in every case. For $\tau = 18/20$, the peak field also appears above the outer corners of the contact. As can be seen in Fig. 5-26(F), the peak field is much closer to the average field in the region above the contacts. The smaller local field factor in this case indicates a more efficient use of the semiconductor volume in the distribution of electric field for the smallest L/W ratio.

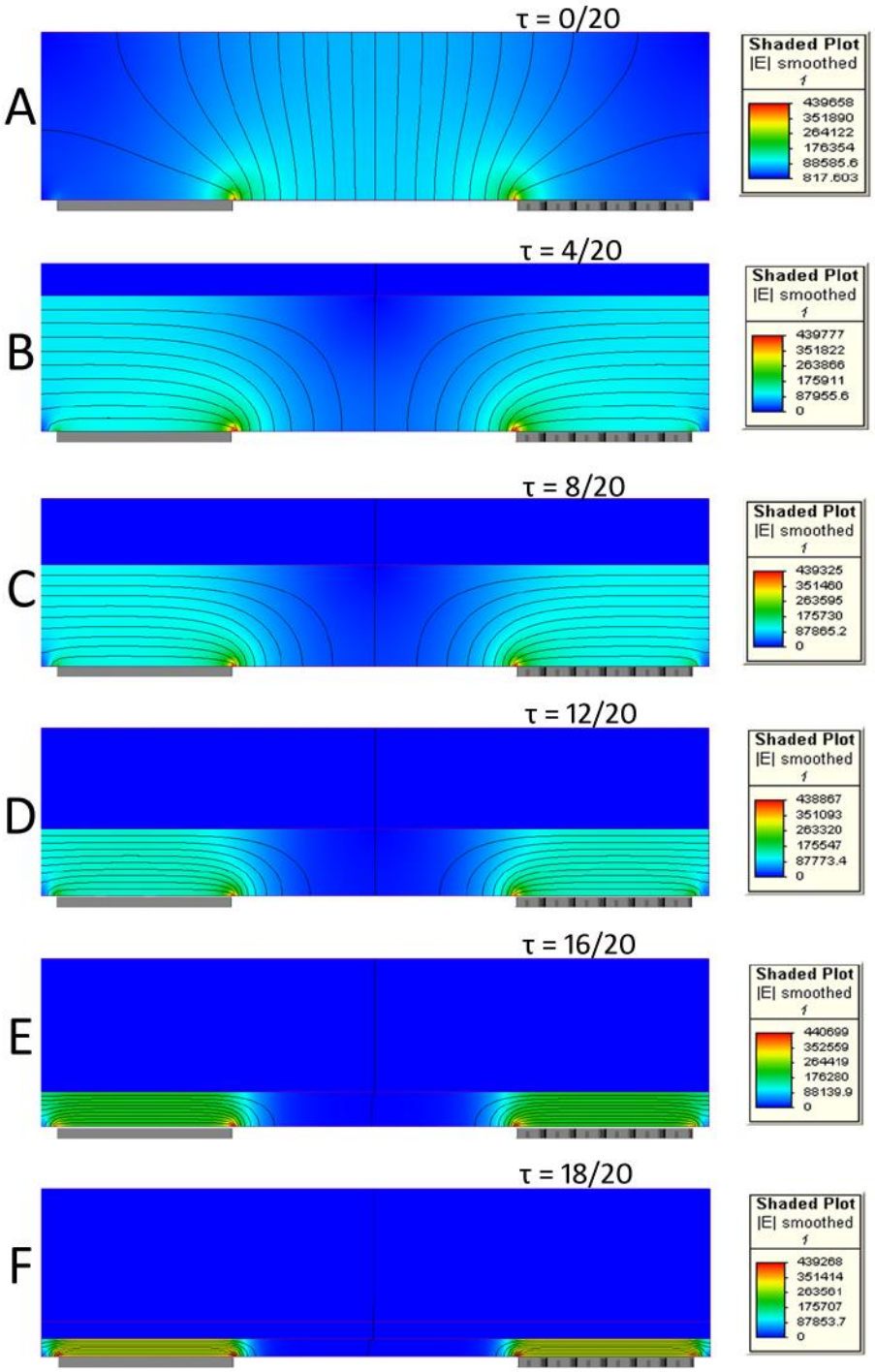

Fig. 5-26 Shaded plots of the electric field at breakdown voltage for the ESHP device topology for selected values of τ. Contour lines connect regions of constant electric potential (A)-(E) have separate color keys (right) that give the electric field value in V/m^2.

6. Summary and Conclusions

This section summarizes the results from the previous chapter and offers analysis based on those results. Next, some further considerations are introduced. These include candidate semiconductor material properties, considerations for low temperature operation, and scaling issues. The response of an EMR device to a pulsed magnetic field and preliminary implications for use as an opening switch are presented. This is followed by a discussion of future work and general conclusions regarding the use of the EMR effect for power applications.

6.1 Summary

In Chapter 5 the PSPICE FEM model was used to calculate the MR of two semiconductor-metal hybrid topologies, the shunted Corbino plate and the externally-shunted Hall plate. MR behavior was examined as a function of geometric ratios characteristic of each topology and semiconductor material properties. ElecNET models were generated to calculate peak pulsed-current capacity and breakdown voltage for each device family in the absence of magnetic field. The characterization of these prototype EMR-based power device topologies is built on the PSPICE model described in Chapter 3, the model validation and 2-point MR investigation presented in Chapter 4, and the ElecNET analysis introduced in Chapter 5. The results of the characterization presented in Chapter 5 are summarized for ease of reference in Table 6-1.

.

These results show that magnetoresistive behavior in these devices is a sensitive function of the geometric ratios introduced in Chapter 5. The 1-T MR values ranged from 12.76 to 20.80 in the SCP topology. The MR was more sensitive to geometric ratio among the ESHP family which displayed MR between 1.58 and 20.68 at 1 T. The largest 1-T MR among the devices was found to occur at γ =14/16 for the SCP family (MR=20.80) and at τ = 18/20 for the ESHP family (MR=20.68).

TABLE 6-1 SUMMARY OF MODELED CHARACTERISTICS OF THE SCP AND ESHP DEVICE TOPOLOGIES

Device Topology[1]	Geometric Ratio (γ,τ)	R(B=0) (Ohms)[2]	MR @ 1 T[2]	Peak 1-ms Pulsed Current (A)[3]	Breakdown Voltage (V)[3]	Semiconductor Region L/W
SCP	0/16	1.56E-01	12.76	410	1496	-
	4/16	1.26E-01	14.26	281	861	-
	8/16	8.45E-02	16.39	295	551	-
	12/16	4.48E-02	19.23	304	308	-
	14/16	2.50E-02	20.80	323	181	-
ESHP	0/20	1.64E+00	1.58	19.5	747	.25
	4/20	6.63E-01	5.00	43	578	0.2
	8/20	5.33E-01	6.54	44	460	0.15
	12/20	3.77E-01	9.39	44	349	0.1
	16/20	2.12E-01	15.37	62	295	0.05
	18/20	1.12E-01	20.68	82	209	0.025

[1] Each device has common overall dimensions (mm) [L x W x t] = [3.4 mm x 13.6 mm x 1.0 mm]. The semiconductor modeled was n-type InSb with [n, μ]=[2×10^{21} m^{-3}, 5 m^2/Vs]

[2] Calculated using PSPICE FEM Model

[3] Calculated using ElecNET© FEM Model

The SCP and ESHP each device display a complex dependence on semiconductor mobility in the PSPICE model. MR increases with semiconductor mobility at all fields, for all geometries but there is a point of diminishing returns that is device and field specific. Device resistance varies linearly but the MR remains constant for a very large range of dopant density, using (3.19) as the magnetoconductivity matrix in the PSPICE model. This result implies that the zero-field resistance of these devices can be controlled directly by varying the dopant density without affecting the MR for a given device geometry. This means the zero-field resistance can be tuned over a wide range to achieve an application specific zero-field resistance. The major constraint is that the dopant density must not raise the conductivity of the semiconductor near that of the shunt, i.e. $\sigma(n)_{semiconductor} << \sigma_{shunt}$. Compliance is easy in the case of a metallic shunt and any candidate semiconductors (InSb, InAs, HgCdTe). Though considered constant over the range of dopant densities investigated in the PSPICE model, the electron mobility can be expected to decrease at very large doping densities ($> 10^{22}$ m^3) due to electron-electron interaction and scattering from dopant species [27].

In the SCP topology, the inclusion of a shunt of any size causes a non-uniform current distribution in the absence of transverse magnetic field. This leads to hotspots that reduce the pulsed-current capacity of the devices. There is however, an increase in pulsed-current capacity for larger γ values, e.g. the capacity increases 15% from γ=4/16 to γ=14/16.

The entire ESHP family has roughly and order of magnitude smaller pulsed-current capacity compared to the SCP. These devices are also limited by current hotspots in the

zero field but more so due to longer path through the semiconductor and the same-side contact arrangement. Of the examined geometric ratios, current capacity is a maximum for τ =18/20 which corresponds to a semiconductor region L/W ratio of 0.025.

The geometries with the largest MR and pulsed current capacity exhibit the lowest breakdown voltages of all devices modeled. This can be seen for the γ =14/16 and τ = 18/20 rows in Table 6-1 for the SCP and ESHP respectively. Not only does geometry limit the breakdown voltage of these devices, but the high mobility semiconductors necessary for large MR have extremely-low breakdown fields compared to silicon.

6.2 Further Considerations: Materials and Scaling

Other important considerations include the tradeoffs among different semiconductors, and their behavior at low temperature. Typical relevant room-temperature material properties for candidate semiconductors are presented here along with considerations for low-temperature use. Additionally, scaling considerations are presented in this section.

6.2.1 Semiconductor Material Properties

The characterizations presented here default to n-type InSb as the semiconductor material when specific values are necessary, but there are other candidate semiconductors. The candidate semiconductors are listed in Table 6-2 along with Si for standard comparison. Typical properties relevant to EMR and power characteristics are listed. Each has its own non-ideal property.

InAs is likely the next best candidate at room temperature since it shows an electron mobility nearly half that of InSb, has an order of magnitude higher breakdown field, and ~50% higher melting temperature. HgCdTe suffers the same trade-off between mobility and breakdown field and it also has a very low thermal conductivity. Both of these properties are detrimental for power applications. Compared to InSb, the breakdown field in GaAs is two orders of magnitude, the melting temperature is nearly double, but its electron mobility only around 10%. Since multiple semiconductors each have different advantages and disadvantages, the material chosen should be application specific.

TABLE 6-2 TYPICAL MATERIAL PROPERTIES OF CANTIDATE SEMICONDUCTORS FOR POWER EMR DEVICES

Property [α]	Si [β]	InSb	InAs	$Hg_{0.9}Cd_{0.1}Te$	GaAs
gap energy @300K (eV)	1.12	0.17	0.354	<0.1 [γ]	1.43
relative dielectric constant	11.8	16.8	15.5	18	12.8
thermal conductivity @300 K ($W\ cm^{-1}\ °C^{-1}$)	1.3	0.16	0.29	0.02	0.55
electron mobility @ 300 K ($m^2\ V^{-1}\ s^{-1}$)	0.19	7.7	~2	1.1-3.0 [γ]	0.85
breakdown electric field (V/m)	$3x10^7$	$\sim10^5$	$4x10^6$	$\sim10^5$-10^6 [γ]	$4x10^7$
melting temperature (K)	1685	798	1215	~940	1510
electron effective mass (m^*)	0.98	0.015	0.023	0.017-0.11 [γ]	0.063
specific heat (J/kG C)	700	200	268	~160	330

[α] Values taken from [29, 34, 35]

[β] For comparison standard, not considered a candidate.

[γ] Sensitive to Hg-Cd ratio: *x* in $Hg_x\ Cd_{1-x}Te$

The sensitivity (dR/dB) of an EMR power device can be improved simply by cooling the active region to increase the electron mobility via minimizing electron-phonon interactions [36, 37]. For example, while carrier concentration remains relatively constant the Hall mobility for $n=4x10^{21}$ m^{-3} InAs goes from 1.2 to 5.1 m^2/Vs for a temperature decrease from 300 K to 77 K [29]. InSb goes from μ =~7 to 27 m^2/Vs for a temperature decrease from 300 K to 77 K for dopant density of $1x10^{21}$ m^{-3} [38, 39]. However, the mobility falls rapidly below ~60 K in InSb with all dopant densities [40]. Another benefit of cooling is the increase in gap energy which is proportional to the square of the breakdown field. For a temperature decrease from 300 K to 77 K InAs and InSb show a 30% and 15% increase in gap energy [41]. The opportunity cost of sufficient cooling during operation is however not trivial.

For example, In 2D electron structures (2DES) which are characterized at very low temperatures (<10 K), InAs is preferred [42]. Although InAs has a lower mobility than InSb at such low temperatures, InAs retains ohmic-contact character and low contact resistance at the Au interface persists. At temperatures below 50 K, the surface depletion layer at InSb-Au interface becomes rectifying and causes an undesirable increase in interface resistance [43].

6.2.2 Scaling Considerations

As shown in Chapters 4 and 5, the zero-field device resistance can be tuned through the doping process for extrinsic high-mobility semiconductors while the MR remains constant. Though the semiconductor electron mobility is not drastically reduced with

heavy doping, it is diminished [18]. The tuning of resistance for a specific application can be accomplished more elegantly via scaling, i.e. controlling the device thickness in the direction of the applied magnetic field. This has been noted for magnetoresistive sensor applications that may require a relatively large (~1 kΩ) zero-field resistance to limit current consumption and heat dissipation [12]. This scaling solution is limited since the semiconductor mobility drops rapidly with thicknesses below 1 μm due to scattering on dislocations that extend into the active region caused by the lattice mismatch at the substrate (e.g. GaAs) interface [8, 44].

Most EMR devices that have been fabricated with areas (normal to the magnetic field) from ~nm^2 to mm^2 and thicknesses ≤ ~1 μm [20, 24]. Typically, scaling to nm dimensions is of importance to EMR devices for sensing applications (e.g. read heads and scanning microscopes). Scaling to large sizes (area ~cm^2, thickness > 1mm) has not typically been considered in the EMR literature. There is nothing physical to preclude the development of a large-scale EMR device. The primary obstacle is in cost of fabrication for a large volume of high-mobility InSb with an embedded metal that forms a low-resistance interface. The conventional method of fabricating EMR sensors is by using MBE for the semiconductor region and metal vapor deposition for the embedded Au shunt [2]. At large sizes this method would become prohibitively expensive and time consuming. Turchi et al. opted for large InSb disks, indium soldered to surface contacts for a large Hall-effect opening switch in [14]. Fabrication of a large volume (~cm^3) high-mobility semiconductor matrix that includes an embedded, low-contact-resistance metallic shunt structure remains as a non-trivial obstacle.

6.3 Response to a Pulsed Magnetic Field

As mentioned in Chapter 1, the fundamental limitation to the response time of EMR sensor devices is approximated by the inverse of the solid-state plasma frequency, which for typical n-type semiconductors is on the order of 10^{-12}-10^{-13} s [37]. This is given by:

$$\omega = \left[\frac{Ne^2.}{\epsilon m}\right]^{\frac{1}{2}} \tag{6.1}$$

For example, using (6.1) the plasma frequency of InSb with N=10^{21} m^{-3} is ω=4.35x10^{-11} Hz. This gives a relaxation time approximation of 2.3x10^{-12} s. This is the basis for the estimate of the temporal response of an EMR-based device to a local magnetic field pulse. Other questions regarding the pulsed response of an EMR-based power device are how does the local transient response compare to conventional power devices? And what are the practical (global) pulsed response limitations?

The general treatment of charge-carrier magneto-transport in this case is based on the solution to the Boltzmann kinetic equation. This is developed in great detail in [45]. The treatment is based on the relaxation time approximation given by (6.1). The relaxation time is the time constant for charge carriers responding to local electric and magnetic fields and thus the time constant for the change in resistance due to the EMR effect.

Response faster than the relaxation time limit is affected by electron inertia based on the effective mass of the majority carrier. The drift velocity is no longer based on the

mean free transit time and the basic parameters for electrical transport (i.e. Hall mobility) are no longer valid. For local response to a rapidly changing electric field (bias field) the dielectric relaxation time limit ($t_r=\varepsilon/\sigma$), skin effect, and eddy current generation affect response time. Here the scope is limited to the most fundamental collective behavior of solid-state plasma to the magnetic field, which determines the basic limit on rate of resistance increase of an EMR based device [37].

In practice, non-fundamental factors will limit the pulsed response time of a given EMR-based power device in a given circuit. These include extrinsic (circuit) capacitance which limits voltage transition time and extrinsic inductance which limits the current transition time. A more notable limitation lies in the large control magnetic field necessary to generate a large MR. Ideally the controlling magnetic field would appear as a square pulse or waveform. The large controlling field requirement demands that the pulsed response limit will be determined most likely by the rise time of the magnetic-field-inducing current pulse in a single turn solenoid or a low N Helmholtz coil [14].

To introduce a small amount of application specificity, it is useful to compare an opening switch based on the EMR effect to other types of repetitive opening switches. One figure of merit for an opening switch is the rate of impedance rise during opening, or $\Delta R/\Delta t$ for a resistive opening switch. Using the relaxation time approximation, we can estimate this figure for the ESHP and the SCP devices of Chapter 5. In order to isolate the local EMR response of a given device, we will ignore global capacitance and inductance and assume a spatially uniform, 1 T square-pulse magnetic field. The best

geometric-ratio devices from each topology described in Chapter 5, give ΔR/Δt values between 10^{10} Ω/s and 10^{11} Ω/s. Neglecting the extrinsic response time factors mentioned previously, this figure of merit compares well to other opening switches as shown in Table 6-3.

TABLE 6-3 ESTIMATED FIGURES OF MERIT FOR REPETITIVE OPENING-SWITCH TECHNOLOGIES AND EMR

Property	EMR [β,γ]	Semiconductor/ SCR [46-48]	Diffuse Plasma [49, 50]	Hall-Effect [14]
ΔR/Δt (Ω/s)	10^{10}-10^{11} [α]	10^{5}-10^{7}	10^{8}-10^{9}	10^{4} [α]
Opening time (s)	~10^{-12}	10^{-6}-10^{-9}	10^{-6}-10^{-9}	10^{-12} [β]
Interruption current density (A/cm^2)	~10^{2}	10^{2}-10^{5}	< 10^{2}	5x10^{3}

[α] For B=1 T

[β] Not including global capacitance, inductance, and actuating magnetic field rise time.

[γ] Based on the devices described in Chapter 5

Crucial characteristics of repetitive opening switches not listed in Table 6-3 include conduction time at interrupt current density, power dissipated during opening, and open-state hold-off voltage. An EMR-based opening switch would have relatively poor ratings in all of these categories, especially when evaluated at same volumetric scale. The reasons for this are fundamental and are illustrated in Chapter 5 for the two prototype topologies. First the non-uniform current densities (hotspots) at both zero and high magnetic fields leads to low interruption current-density capacity and low on-state conduction current capabilities for a given volumetric scale. Second, the high-

mobility semiconductor that must be used for a large MR is fundamentally handcuffed to a low breakdown voltage in the open state. These factors have been described in Chapter 5 and it is clear that compared to the state of the art SOS technology, an EMR-based opening switch would not comparable power handling capabilities at same scale [48]. The only clear advantages would lie in rate of impedance rise and fast transition (opening and recovery) times [49]. High power (~1 kV hold-off voltage, ~1 kA conduction current) operation is possible but would require a large active volume and a large-area controlling magnetic field.

6.4 Future investigations

The work described in this paper represents the initial and prospective exploration of the EMR effect for power applications. The work presented here lays a foundation on which several different investigations may be based. Suggested future investigations can be broken down into 3 categories: additional model validation, an improved model, and a characterization and analysis of an EMR-based opening switch.

Present model validation should be performed by comparing experimental results with actual devices similar to those modeled using the PSPICE FEM model. This comparison will show the ways the model needs to be improved and in which ways it is sufficient. The validation leads to the next area which is an improved model. A comprehensive model validation will present areas of model improvement in addition to those already apparent, which follow.

One manifestation of next generation model would ideally be in a modified ElecNet code. Modifying the standard ElecNET code to account for the 2-D magnetoconductivity given by (3.19), could allow it to take over the primary role of the PSPICE method with the following benefits. First, the ElecNET Code is optimized for mesh construction. It allows easy implementation of curve and border refinement algorithms which would improve the accuracy in calculating magnetoresistance and facilitate a much higher mesh density [28]. ElecNET also contains a robust graph generation tools in terms of electric field, electric potential, and current density. These benefits are offset by the loss of PSPICE's built-in diagnostic tools and more sophisticated transient and multi-tiered circuit capabilities. This becomes of prime importance for the third area, characterization as an opening switch.

One of the main benefits of using the PSPICE model is the ability to model transient response of an EMR-based hybrid. For characterizing an EMR opening switch, the ability to model global inductance and capacitance along with the intrinsic parameters is important. This is why it will be useful to extend the modeling effort in both programs. ElecNET should be pursued to improve the accuracy of the MR behavior and develop useful data products such as low and high-magnetic-field current-density maps and electric-field distribution maps. The PSPICE model should be further developed to characterize the intrinsic transient response along with the global transient response in a practical circuit with a magnetic field generation sub-circuit. The transient characterization should include predictions for maximum repetition rate in a simple inductive energy store circuit with nominal circuit and switch inductance values.

Additionally, breakdown at large E×B fields in an EMR device would be the next seminal experimental data product for characterization as an opening switch. This has been measured previously for simple Hall devices, but only at relatively low magnetic field magnitudes [30].

6.5 Conclusions

The MR characterization of the prototype semiconductor-metal hybrid devices as a function of topology, geometric ratio, and semiconductor material properties forms the fundamental evaluation of EMR devices for power applications. The evaluation of the 2-point MR for existing and prototype EMR-based devices is essential for power applications. The *distinction* between 2-point and 4-point MR is important to assign the proper gravity to the extremely large MR reported in sensor literature, when translated to a power context. The identification and evaluation of pulsed current and breakdown voltage limitations using the ElecNET model is a first for EMR-based semiconductor-metal hybrids. The data set presented here is useful for purely characterization purposes. But additionally, these findings and the unavoidable trade-off between Hall mobility and breakdown field in the active semiconductor evidence the unique obstacles for the implementation of the EMR effect in potential power applications.

EMR-based devices for sensing applications have been well characterized and their advantages in that role have been demonstrated in the literature as described in Chapter 2. The data set presented here suggests that in general it would be more efficient and practical to use conventional devices in power switching applications. In applications that may benefit from magnetic field sensing to actuate power switching, it

would be more practical to separate the sensing mechanism from the power switching mechanism. This assertion follows from the mobility vs. breakdown field trade-off in narrow-gap high-mobility semiconductors.

The reason so many types of power semiconductor devices exists is because of the broad scope of applications, and the range of requirements within any one type of application. The characterization of EMR-based semiconductor-metal hybrids as power devices, adds a fundamentally different type of operating principle for consideration. Although an application well suited to benefit from the advantages and tolerate the limitations of an EMR power device may not exist today, it is not unreasonable to think that one will exist in the future.

References

[1] S. A. Solin, T. Thio, and D. R. Hines, "Controlled GMR enhancement from conducting inhomogeneities in non-magnetic semiconductors-Solid-State Sci. Technol," *Physica B,* vol. 279, pp. 37-40, 2000.

[2] S. A. Solin, T. Thio, D. R. Hines, and J. J. Heremans, "Enhanced Room-Temperature Geometric Magnetoresistance in Inhomogeneous Narrow-Gap Semiconductors," *Science,* vol. 289, pp. 1530-1532, September 1, 2000 2000.

[3] T. Thio and S. A. Solin, "Giant magnetoresistance enhancement in inhomogeneous semiconductors," *Applied Physics Letters,* vol. 72, p. 3497, 1998.

[4] S. A. Solin, D. R. Hines, A. C. H. Rowe, J. S. Tsai, and Y. A. Pashkin, "Nanoscopic magnetic field sensor based on extraordinary magnetoresistance," *Journal of Vacuum Science & Technology B: Microelectronics and Nanometer Structures,* vol. 21, p. 3002, 2003.

[5] D. R. Hines, S. A. Solin, T. Thio, and T. Zhou, "Extraordinary magnetoresistance at room temperature in inhomogeneous narrow-gap semiconductors," USPO, Ed. U.S.: NEC Laboratories America, Inc., 2004.

[6] J. Moussa, L. R. Ram-Mohan, A. C. H. Rowe, and S. A. Solin, "Response of an extraordinary magnetoresistance read head to a magnetic bit," *Journal of Applied Physics,* vol. 94, p. 1110, 2003.

[7] S. Solin, "Magnetic field nanosensors," *Scientific American,* vol. 291, pp. 70-77, 2004.

[8] S. A. Solin, D. R. Hines, J. S. Tsai, Y. A. Pashkin, S. J. Chung, N. Goel, and M. B. Santos, "Room temperature extraordinary magnetoresistance of nonmagnetic narrow-gap semiconductor/metal composites: application to read-head sensors for ultrahigh-density magnetic recording," *Magnetics, IEEE Transactions on,* vol. 38, pp. 89-94, 2002.

[9] R. S. Popovic, *Hall effect devices*: Institute of Physics, 2004.

[10] S. A. Solin, D. R. Hines, A. C. H. Rowe, J. S. Tsai, Y. A. Pashkin, S. J. Chung, N. Goel, and M. B. Santos, "Nonmagnetic semiconductors as read-head sensors for ultra-high-density magnetic recording," *Applied Physics Letters,* vol. 80, p. 4012, 2002.

[11] R. S. Popovic, "Complete Galvanomagnetic Equation," in *Hall Effect Devices*: Inst of Physics Pub Inc, 2004.

[12] J. Heremans, "Solid state magnetic field sensors and applications," *J. Phys. D: Appl. Phys,* vol. 26, p. 1168, 1993.

[13] J. Heremans, D. L. Partin, C. M. Thrush, and L. Green, "Narrow-gap semiconductor magnetic-field sensors and applications," *Semicond. Sci. Technol,* vol. 8, pp. S424-S430, 1993.

[14] E. K. Inall, A. E. Robson, and P. J. Turchi, "Application of the Hall effect to the switching of inductive circuits," *Review of Scientific Instruments,* vol. 48, p. 462, 1977.

[15] C. Herring, "Effect of Random Inhomogeneities on Electrical and Galvanomagnetic Measurements," *Journal of Applied Physics,* vol. 31, p. 1939, 2004.

[16] A. Y. Shik, *Electronic Properties of Inhomogeneous Semiconductors*: Taylor & Francis, 1995.

[17] C. M. Wolfe, G. E. Stillman, and J. A. Rossi, "High Apparent Mobility in Inhomogeneous Semiconductors," *Journal of The Electrochemical Society,* vol. 119, p. 250, 1972.

[18] S. A. Solin and T. Thio, "GMR enhancement in inhomogeneous semiconductors for use in magnetoresistance sensors," USPO, Ed.: NEC Research Institute, Inc., 1999.

[19] J. Moussa, L. R. Ram-Mohan, J. Sullivan, T. Zhou, D. R. Hines, and S. A. Solin, "Finite-element modeling of extraordinary magnetoresistance in thin film semiconductors with metallic inclusions," *Physical Review B,* vol. 64, p. 184410, 2001.

[20] S. A. Solin, "Extraordinary Phenomena in Semiconductor-Metal Hybrid Nanostructures Based on Bilinear Conformal Mapping," *Arxiv preprint cond-mat/0602110,* 2006.

[21] R. S. Popovic, "Numerical analysis of MOS magnetic field sensors," *SOL. ST. ELECTRON.,* vol. 28, pp. 711-716, 1985.

[22] A. Salim, T. Manku, A. Nathan, Q. S. Inc, and C. A. Santa Clara, "Modeling of magnetic field sensitivity of bipolarmagnetotransistors using HSPICE," *Computer-Aided Design of Integrated Circuits and Systems, IEEE Transactions on,* vol. 14, pp. 464-469, 1995.

[23] R. F. Wick, "Solution of the Field Problem of the Germanium Gyrator," *Journal of Applied Physics,* vol. 25, pp. 741-756, 1954.

[24] M. Holz, O. Kronenwerth, and D. Grundler, "Magnetoresistance of semiconductor-metal hybrid structures: The effects of material parameters and contact resistance," *Physical Review B,* vol. 67, p. 195312, 2003.

[25] T. Zhou, "Extraordinary magnetoresistance in externally shunted van der Pauw plates," *Applied Physics Letters,* vol. 78, p. 667, 2001.

[26] M. Holz, O. Kronenwerth, and D. Grundler, "Enhanced sensitivity due to current redistribution in the Hall effect of semiconductor-metal hybrid structures," *Applied Physics Letters,* vol. 86, p. 072513, 2005.

[27] O. Madelung, *Semiconductors. Group IV elements and III-V compounds*: Berlin; New York: Springer-Verlag, 1991.

[28] "ElecNet," 6.14.1 ed 300 Léo-Pariseau, Suite 2222 Montréal, Québec H2X 4B3,Canada Infolytica Corporation.

[29] O. Madelung, *Semiconductors-basic data*: Springer, 1996.

[30] M. Toda and M. Glicksman, "Transverse Breakdown in a Strong Hall Electric Field," *Physical Review,* vol. 140, pp. 1317-1323, 1965.

[31] A. A. Andronov, "Electron runaway in strong E. LH fields and breakdown in n-InSb," *J. Phys. C: Solid State Phys,* vol. 13, p. 6287—6297, 1980.

[32] W. P. Dumke, "Theory of Avalanche Breakdown in InSb and InAs," *Physical Review,* vol. 167, pp. 783-789, 1968.

[33] N. Mohan, T. M. Undeland, and W. P. Robbins, *Power electronics*: Wiley New York, 1995.

[34] P. Capper, *Properties of Narrow Gap Cadmium-Based Compounds*: Iet, 1994.

[35] D. R. Lide, *CRC handbook of chemistry and physics*: CRC Press Boca Raton, FL, 1999.

[36] T. D. Boone, L. Folks, J. A. Katine, S. Maat, E. Marinero, S. Nicoletti, M. Field, G. J. Sullivan, A. Ikhlassi, and B. Brar, "Temperature Dependence of Magnetotransport in Extraordinary Magnetoresistance Devices," *Magnetics, IEEE Transactions on,* vol. 42, pp. 3270-3272, 2006.

[37] M. F. Hoyaux, *Solid state plasmas*. London: Pion, 1970.

[38] E. D. Palik, G. S. Picus, S. Teitler, and R. F. Wallis, "Infrared Cyclotron Resonance in InSb," *Physical Review,* vol. 122, pp. 475-481, 1961.

[39] D. L. Rode, "Electron Transport in InSb, InAs, and InP," *Physical Review B,* vol. 3, pp. 3287-3299, 1971.

[40] Chusov, II and N. G. Yaremenko, "Magnetoresistance of Strongly Compensated n-Type InSb," *Sov. Phys. Semiconductors,* vol. 7, pp. 830-831, 1973.

[41] Z. M. Fang, K. Y. Ma, D. H. Jaw, R. M. Cohen, and G. B. Stringfellow, "Photoluminescence of InSb, InAs, and InAsSb grown by organometallic vapor phase epitaxy," *Journal of Applied Physics,* vol. 67, p. 7034, 1990.

[42] M. Hoener, O. Kronenwerth, C. Heyn, D. Grundler, and M. Holz, "Geometry-enhanced magnetoresistance of narrow Au/ InAs hybrid structures incorporating a two-dimensional electron system," *Journal of Applied Physics,* vol. 99, p. 036102, 2006.

[43] S. A. Solin, "Design and Properties of a scanning EMR probe Microscope," *Arxiv preprint cond-mat/0602146,* 2006.

[44] S. D. Parker, R. L. Williams, R. Droopad, R. A. Stradling, K. W. J. Barnham, S. N. Holmes, J. Laverty, C. C. Phillips, E. Skuras, and R. Thomas, "Observation and control of the amphoteric behaviour of Si-doped InSb grown on GaAs by MBE," *Semiconductor Science and Technology,* vol. 4, pp. 663-676, 1989.

[45] R. S. Popovic, "3.2 Kinetic Equation Approach," in *Hall Effect Devices*: Inst of Physics Pub Inc, 2004.

[46] I. V. Grekhov and G. A. Mesyats, "Physical basis for high-power semiconductor nanosecond openingswitches," *Plasma Science, IEEE Transactions on,* vol. 28, pp. 1540-1544, 2000.

[47] K. H. Schoenbach, V. K. Lakdawala, D. C. Stoudt, T. F. Smith, and R. P. Brinkmann, "Electron-beam-controlled high-power semiconductor switches," *Electron Devices, IEEE Transactions on,* vol. 36, pp. 1793-1802, 1989.

[48] G. A. Mesyats, S. N. Rukin, S. K. Lyubutin, S. A. Darznek, Y. A. Litvinov, V. A. Telnov, S. N. Tsiranov, and A. M. Turov, "Semiconductor opening switch research at IEP," *Pulsed Power Conference, 1995. Digest of Technical Papers. Tenth IEEE International,* vol. 1, 1995.

[49] K. H. Schoenbach, M. Kristiansen, and G. Schaefer, "A review of opening switch technology for inductive energy storage," *Proceedings of the IEEE,* vol. 72, pp. 1019-1040, 1984.

[50] W. Pfeiffer and M. Junker, "COMPARISON OF TWO DIFFERENT CONCEPTS TO REALIZE AN OPENING SWITCH WITH HIGH REPETITION RATE," *Pulsed Power Conference, 1993. Digest of Technical Papers. Ninth IEEE International,* vol. 1, 1993.

Vita

Clay Nunnally received the B.S. degree in physics from Abilene Christian University in 2001, the M.S. degree in engineering physics from University of Virginia in 2004, and the Ph.D. in Electrical Engineering from the University of Missouri in 2008.

He served as a Project Assistant in preparing the MicroMAPS satellite-based remote sensor with NASA Langley Research Center in 2002. He then served as the Assistant Principal Investigator with the University of Virginia in developing an atmospheric remote-sensing payload that was launched from NASA Wallops Island Flight Facility in 2004. His research interests include space based remote sensing, pulsed power technology, and the economy and efficiency of alternative energy systems.

Clay Nunnally is a Student Member of the International Society for Optical Engineering and Sigma Pi Sigma. He was named one of 50 University Scholars and received the Fred Barton Physics award at Abilene Christian in 2001. He was awarded an NSF IGERT fellowship, a UVA Dean's fellowship, and a Virginia Space Grant Consortium fellowship at the University of Virginia.